



A University of Sussex PhD thesis

Available online via Sussex Research Online:

<http://sro.sussex.ac.uk/>

This thesis is protected by copyright which belongs to the author.

This thesis cannot be reproduced or quoted extensively from without first obtaining permission in writing from the Author

The content must not be changed in any way or sold commercially in any format or medium without the formal permission of the Author

When referring to this work, full bibliographic details including the author, title, awarding institution and date of the thesis must be given

Please visit Sussex Research Online for more information and further details



University of Sussex

**Large-Eddy Simulation of Separated-Flow
Transition under Elevated Free-Stream Turbulence
and Pressure Gradient**

HuaJun Li

Submitted for the degree of Doctor of Philosophy

University of Sussex

February 2022

Abstract

The primary focus of this PhD thesis is to enhance current understanding on boundary layer separated-flow transition under elevated free-stream turbulence (FST). Due to the applied free-stream turbulence, streaks are formed and propagate inside the boundary layer. These play an important role in the transition process. Previous studies have revealed that transition can occur due to both inviscid Kelvin-Helmholz (K-H) instability and streak-related instability mechanisms. Also, in an elevated FST environment, such as under 1.99% FST, streaks are found to contribute higher energy than the K-H instability during transition. Nevertheless, important questions such as, “How can streaks lead to transition-onset?”, and “What is the transition mechanism with both streaks and K-H instability?”, remain unanswered.

The main discussion of this thesis has been divided into four sections. First, the numerical set-up for the current investigation is discussed in chapter 4. The Large Eddy Simulation (LES) approach, with a dynamic subgrid-scale (SGS) turbulence model, is employed to investigate the current flow field. The predicted time-mean flow field has a good agreement with the experimental observations and previous numerical predictions. Stability analyses have shown that the separated-flow transition in the 0%-FST case possessed a K-H frequency peak, whereas no frequency peak is detected in the 3%-FST case. Instead, streaks exist in the boundary layer up to the transition-onset location. From the flow visualisation, the span-wise K-H rollers found in the 0%-FST case have been severely disrupted in the 3%-FST case. This has resulted in part-span 2D rollers, rapidly developing into a 3D motion. Consequently, the usual secondary instability stage is bypassed, followed by weaker vortex shedding. Current analyses have revealed that both K-H instability and streak-related instability are at work.

Second, the effect of free-stream turbulence intensity (FSTI) on separated-flow transition is investigated in Chapter 5. In total, four levels of FST are studied and compared.

The separation bubble characteristics are found to be sensitive to the increased FSTI. Both separation bubble length and height reduce when FSTI increases. A similar relation with FSTI is observed from the transition onset location. It moves forward when FSTI increases, which is believed to be caused by the reduced length of the separated shear layer. This is due to streaks propagating inside the boundary layer and through the transition process, interrupting growth of the separated shear layer and promoting early transition. In the highest FSTI case (8.0% FST) under investigation, a separation bubble and vortex shedding can be observed, indicating the coexistence of both streak instability and K-H instability in the transition process. However, the former is found to be a much stronger transition mechanism than the latter.

In the third discussion, Proper Orthogonal Decomposition (POD) has been employed to analyse the current separated-flow transition in Chapter 6. From the POD analyses, results have confirmed the coexistence of both streak instability and K-H instability in the 3%-FST case. The streak instability is found to dominate in the current separated-flow transition. In the power spectral density analyses of the POD corresponding time-coefficients, the K-H frequency peak has been detected. Nevertheless, the K-H instability is considered as a localised activity. Both the outer- and inner-streak instability modes normally found in the bypass transition exist in the current separated-flow transition. The differences between these two streak instability modes have been clearly demonstrated by the POD mode visualisation.

In Chapter 7 of the final discussion, flow visualisation and 2D particle tracking have been employed to investigate the two modes of streak instability in the current separated-flow transition. Differences between the current two streak instability modes and those from the bypass transition have been identified. Analogous to the bypass transition, the inner mode originates from shear between a high-speed streak and below low-speed fluid, whereas the outer mode is caused by shear between a lifted low-speed streak and the high-speed free-stream flow. In contrast to the bypass transition, the inner mode streak instability is found to have a similar instability mechanism to the K-H instability. Part-span K-H roller can be a result of inner mode streak instability. For the outer mode, instability arises due to the formation of ring-like vortices warping around the low-speed streak. These vortices are believed to be the precursor to the hairpin vortices. Initial breakdowns of both streak instability modes are via the varicose breakdown pattern.

Declaration

I hereby declare that this thesis was written by myself, that the underlying research is original and my own unless otherwise stated, and that this thesis has not been and will not be submitted in whole or in part to another University for the award of any other degree.

Signature:

HuaJun Li

Acknowledgements

First, I would like to thank my main supervisor, Professor Martin Rose, for all the guidance and support. He has given a lot of valuable advice and feedback for this PhD to become possible.

I also greatly appreciate the support from Professor Zhiyin Yang. Without his valuable advice and feedback, this PhD would not have been achievable.

Many thanks also for the valuable advice given by Dr. Esra Sorguven on large-dddy simulation and data representation.

A special thank you goes to colleagues in the Thermal-Fluid Mechanics Research Centre (TFMRC) - Mr Harri Koivisto, Dr. Rahul Rajasekharan, Mr Daniel Payne, Mr Thomas Irps, Dr. Yeru Shang and Mrs Peiying Sun - for all the useful conversations and supports.

I would like to express my special appreciation and thanks to my parents for their support and understanding during my PhD.

Last but not least, I would like to say a heartfelt thank you to my beloved wife, Dr. Nan Zheng, for her patience, understanding, and endless support over the period of my PhD, and my to beloved daughter, Doris Li.

Preface

The boundary layer separate flow transition under 3% free-stream turbulence and adverse pressure gradient has been investigated in the current thesis. Work from this thesis has been published in the following papers:

1. Hua J. Li and Z. Yang, 2019, Separated boundary layer transition under pressure gradient in the presence of free-stream turbulence, *Physics of Fluids*, 31(10), 104106(2019)
2. Hua J. Li and Z. Yang, 2016, Numerical study of separated boundary layer transition under pressure gradient, Conference: The 12th International Conference on Heat Transfer, Fluid Mechanics and Thermodynamics, Malaga, Spain

Contents

List of Figures	20
List of Tables	21
1 Introduction	22
1.1 Overview	22
1.2 Routes to Boundary Layer Transition	24
1.3 Natural Transition	25
1.4 Bypass Transition	26
1.5 Separated-flow Transition	26
1.6 Separated-flow Transition under Elevated FST	27
2 Literature Review	29
2.1 Large-Eddy Simulation and Turbulence Modelling	29
2.2 Dynamic SGS Turbulence Model	32
2.3 Proper Orthogonal Decomposition (POD)	34
2.3.1 The Direct Method POD	35
2.3.2 The Snapshot Method POD	38
2.4 Vortex Identification Methods	39
2.5 Boundary Layer Transition	40
2.5.1 Bypass Transition	40
2.5.2 Separated-flow Transition	43
2.6 Overview and Objectives of the Present Research	47
3 Numerical Details	49
3.1 The DELTA Solver	49

3.1.1	Solution Procedures - SIMPLE Algorithm	50
3.1.2	Improved Rhie-Chow Interpolation	51
3.1.3	Free-stream Turbulence Generation	53
3.1.4	Convective Outflow Boundary Condition	54
3.2	DELTA Solver Improvements	55
3.3	Computational Resources	57
3.4	Implementation of POD method	58
4	Separated-flow Transition on Flat Plate	59
4.1	Introduction	59
4.2	Simulation Configuration and Overview	60
4.3	Computational Mesh Analysis	64
4.4	Flow Characteristics	67
4.4.1	Mean Flow Characteristics	67
4.4.2	T-S Instability	72
4.4.3	K-H Instability	74
4.5	Summary	86
5	Effect of Free-stream Turbulence Intensity	88
5.1	Introduction	88
5.2	The Simulation Configuration	88
5.3	Time-averaged Flow Characteristics	90
5.3.1	Time-averaged Wall Shear Stress	90
5.3.2	Boundary Layer Shape Factor	93
5.3.3	Time-averaged Velocity Profiles	94
5.3.4	Time-averaged Velocity Distribution	95
5.3.5	Displacement and Momentum Thickness	96
5.3.6	The Maximum RMS Velocities	98
5.4	Flow Visualisation	100
5.5	Summary	103
6	Proper Orthogonal Decomposition (POD) Analysis of Separated-flow Transition	105
6.1	Introduction	105

6.2	POD Analysis Sampling Locations	106
6.3	POD Results	107
6.3.1	POD Results - 0%-FST Case	107
6.3.2	POD Results - 3%-FST Case	114
6.4	Summary	134
7	Boundary-Layer Streak Instability	137
7.1	Introduction	137
7.2	Streak Identification	137
7.3	Vortex Identification Methods	140
7.4	Streak Instability - Overview	140
7.5	Streak Instability - Inner Mode	142
7.5.1	Three-dimensional Flow Visualisation	142
7.5.2	2D Particle Tracking - Inner Mode	145
7.6	Streak Instability - Outer Mode	148
7.6.1	Three-dimensional Flow Visualisation	149
7.6.2	2D Particle Tracking - Outer Mode	151
7.7	Summary	154
8	Conclusion	155
8.1	Conclusion	155
8.2	Scope for Future Research	159

List of Symbols

Δ	Grid filter length
Δt	Time-step size
Δx^+	Non-dimensional stream-wise mesh size
Δy^+	Non-dimensional wall-normal mesh size
Δz^+	Non-dimensional span-wise mesh size
δ^*	Displacement thickness
δ_{100}	100% boundary layer thickness
δ_{95}	95% boundary layer thickness
δ_{99}	99% boundary layer thickness
λ	Eigenvalue
λ_2	λ_2 -criterion
μ_t	Turbulence viscosity
μ	Dynamic viscosity
ν	Kinematic viscosity
$\overline{\mathbf{U}}$	Averaged velocity field from POD
$\overline{S_{ij}}$	Strain rate tensor
Φ	Eigenvector matrix
Φ_s	Spatial coefficient from Snapshot Method

ρ	Density
$\sqrt{u'u'}$	Stream-wise root-mean-square velocity
$\sqrt{v'v'}$	Wall-normal root-mean-square velocity
$\sqrt{w'w'}$	Span-wise root-mean-square velocity
τ_{ij}^r	Residual stress tensor
τ_w	Wall-shear stress
θ^*	Momentum thickness
$\tilde{\Delta}$	Sub-test filter length
\tilde{S}_{ij}	Subtest strain rate tensor
$ \bar{S} $	Magnitude of the strain rate scalar
$ \tilde{S} $	Magnitude of the subtest strain rate scalar
A	Time-coefficient matrix
$a_k(t)$	Transient time-coefficient
C	Covariance matrix
c	Wave speed
C_d	Dynamic SGS turbulence model constant
C_s	Smagorinsky SGS turbulence model constant
C_{cor}	Correlation matrix
C_{ij}	Cross term
d	Flat plate thickness
dP	Change in pressure
dt	Change in time
dx, dy, dz	Change in different directions

$f_{KHunstable}$	Frequency unstable to K-H wave
$f_{TSunstable}$	Frequency unstable to T-S wave
H	Shape factor
h	Shear layer thickness
h_{bubble}	Height of the separation bubble
K	Free-stream acceleration parameter
k	POD mode
k_n	Wave number
l_{bubble}	Length of the separation bubble
L_{ij}	Leonard term
n	A superscript denotes a variable from the current iteration/time-step
$n + 1$	A superscript denotes a variable from the next iteration/time-step
N_c	Number of columns
N_r	Number of rows
N_x	Number of nodes in stream-wise direction
N_y	Number of nodes in wall-normal direction
N_z	Number of nodes in span-wise direction
Q	Q-criterion
R_i	Richardson number
R_{ij}	Reynolds term
Re_{δ^*}	Reynolds number in terms of displacement thickness
Re_{s_o}	Reynolds number at nominal exit
s	Seconds

S_0	Test section length
St_θ	Vortex-shedding Strouhal number
t	Time in seconds
T_{ij}^r	Sub-test stress tensor
TR_{onset}	Transition onset location
Tu	Free-stream turbulence intensity near the flat plate leading edge
Tu_2	Free-stream turbulence intensity before boundary layer separation
U	Velocity field
u', v', w'	Instantaneous stream-wise, wall-normal, span-wise fluctuation velocity
u, v, w	Instantaneous stream-wise, wall-normal, span-wise velocity
U_s^T	Transposed snapshot matrix
U_m, U_{mean}	Time-averaged velocity field
U_s	Snapshot matrix
U_{fs}	Free-stream velocity at the edge of the boundary layer
U_{in}	Inflow velocity
U_{out}	Outflow velocity at nominal exit
\tilde{U}_k	Velocity field from a POD Mode k
CFD	Computational fluid dynamics
CFL	Courant-Friedrichs-Lewy number
DELTA	CFD Solver - DELTA
DNS	Direct Numerical Simulation
EXP	Experiment
FDR	Fourteen Data Rate, 14Gb/s data rate per lane

FST Free-Stream turbulence

FSTI Free-Stream turbulence intensity

K-H Kelvin-Helmholtz instability

LE Leading edge

LES Large-Eddy Simulation

LPT Low-Pressure turbine

MPI Message Passing Interface

NFS Network File System

POD Proper Orthogonal Decomposition

QUICKS Quadratic Upwind Interpolation for Convective Kinematics

RDMA Remote Direct Memory Access

ReaX Boundary layer reattachment location

RMS Root mean square

SepX Boundary layer separation location

SGS Subgrid-scale

SIMPLE Semi Implicit Method for Pressure Linked Equations

STS Subtest-scale

T-S Tollmien-Schlichting instability

TECPLOT CFD Post-processing tool

URANS Unsteady Reynolds Averaged Navier-Stokes Simulation

List of Figures

1.1	Routes to boundary layer transition flowchart. <u>Brown colour</u> : Natural transition; <u>Blue colour</u> : Separated-flow transition; <u>Red colour</u> : Separated-flow transition under elevated FST; <u>Green colour</u> : Bypass transition.	24
1.2	Schematic of boundary layer natural transition.	25
1.3	Separated-flow transition and laminar separation bubble.	27
2.1	A typical turbulence energy spectrum and definition of different turbulence length scales.	30
2.2	Elliptical distribution of a dataset.	35
2.3	<u>Gold</u> : High-speed streaks, <u>Blue</u> : Low-speed streaks, <u>Green</u> : Breakdown vortices.	43
3.1	An example of stream-wise stencil around a cell, x_i , in the immersed plane.	54
3.2	Free-stream turbulence spectrum near the flat plate leading edge.	54
4.1	Schematic of the computational domain.	60
4.2	A: An overview of the computational mesh with mesh points omitted for better visualisation. <u>Regions coloured in red and the exit domain</u> : every 4th point in x and y is shown. <u>The remaining region</u> : every 4th point and every 2nd point in x and y are shown respectively. B: Detailed view of the computational mesh (all points shown) around the flat plate leading edge that is highlighted by blue edges in A.	62
4.3	The temporal change of separation bubble characteristics. Left y-axis: Scales for the separation and reattachment locations with symbol (\circ). Right y-axis: Scales for the bubble length, l_{bubble} , with symbol (Δ).	63
4.4	Comparison of velocity profiles between the two cases.	66
4.5	Comparison of velocity distribution between the two cases.	66

4.6	Time-mean u -velocity contour of the computational domain at mid-plane (only the mesh blocks next to the plate surface are shown). For the purposes of providing a clear illustration, the wall-normal dimension has been scaled to 1.5 times the stream-wise dimension.	67
4.7	Solid line: Time-mean stream-wise wall shear stress from the current LES calculation. <u>Symbols</u> : Separation and reattachment locations. Current LES: (‘ · ’), Experiment data: Coull and Hodson (2011) (‘ ◦ ’), LES data: Nagabhushanan et al. (2013) (‘ Δ ’).	68
4.8	<u>Black colour</u> : Time-mean velocity profiles at $x/S_0 = 0.50, 0.60, 0.65, 0.70, 0.75, 0.80, 0.85, 0.90, 0.95, 1.00$. <u>Gray colour</u> : Boundary layer thickness at δ_{95} . <u>Symbols</u> : Current LES: (‘ - ’), Experiment data (Coull and Hodson (2011)): (‘ ◦ ’), LES data (Nagabhushanan et al. (2013)): (‘ - - ’).	69
4.9	Free-stream velocity distribution along the flat plate surface. <u>Symbols</u> : Current LES: (‘ - ’), Experiment data (Coull and Hodson (2011)): (‘ ◦ ’), LES data (Nagabhushanan et al. (2013)): (‘ - - ’).	70
4.10	<u>Left</u> : Flat plate (placed vertically) and PSD sampling points (‘ ◦ ’) within the boundary layer showing by u -velocity line contour. <u>Right</u> : Displaced frequency spectra of u' -velocity at stream-wise locations between $x/S_0 = 0.10$ and $x/S_0 = 0.65$. Dash line: the T-S wave maximum amplification frequency, $f_{TS(unstable)} = 125\text{Hz}$, predicted by the correlation from Equ. 4.2. In the vertical scale of the displaced frequency spectra plot, one increment between two major ticks is 1.0×10^5	73
4.11	Boundary layer velocity profiles in the 3%-FST case. <u>Solid line</u> : Velocity profiles ($U_{mean}, \sqrt{u'u'}, \sqrt{v'v'},$ and $\sqrt{w'w'}$) between $x/S_0 = 0.40$ and $x/S_0 = 0.97$. <u>Dash line</u> : Boundary layer edge. <u>Dotted line</u> : Boundary layer profile point of inflection ($d^2U/dy^2 = 0$). <u>Symbol</u> : The maximum value of RMS velocity profile.	75
4.12	Boundary layer velocity profiles in 0%-FST case. <u>Solid line</u> : Velocity profiles ($U_{mean}, \sqrt{u'u'}, \sqrt{v'v'},$ and $\sqrt{w'w'}$) between $x/S_0 = 0.40$ and $x/S_0 = 0.97$. <u>Dash line</u> : Boundary layer edge. <u>Dotted line</u> : Boundary layer profile point of inflection ($d^2U/dy^2 = 0$). <u>Symbol</u> : The maximum value of RMS velocity profile.	76

4.13	Maximum RMS velocities along the stream-wise direction. $(\sqrt{u'u'})_{max}/U_{out}$: (' - '); $(\sqrt{v'v'})_{max}/U_{out}$: (' - - '); $(\sqrt{w'w'})_{max}/U_{out}$: (' - - - ').	77
4.14	Instantaneous wall-normal and span-wise velocity components at five consecutive time steps.	78
4.15	' Ri ': is the Richardson number, ' k_n ': is the wave number, ' h ': is the free shear layer thickness, and ' c ': is the velocity at the point of inflection.	79
4.16	u' -velocity frequency spectra at two stream-wise locations of $x/S_0 = 0.78$ and $x/S_0 = 0.81$, and at span-wise location $z/S_0 = 0.098$ for the 0%-FST case.	81
4.17	<u>Left</u> : Flat plate (placed vertically) and PSD sampling points (' \circ ') within the boundary layer showing by u -velocity line contour. <u>Right</u> : Displaced frequency spectra of u' -velocity at stream-wise locations between $x/S_0 = 0.61$ and $x/S_0 = 0.81$. In the vertical scale of the displaced frequency spectra plot, one increment between two major ticks is 1.0×10^5	82
4.18	u' -velocity frequency spectra at two stream-wise locations of $x/S_0 = 0.70$ and $x/S_0 = 0.72$, and at span-wise location $z/S_0 = 0.098$ of the 3%-FST case.	83
4.19	Q-criterion iso-surface flow visualisation of the transition process between the 0%-FST and the 3%-FST cases. Gold colour: Iso-surfaces at Q-criterion value of 2000, Dark colour (only in the 3%-FST case): Visualisation of streaks using the wall-normal vorticity.	84
4.20	Separated shear layer vortex shedding in the 3%-FST case with the development of a vortex cascade.	85
5.1	Comparison of wall shear stress under the influence of different FSTI. Symbols are showing the boundary layer separation and reattachment locations respectively located on the left-hand-side and right-hand-side.	90
5.2	Comparison of boundary layer shape-factor curves under the influence of different FSTI.	94
5.3	Comparison of velocity profiles under the influence of different FSTI.	95

5.4	Comparison of velocity distribution under the influence of different FSTI. For each curve, the first symbol indicates the separation location, the second symbol indicates the transition onset location, and the third symbol indicates the reattachment location. This order follows the free-stream flow direction.	96
5.5	Comparison of boundary layer thickness parameters under the influence of different FSTI.	97
5.6	Maximum RMS velocities along the stream-wise direction. $(\sqrt{u'u'})_{max}/U_{out}$: (' - '); $(\sqrt{v'v'})_{max}/U_{out}$: (' - - '); $(\sqrt{w'w'})_{max}/U_{out}$: (' - - ').	99
5.7	Mid-span xy -plane flow visualisation of Case-4.7. Contour shows vorticity magnitude with values between 0 and 800.	101
5.8	Mid-span xy -plane flow visualisation of Case-8.0. Contour shows vorticity magnitude with values between 0 and 800.	102
6.1	Sampling plane locations in the POD analyses. The displayed flow field is within the first layer of blocks next to the flat plate surface, not the entire computational domain. <u>White line</u> : Constant spanned xz -plane. <u>Black line</u> : Enclosing the area of a xy -plane; <u>Line contour</u> : temporal averaged span-wise vorticity field.	106
6.2	Energy distribution of the first 10 POD modes from the xz -plane flow field (0%-FST case).	108
6.3	POD contour of the u' -velocity from the xz -plane flow field (0%-FST case).	109
6.4	Time-coefficient PSD of the xz -plane flow field (0%-FST case).	110
6.5	Energy distribution of the first 10 POD modes from the mid-span xy -plane flow field ($z/S_0 = 0.10$, 0%-FST case).	111
6.6	POD contour of the u' -velocity from the mid-span xy -plane flow field ($z/S_0 = 0.10$ 0%-FST case).	112
6.7	Time-coefficient PSD of the mid-span xy -plane flow field ($z/S_0 = 0.10$, 0%-FST case).	113
6.8	POD contour of the u' -velocity from the xz -plane flow field (3%-FST case).	114
6.9	Energy distribution of the xz -plane flow field (3%-FST case).	116
6.10	Time-coefficient PSDs of the xz -plane flow field (3%-FST case).	116
6.11	POD contour of the v' -velocity from the xz -plane flow field (3%-FST case).	118

6.12	POD contour of the w' -velocity from the xz -plane flow field (3%-FST case).	120
6.13	POD contour of the pressure fluctuation from the xz -plane flow field. Mode-1 of the pressure fluctuation POD contour has predominantly captured the global pressure fluctuation due to the mass flow imbalances between the upper and the lower passage of the computational domain. As a result, its energy contribution has not been accounted for in the energy distribution calculation (3%-FST case).	121
6.14	Energy distribution of the mid-span xy -plane flow field ($z/S_0 = 0.10$).	122
6.15	POD contour of the u' -velocity from the mid-span xy -plane flow field ($z/S_0 = 0.10$).	123
6.16	Time-coefficient PSDs from the mid-span xy -plane flow field ($z/S_0 = 0.10$).	125
6.17	Energy distribution of the left-quarter-span xy -plane flow field ($z/S_0 = 0.05$).	126
6.18	POD contour of the u' -velocity from the left-quarter-span xy -plane flow field ($z/S_0 = 0.05$).	127
6.19	Time-coefficient PSDs from the left-quarter-span xy -plane flow field ($z/S_0 = 0.05$).	128
6.20	POD contour of the u' -velocity from the right-quarter-span xy -plane flow field ($z/S_0 = 0.15$).	130
6.21	POD contour of the w' -velocity field from the left-quarter-span flow field ($z/S_0 = 0.10$).	131
6.22	POD contour of the w' -velocity field from the left-quarter-span flow field ($z/S_0 = 0.05$).	132
6.23	POD contour of the u' -velocity field from the mid-span flow field ($z/S_0 = 0.10$). <u>Solid lines</u> : High-speed streaks ($+u'$); <u>Dash lines</u> : Low-speed streaks ($-u'$).	133
6.24	POD contours of the u' -velocity field from the left-quarter-span flow field ($z/S_0 = 0.05$). <u>Solid lines</u> : High-speed streaks ($+u'$); <u>Dash lines</u> : Low-speed streaks ($-u'$).	134
7.1	Normalised velocity fluctuation, u' , line contour of xz -plane at $y/S_0 = 0.0008, 0.0024, 0.0048, 0.0070, \text{ and } 0.0124$ of an arbitrary time step.	138

7.2	u' -velocity iso-surfaces to demonstrate boundary layer streaks in the three-dimensional space.	139
7.3	Comparison between the λ_2 -criterion and Q-criterion on identifying coherent flow structures from the current separated-flow transition and breakdown.	140
7.4	A transient contour plot illustrates the evolution of a typical inner mode streak instability in the 2D space.	143
7.5	A transient iso-surfaces plot illustrates the evolution of a typical inner mode streak instability in the 3D space. <u>Red</u> : High-speed streak ($+u'$). <u>Blue</u> : Low-speed streak ($-u'$). <u>Gold</u> : Q-criterion iso-surface.	144
7.6	Velocity profiles (u and u') at $x/S_0 = 0.70$ and $t = 75.7200(s)$	145
7.7	Particle trajectory inside the high-speed streak that leads to the inner mode streak instability.	146
7.8	Particle-velocity information along the particle trajectory inside the high-speed streak that leads to the inner mode streak instability.	147
7.9	A transient contour plot illustrates the evolution of a typical inner mode streak instability in the 2D space.	148
7.10	A transient iso-surfaces plot illustrates the evolution of a typical outer mode streak instability in the 3D space. <u>Red</u> : High-speed streak ($+u'$). <u>Blue</u> : Low-speed streak ($-u'$). <u>Gold</u> : Q-criterion iso-surface.	150
7.11	Velocity profiles (u and u') at $x/S_0 = 0.75$ and $t = 75.27(s)$	151
7.12	Particle trajectory inside the low-speed streak that leads to the outer mode streak instability.	152
7.13	Particle velocity information along the particle trajectory inside the low-speed streak that leads to the outer mode streak instability.	153

List of Tables

4.1	Flow configuration and numerical details.	64
4.2	Details of two cases under investigation, (“ b ” : the base-line case; “ * ” : this value is calculated based on the three-dimensional mesh sizes around the separation bubble).	65
4.3	Frequency ranges are unstable to K-H instability. (‘ * ’ : the transition-onset location).	80
5.1	Non-dimensional mesh sizes in four simulations with different FSTI. In this table, Tu : free-stream turbulence intensity sampled near the flat plate LE; Tu_2 : free-stream turbulence intensity sampled before boundary layer separation at $x/S_0 = 0.576$	89
5.2	Separation bubble characteristics in different cases. In this table, Tu : free-stream turbulence intensity sampled near the flat plate LE; Tu_2 : free-stream turbulence intensity sampled before boundary layer separation at $x/S_0 = 0.576$; $SepX$: separation location; $ReaX$: reattachment location; l_{bubble} : separation bubble length; h_{bubble} : separation bubble maximum thickness; TR_{onset} : transition onset location.	91

Chapter 1

Introduction

1.1 Overview

The boundary layer transition process from laminar to turbulent flow is extremely important in many engineering applications, as its behaviour can greatly influence a system's efficiency. For instance, in a modern multi-shaft turbo fan engine, the specific fuel consumption and efficiency of the engine can be greatly influenced by the low-pressure turbine (LPT) blade design. The LPT rotor is the only component that drives a large-diameter stage-1 compressor fan. This LPT rotor converts the upstream high velocity and high temperature gas into shaft power. During operation, each LPT blade is under significant aerodynamic and thermal load. Therefore, by understanding and carefully controlling the boundary layer transition process on the LPT blade surface, the profile loss can be reduced, hence increasing the LPT rotor efficiency. The LPT blade's lifespan can also be greatly extended when carefully controlling the blade surface heat transfer rate, which is also mainly controlled by the boundary layer transition process. Normally, one section of the LPT rotor can consist of as many as 96 blades in order to spread the required load. Therefore, any small improvement to the LPT blade design can have significant impacts on the overall engine efficiency. Also, by increasing the performance of a single blade, a reduction in blade count can result in significant engine weight reduction. [Cobley et al. \(1997\)](#) reported that a 20% reduction in blade count can be achieved by careful control of the boundary layer transition process alone.

Depending on the size of the LPT rotor, it can operate in a wide range of Reynolds numbers and incident angles. When operating under low Reynolds number flow condi-

tions, the boundary layer may separate laminarly and it inviscidly becomes turbulent, but without a reattachment. Such a transition process can incur a significant loss. To design an LPT blade operating within such a wide range of Reynolds number flow conditions requires a good understanding of the boundary layer transition process.

The modern “high-lift” LPT blade design features a closed laminar separation bubble on the blade suction side surface. The LPT blade efficiency and the heat transfer rate are greatly influenced by the size of this laminar separation bubble which is mainly controlled by the boundary layer separated-flow transition process. A full understanding of such a transition process is of significant practical interest. Therefore, advancing the current understanding of such a transition process is the main context of the current study.

1.2 Routes to Boundary Layer Transition

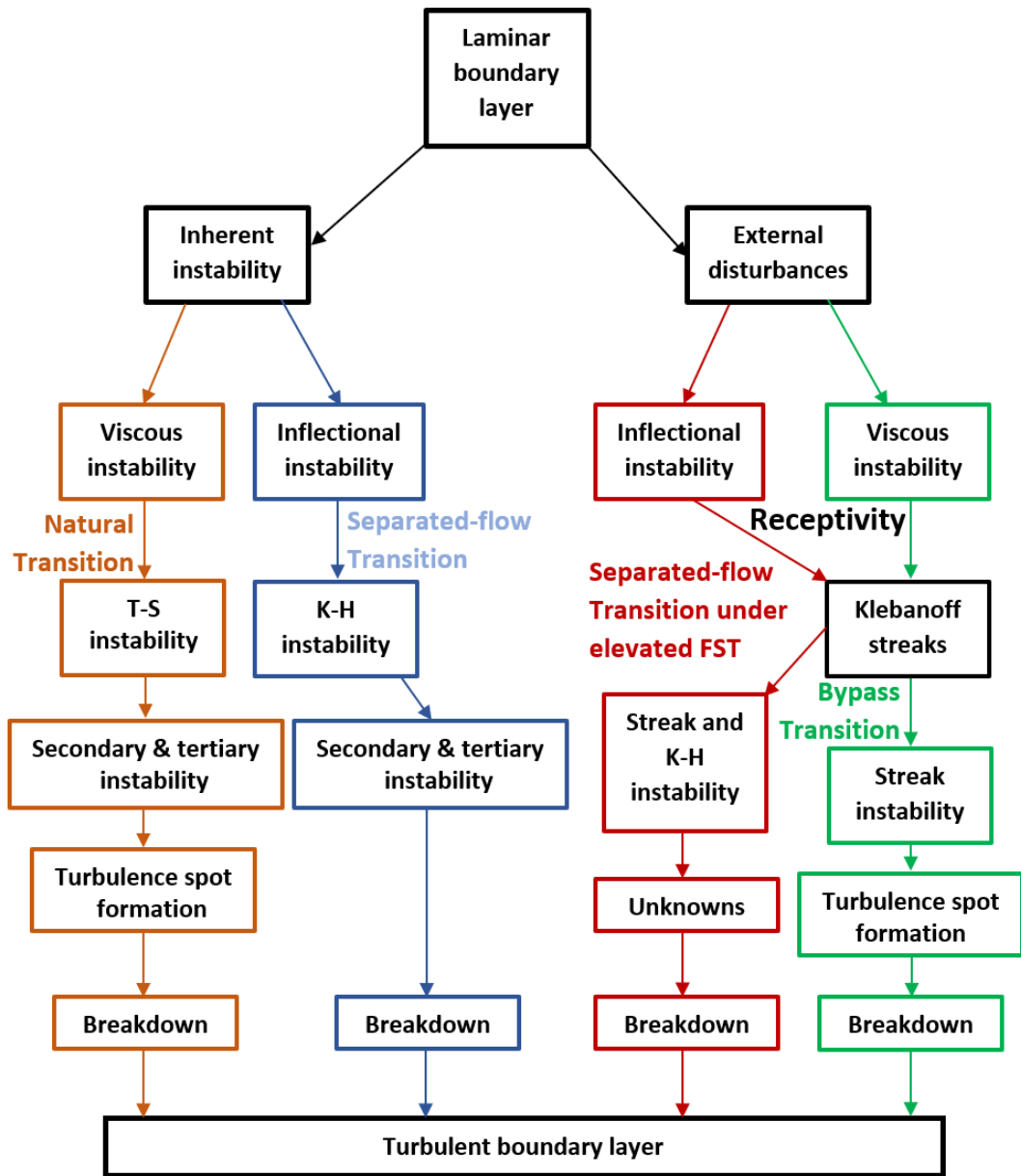


Figure 1.1: Routes to boundary layer transition flowchart. Brown colour: Natural transition; Blue colour: Separated-flow transition; Red colour: Separated-flow transition under elevated FST; Green colour: Bypass transition.

The boundary layer transition process is an extremely sensitive and complex flow phenomenon whose behaviours are particularly difficult to predict. [Mayle \(1991\)](#) conducted an extensive review of the three main routes to transition, as shown in Figure 1.1. These are known as boundary layer natural transition (coloured in brown), bypass transition

(coloured in green), and separated-flow transition (coloured in blue). There is another route to transition that has not been widely recognised, which is known as separated-flow transition under elevated FST. This route to transition is not yet fully understood and the current study will provide further clarification on this complex transition process. A brief introduction to different transition routes will be given below to support understanding of the current context.

1.3 Natural Transition

Natural transition (coloured brown in Figure 1.1) is a viscous instability normally found in a developing attached boundary layer on a zero roughness surface and under a minimal level of FST. According to [Schlichting \(1979\)](#), a typical natural transition process can be divided into several stages, as depicted in Figure 1.2.

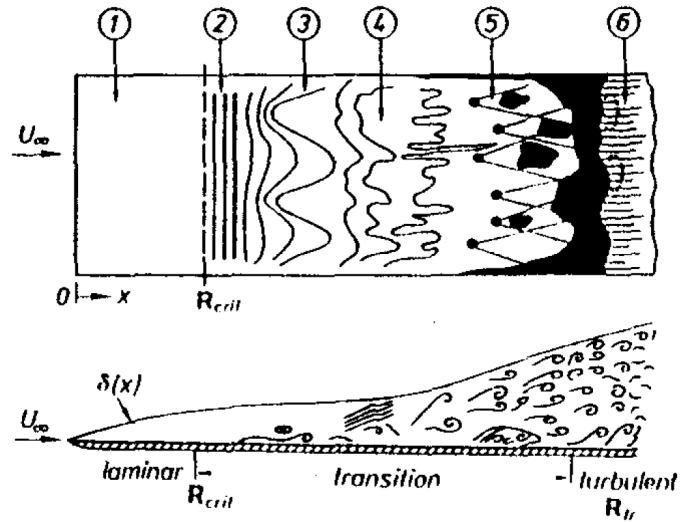


Figure 1.2: Schematic of boundary layer natural transition.

This transition process usually starts with a selective amplification of weak background disturbances and results in the formation of Tollmien-Schlichting (T-S) instability waves which appear as a series of two-dimensional (2D) span-wise rollers. The next stage (secondary instability stage) of the transition process starts when the Tollmien-Schlichting waves have reached a critical speed (1% of the freestream convective speed). In this stage, the 2D span-wise rollers are distorted by the non-linear effects, leading to an increase of vorticity inside the boundary layer resulting in the formation of loop vortices. The secondary instability stage of the T-S wave can be classified into K-type ([Klebanoff et al.](#)

(1961a)) and H-type (Herbert (1983)). The K-type instability has an identical wavelength to the T-S wave span-wise wavelength, whereas the H-type instability has half the T-S wave span-wise wavelength. Generally, the length of the secondary instability stage is approximately five wavelengths of the T-S wave (Klebanoff et al. (1961a)). The final stage of the transition process is the formation of turbulent spots (Emmons (1951)) from regions of peak fluctuations. Ultimately, these turbulent spots coalesce together while propagating downstream to form a continuous region of turbulent flow.

1.4 Bypass Transition

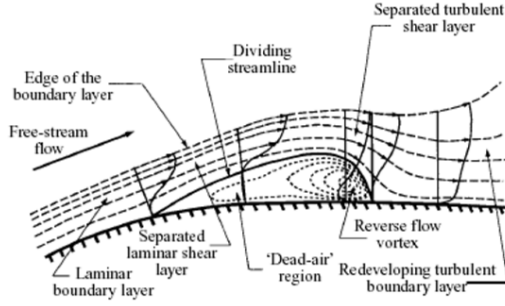
Bypass transition (coloured green in Figure 1.1) can occur when FST intensity increases to a critical level with a few stages of the classical natural transition route bypassed. These are stages 2, 3, and 4 (in Figure 1.2), known as slow T-S wave developing stages. As a result, transition can happen rapidly and begins with direct turbulent spot inception which is stage-5 shown in Figure 1.2. Generally, there are four stages of bypass transition, namely:

1. Boundary layer receptivity to free-stream turbulence, in which low-frequency energy from the free-stream turbulence packets penetrates the boundary layer through shear sheltering.
2. The low-frequency energy entering the boundary layer can result in the formation of streaks that propagate inside the boundary layer.
3. Development of the streak instability stage, caused by the interaction of different magnitude streaks.
4. Instability rapidly increases and causes the formation of a turbulence spot. The burst of turbulence spots leads to the boundary layer becoming turbulent.

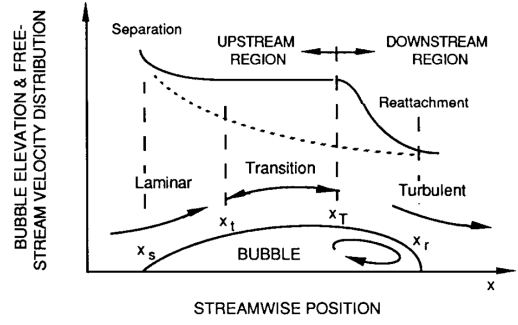
1.5 Separated-flow Transition

As shown in Figure 1.3a, on a curved surface such as an LPT blade suction side surface, the boundary layer on the forward portion of the surface is under a favourable pressure gradient and strong acceleration, resulting in an attached boundary layer being normally found in this region.

When there is a sudden change of surface curvature, or a switch to an adverse pressure



(a) Separated-flow transition on curved surface (O'Meara and Mueller, 1987).



(b) Transition location of a separation bubble (Mayle 1991).

Figure 1.3: Separated-flow transition and laminar separation bubble.

gradient, the attached laminar boundary layer separates from the surface. Intermittently, reversed fluid is found under the separated shear layer, which leads to the formation of a “Dead-air” region. The time-mean velocity profile at this location exhibits a point of inflection and the boundary layer is considered inviscidly unstable to any small disturbance. Amplification of these disturbances can lead to the onset of transition and formation of the primary instability. The approximate location of the transition can be found in Figure 1.3b. The dominant instability mechanism is the well-known Kelvin-Helmholtz (K-H) instability, or the so-called K-H wave. Normally, the instability wave amplitude grows linearly and is then followed by an exponential growth. Once the growth of this instability wave is saturated, transition develops into the so-called secondary instability stage, in which two-dimensional vortex shedding can be observed. However, this stage is less understood. Frequently, three-dimensional vortical structures are formed before the turbulent breakdown.

1.6 Separated-flow Transition under Elevated FST

Another route to transition can be found when separated-flow transition happens in a high FST environment. This transition process is not yet fully understood. Nevertheless, the current understanding can provide an overview of this transition process. Similar to the initial stage of bypass transition, boundary layer streaks are formed due to receptivity of free-stream turbulence energy. Meanwhile, the boundary layer separates due to the local adverse pressure gradient. As a result, both boundary layer streaks and K-H instability

exist in the separated shear layer, in which transition onset is triggered by both the streak instability and the K-H instability. Depending on the level of FST, one of these two instabilities can dominate in the transition process. The break down process can also be different to those originating from separated-flow transition and bypass transition due to the existence of multiple instability mechanisms. As the current understanding on this route to transition is very limited, the objective of this study is to advance the understanding of such a transition process.

Chapter 2

Literature Review

2.1 Large-Eddy Simulation and Turbulence Modelling

The governing equations involved in the current numerical study are the unsteady Navier-Stokes equations. As the base-line experimental work was a low-speed experiment with velocity below $6.0(m/s)$, only the incompressible form of the governing equations is considered here, in which density is assumed to be constant. The general form is defined as below, with Eqn. 2.1 and Eqn. 2.2 respectively maintaining the mass and momentum conservation. They are therefore known as the continuity and momentum equations.

$$\frac{\partial u_i}{\partial x_i} = 0 \quad (2.1)$$

$$\frac{\partial u_i}{\partial t} + u_j \frac{\partial u_i}{\partial x_j} = -\frac{1}{\rho} \frac{\partial P}{\partial x_i} + \frac{\partial}{\partial x_j} \left(\nu \frac{\partial u_i}{\partial x_j} \right) \quad (2.2)$$

For the purpose of minimising the computational cost without huge penalties in terms of resolution and accuracy, large-eddy simulation (LES) is employed here to solve the Navier-Stokes equations. Its cost-effectiveness is between the Unsteady Reynolds Averaged Navier-Stokes (URANS) approach and the Direct Numerical Simulation (DNS) approach. LES provides more information on the flow field than can URANS; meanwhile, it requires fewer computational resources than does DNS. LES achieves its high effectiveness by resolving only the large-scale fluid motions, and by modelling the small-scale ones. Most importantly, LES has been widely employed and has proved to be capable of transition prediction which is the scope of the current study.

In the current LES approach, the implicit filtering is employed. The computational

grid functions as a low-pass filter, separating the flow into resolved scales and unresolved scales, as shown in Figure 2.1. Turbulent flow with the length scale larger than the control volume is fully resolved. The energy spectrum produced by this range of fluid contributes the majority of the turbulence kinetic energy and is known as the resolved scale. For the unresolved scale, the turbulent flow has a smaller scale than the control volume. These scales cannot be resolved directly by the governing equations. In order to consider their contribution to the overall energy spectrum, they are modelled by the so-called subgrid-scale (SGS) turbulence model. The SGS turbulence model is also responsible for summing up the energy transfer between the two scales. Hence, its accuracy has a significant impact on the LES prediction. Normally, the cut-off point of a typical LES calculation is within the Inertial scale. This is the parameter that defines the control-volume size.

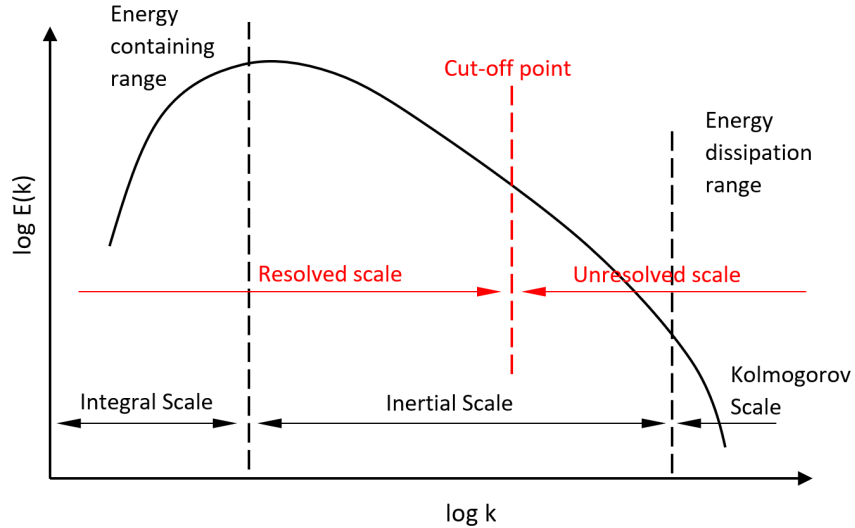


Figure 2.1: A typical turbulence energy spectrum and definition of different turbulence length scales.

In LES, the general form of the governing equations is transformed into a set of filtered equations, where the filtered term is denoted by an over line ‘ $\overline{\quad}$ ’. The filtered Navier-Stokes equations are written below as:

$$\overline{\frac{\partial u_i}{\partial x_i}} = 0 \quad (2.3)$$

$$\overline{\frac{\partial u_i}{\partial t}} + \overline{u_j \frac{\partial u_i}{\partial x_j}} = -\frac{1}{\rho} \overline{\frac{\partial P}{\partial x_i}} + \overline{\frac{\partial}{\partial x_j} \left(\nu \frac{\partial u_i}{\partial x_j} \right)} \quad (2.4)$$

When solving these equations, the convection term, $\overline{u_j \partial u_i / \partial x_j}$, is not linearly solvable,

and is decomposed into a linear convection term and an extra derivative term according to:

$$\overline{u_i u_j} = \overline{u_i} \overline{u_j} + \tau_{ij}^r \quad (2.5)$$

where, τ_{ij}^r , is the residual stress tensor. The convective term is therefore rewritten as:

$$\overline{u_j \frac{\partial u_i}{\partial x_j}} = \frac{\partial \overline{u_i} \overline{u_j}}{\partial x_j} + \frac{\partial \tau_{ij}^r}{\partial x_j} \quad (2.6)$$

This yields the filtered momentum equation:

$$\frac{\partial \overline{u_i}}{\partial t} + \frac{\partial \overline{u_i} \overline{u_j}}{\partial x_j} = -\frac{1}{\rho} \frac{\partial \overline{P}}{\partial x_i} + \frac{\partial}{\partial x_j} \left(\nu \frac{\partial \overline{u_i}}{\partial x_j} \right) - \frac{\partial \tau_{ij}^r}{\partial x_j} \quad (2.7)$$

After the work of [Clark et al. \(1979\)](#), the residual stress tensor, τ_{ij}^r , can be further simplified using the Leonard (triple) decomposition, which is written as:

$$\tau_{ij}^r = \overline{u_i u_j} - \overline{u_i} \overline{u_j} = \underbrace{\overline{\overline{u_i} \overline{u_j}} - \overline{u_i} \overline{u_j}}_{L_{ij}} + \underbrace{\overline{u_i' u_j'}}_{C_{ij}} + \underbrace{\overline{u_i' u_j'}}_{R_{ij}} \quad (2.8)$$

In Eqn. 2.8, there are new terms introduced by the decomposition operation, in which, L_{ij} is the ‘‘Leonard term’’, C_{ij} is the ‘‘Cross term’’, and R_{ij} is the ‘‘Reynolds term’’. In LES, the interaction within the resolved scale and the bi-directional interaction between the resolved and unresolved scales are assumed to be equal. Therefore, L_{ij} is approximately equal to C_{ij} , whereas R_{ij} , describes the interaction between the sub-grid scales.

Using the Boussinesq eddy viscosity hypothesis, the closure of the equations can be achieved by modelling the residual stress tensor, τ_{ij}^r , which is defined as:

$$\tau_{ij}^r - \frac{1}{3} \tau_{kk} \delta_{ij} = 2\mu_t S_{ij} \quad (2.9)$$

In Eqn. 2.9, the subgrid-scale turbulence viscosity, μ_t , can be modelled by a subgrid-scale turbulence model. For example, the widely used Smagorinsky-Lilly SGS turbulence model is written as:

$$\mu_t = \rho (C_s \Delta)^2 |\overline{S}| \quad (2.10)$$

In Eqn. 2.10, C_s is the universal Smagorinsky constant, and Δ is the filter length and is proportional to the size of the control volume when implicit filtering is used. It is defined as $\Delta = (d_x d_y d_z)^{1/3}$, where d_x , d_y , d_z are dimensions of the control volume. $|\overline{S}|$ is

the magnitude of the strain scalar and is defined as:

$$|\bar{S}| = (2\bar{S}_{ij}\bar{S}_{ij})^{\frac{1}{2}} \quad (2.11)$$

where, \bar{S}_{ij} , is the strain rate tensor and is written as:

$$\bar{S}_{ij} = \frac{1}{2} \left(\frac{\partial u_i}{\partial x_j} + \frac{\partial u_j}{\partial x_i} \right) \quad (2.12)$$

Nevertheless, the widely used Smagorinsky-Lilly SGS turbulence model is found to be too dissipative due to the fixed model constant, C_s . This is not favourable to the transition prediction. For example, the location of separation and reattachment can be over predicted. To overcome this problem, a more advanced dynamic SGS turbulence model is employed here with the model constant C_s varying according to the local flow conditions. The details of this SGS turbulence model will be discussed in Section 2.2.

2.2 Dynamic SGS Turbulence Model

Depending on the flow condition and filter cut-off length of LES calculation, a universal model constant, C_s , with value between 0.1 and 0.23 is normally used in the conventional Smagorinsky-Lilly SGS turbulence model. However, a constant C_s value was discovered to be too dissipative, especially in the low Reynolds number region near the wall surface. It was found by other researchers, such as [Yang and Voke \(2001\)](#) and [Nagabhushanan et al. \(2013\)](#) to predict separated-flow transition incorrectly. Therefore, a more sophisticated dynamic SGS turbulence model, proposed by [Germano et al. \(1991\)](#), with modification from [Lilly \(1991\)](#), is adopted in all simulations in this thesis. This is a one-equation SGS turbulence model based on the Boussinesq eddy viscosity hypothesis. The model constant, C_d , is evaluated locally according to the energy transfer between the subgrid-scale and a newly introduced subtest-scale. The subtest-scale is evaluated from a test filter, $\tilde{\Delta}$, with its size normally taken as twice that of the subgrid-scale filter (Δ), where $\tilde{\Delta}/\Delta = 2$. The model constant can therefore be retained to a minimum when the flow is laminar or in the fully resolved region, where the SGS turbulence model should be completely switched off. Additionally, the model constant in the dynamic SGS turbulence model can be either positive or negative. This means that the energy backscattering, the upscale energy transfer from the small scale to the larger one, is also taken into consideration by

the turbulence model.

In the dynamic SGS turbulence model, the closure applied to the subgrid-scale stress, τ_{ij} , is defined as

$$\tau_{ij} - \frac{1}{3}\tau_{kk}\delta_{ij} = 2C_d\overline{\Delta}^2|\overline{S}|\overline{S}_{ij} \quad (2.13)$$

The closure applied to the subtest-scale (STS) stress, T_{ij} , is defined as:

$$T_{ij} - \frac{1}{3}T_{kk}\delta_{ij} = 2C_d\tilde{\Delta}^2|\tilde{S}|\tilde{S}_{ij} \quad (2.14)$$

The overline, ‘ $\overline{\quad}$ ’, denotes subgrid filter scale, the overhead tilde, ‘ $\tilde{\quad}$ ’, denotes the subtest filter scale. C_d is the dynamic SGS model constant. As proposed by Lilly (1991), the optimal size ratio between the grid filter and the test filter is $\tilde{\Delta}/\Delta = 2$. Therefore, the test filter, $\tilde{\Delta} = 8(d_x d_y d_z)^{1/3}$, is used in the current LES solver.

The resolved stress tensor, L_{ij} , associated with the subtest-scale stress, T_{ij} , and the averaged subgrid-scale stress, $\langle \tau_{ij} \rangle$, can be defined as:

$$L_{ij} = T_{ij} - \langle \tau_{ij} \rangle = -\widetilde{u_i u_j} + \tilde{u}_i \tilde{u}_j \quad (2.15)$$

after subtracting equation 2.13 from equation 2.14

$$L_{ij} - \frac{1}{3}L_{kk}\delta_{ij} = 2C_d M_{ij} \quad (2.16)$$

where

$$M_{ij} = \tilde{\Delta}^2|\tilde{S}|\tilde{S}_{ij} - \overline{\Delta}^2|\overline{S}|\overline{S}_{ij} \quad (2.17)$$

In order to obtain a result with minimum error, the least squares approach is used when solving equation 2.16.

$$q = (L_{ij} - \frac{1}{3}L_{kk}\delta_{ij} - 2C_d M_{ij})^2 \quad (2.18)$$

Upon setting $\partial q/\partial C = 0$, C_d is evaluated as:

$$C_d = \frac{1}{2} \frac{[L_{ij} M_{ij}]}{[M_{ij} M_{ij}]} \quad (2.19)$$

where ‘ $[\]$ ’, denotes the span-wise averaging. In the current LES solver, both the averaging operation and the capping of the model constant, C_d , are implemented in order

to improve the modelling stability.

2.3 Proper Orthogonal Decomposition (POD)

Proper Orthogonal Decomposition (POD) can be used to analyse energy contributions from a complex flow field, in which turbulence motion is represented by a set of deterministic functions; and each of these functions captures a portion of the total kinetic energy. As a result, the most important flow structures can be represented by functions or POD modes that capture the most energetic flow structures. This numerical tool is found to be particularly useful for many transition studies. For example, an insight into energy contributions from the complex transition process is beneficial in finding coherent structures. A few transition studies have employed the POD method to help in understanding the complex flow structures. These include [Simoni et al. \(2017\)](#), [Istvan and Yarusevych \(2018\)](#), and [Hosseinverdi and Fasel \(2018\)](#). Details of these studies are discussed in Section 2.5.2.

The detailed description of the POD method has been provided by [Weiss \(2019\)](#), in which the velocity field, $u'(x, t)$, can be decomposed into a group of deterministic spatial modes, $\Phi_k(x)$, which can be modulated by their transient time-coefficients, $a_k(t)$. Mathematically, this idea is expressed in Eqn. 2.20.

$$u'(x, t) = \sum_{k=1}^{\infty} a_k(t)\Phi_k(x) \quad (2.20)$$

The objective of POD analysis is to find orthonormal modes that contain the most kinetic energy in a turbulent flow field, which may not be straightforward through observation or other analytical approaches. The meaning behind the POD can be further explained with a two-dimensional velocity fluctuation dataset, written in Eqn. 2.21, which is collected from two neighbouring points inside a flow field.

$$U = \begin{pmatrix} u'_a(t_1) & u'_b(t_1) \\ \vdots & \vdots \\ u'_a(t_n) & u'_b(t_n) \end{pmatrix} \quad (2.21)$$

While projecting this raw velocity data onto a graph drawn on the natural basis (x-axis: u'_b and y-axis: u'_a), an elliptic distribution of data points can be observed due to the correlation of the two variables u'_a and u'_b .

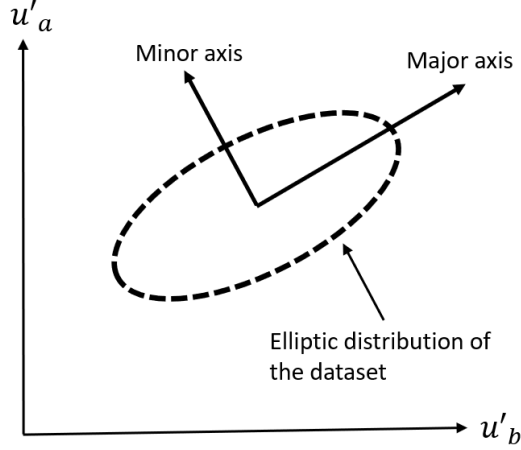


Figure 2.2: Elliptical distribution of a dataset.

As shown in Figure 2.2, the maximum variance can be found on the major axis of the ellipse, and the minimum variance is on the minor axis. As these two axes are orthogonal, their unit vectors correspond to the two proper orthogonal modes of the dataset. These two proper orthogonal modes can be calculated by finding the two corresponding eigenvectors of the covariance matrix, C , as shown in Eqn. 2.22.

$$C = \frac{1}{m-1} \begin{pmatrix} \sum_{i=1}^m u_a'^2(t_i) & \sum_{i=1}^m u_a'(t_i)u_b'(t_i) \\ \sum_{i=1}^m u_b'(t_i)u_a'(t_i) & \sum_{i=1}^m u_b'^2(t_i) \end{pmatrix} \quad (2.22)$$

Ideally, this matrix should be symmetric so that it can be diagonalised to carry out an eigendecomposition. Similarly, in a multi-dimensional case, the data set is distributed as an ellipsoid. Its eigenvectors, or proper orthogonal modes, are axes of the multi-dimensional ellipsoid. Consequently, a distribution of modal kinetic energy can be achieved by ranking the eigenvectors.

2.3.1 The Direct Method POD

There are different methods to compute the POD of a given multi-dimensional data set. The most fundamental approach will be discussed here, known as the Direct Method. However, there is a limitation preventing the application of this method to the large data set of the current LES calculation. This is the excessive requirement of the computational resources. A large matrix, of more than 250 million elements, is needed for the current three-dimensional $u'(x, y, t)$ POD analysis. Such a size requirement is mainly due to the

requirement of a symmetric covariance matrix that will be diagonalised to find eigenvalues and eigenvectors. The purpose of discussing this POD method (Direct Method) is to provide a more straightforward comparison to the optimised method (Snapshot Method) employed in the current LES analysis.

In the calculation using the POD Direct Method, raw data containing $u'(x, y, t)$ information is reordered into a matrix, U_s , as shown in Eqn. 2.23. Typically, this matrix should have a size of $N_r \times N_c$. The total number of columns, N_c , is equal to the mesh size of a two-dimensional plane that will be analysed, $N_x \times N_y$. The total number of rows, N_r , is equal to the total number of time steps of the data set, N_t .

$$U_s = \begin{pmatrix} u'(x_1, y_1, t_1) & \cdots & u'(x_{N_x}, y_{N_y}, t_1) \\ \vdots & \ddots & \vdots \\ u'(x_1, y_1, t_{N_t}) & \cdots & u'(x_{N_x}, y_{N_y}, t_{N_t}) \end{pmatrix} = \begin{pmatrix} u'_{(1,1)} & \cdots & u'_{(N_c,1)} \\ \vdots & \ddots & \vdots \\ u'_{(1,N_r)} & \cdots & u'_{(N_c,N_r)} \end{pmatrix} \quad (2.23)$$

This matrix, U_s , is normally named as the snapshot matrix of the Direct Method. After the snapshot matrix is fully defined, it is input into Eqn. 2.24 to compute the covariance matrix, C , which has dimensions of $N_c \times N_c$.

$$C = \frac{1}{N_c - 1} U_s^T U_s \quad (2.24)$$

In the current LES calculation, xy -plane in the two major mesh blocks covering the completed time-mean separation bubble has a total mesh size of $N_c \approx 15800$ ($N_x \times N_y = 217 \times 73$). This results a covariance matrix that contains approximately 250 million elements which provides a general idea of the extensive requirements of the POD Direct Method. In the next step, the eigenvectors and eigenvalues are computed from the covariance matrix. This yields an eigenvector matrix, Φ , with a size of $N_c \times N_c$, as shown in Eqn. 2.25, and an N_c number of eigenvalues.

$$\Phi = \begin{pmatrix} \phi_{(1,1)} & \cdots & \phi_{(1,N_c)} \\ \vdots & \ddots & \vdots \\ \phi_{(N_c,1)} & \cdots & \phi_{(N_c,N_c)} \end{pmatrix} \quad (2.25)$$

As eigenvectors are the proper orthogonal modes of the data set, the ranking of these eigenvectors will provide a descending order of energy distribution from the proper orthogonal modes, where low-order modes contribute the most energy. The corresponding eigenvalues are also reordered along with the ranking of the eigenvectors. The percentage

of energy contribution from individual mode, i , is defined as $\lambda_i / \sum \lambda_{nk}$, where λ is the eigenvalue. After the ranking of the eigenvalues, the modal energy contribution is also ranked in a descending order. Therefore, the overall energy distribution can be readily visualised by projecting the percentage of modal energy contribution onto a figure. Additionally, in order to visualise different modes of the dataset, a spatial mode matrix with a size of $N_x \times N_y$ is needed to represent the computational grid in the xy -plane. This matrix is normally converted from the eigenvector matrix. The procedure of conversion is the exact reversal of when the original dataset was ordered into the snapshot matrix, U_s . Further details of the reordering procedure can be found in [Weiss \(2019\)](#). The resultant spatial mode matrix contains a total number of N_c modes with a $N_x \times N_y$ matrix under each mode.

To obtain the temporal information from the POD calculation, the eigenvector matrix, Φ , is multiplied by the snapshot matrix, U_s ; the resultant time-coefficient matrix, A , in Eqn. 2.26, has a size of $N_r \times N_c$.

$$A = U\Phi = \begin{pmatrix} \phi_{(1,1)} & \cdots & \phi_{(1,N_c)} \\ \vdots & \ddots & \vdots \\ \phi_{(N_c,1)} & \cdots & \phi_{(N_c,N_c)} \end{pmatrix} \begin{pmatrix} u_{(1,1)} & \cdots & u_{(1,N_c)} \\ \vdots & \ddots & \vdots \\ u_{(N_r,1)} & \cdots & u_{(N_r,N_c)} \end{pmatrix} = \begin{pmatrix} a_{(1,1)} & \cdots & a_{(1,N_c)} \\ \vdots & \ddots & \vdots \\ a_{(N_r,1)} & \cdots & a_{(N_r,N_c)} \end{pmatrix} \quad (2.26)$$

The energy contribution of each mode can be individually evaluated and expressed in a velocity field, \tilde{U}_k , defined by $\tilde{U}_k = A_k \Phi_k^T$. The calculation of \tilde{U}_k of each POD mode (k), is done by multiplying the k th column of the time-coefficient matrix and the transpose of the k th column of the eigenvector matrix, as shown in Eqn. 2.27.

$$\tilde{U}_k = \begin{pmatrix} a_{(1,k)} \\ \vdots \\ a_{(N_r,k)} \end{pmatrix} \begin{pmatrix} \Phi_{(1,k)} & \cdots & \Phi_{(N_c,k)} \end{pmatrix} = \begin{pmatrix} \tilde{u}_{(1,1)}^k & \cdots & \tilde{u}_{(1,N_c)}^k \\ \vdots & \ddots & \vdots \\ \tilde{u}_{(N_r,1)}^k & \cdots & \tilde{u}_{(N_r,N_c)}^k \end{pmatrix} \quad (2.27)$$

Predominantly, the first few POD modes contribute majority of the total kinetic energy, which is enough to help to identify the dominant flow structures. In some applications, only the calculation of a few of the low-order modes of \tilde{U}_k is sufficient to meet the requirement and this can greatly reduce the computational cost while processing the POD results.

2.3.2 The Snapshot Method POD

Typically, a symmetric covariance matrix with a size of $N_c \times N_c$ is required for the eigen-decomposition in the original POD Direct Method. As N_c is the total mesh size of a two-dimensional plane ($N_x \times N_y$) under investigation, a covariance matrix with 250 million elements is needed for the POD Direct Method when used with the current LES dataset. The resource for processing such a large matrix is not readily achievable. Alternatively, the Snapshot POD approach introduced by [Sirovich \(1987\)](#), is employed here. Consequently, an asymmetric covariance matrix with a much lower element count can be used to carry out a POD calculation, making it less demanding in terms of computational resources, and so the Snapshot POD analysis can be applied to datasets from high-fidelity CFD calculations.

The key concept behind the Snapshot Method is that, mathematically, there is no fundamental difference between the spatial modes and the temporal coefficients in the POD calculation. Therefore, the deterministic spatial modes in the Direct Method are replaced by the time-coefficients in the Snapshot Method. This makes POD in the Snapshot Method a decomposition of the temporal coefficients modulated by the spatial modes. In such an approach, the use of a very large covariance matrix can be avoided. Instead, a symmetric correlation matrix with a size of $N_r \times N_r$, is needed, where N_r is the total number of time instances of the dataset, where $N_r = N_t$. This correlation matrix, C_{cor} , is calculated from Eqn. [2.28](#), and the input snapshot matrix, U_s , is identical to the one in the Direct Method, as shown in Eqn. [2.23](#).

$$C_{cor} = \frac{1}{N_r - 1} U_s U_s^T \quad (2.28)$$

The total time instance of the current LES dataset is $N_t = 500$. As a result, the element count of the corresponding correlation matrix, C_{cor} , is 250×10^3 ($N_t \times N_t$) elements. The size reduction here is substantial and the matrix size in the Snapshot Method is more computationally accessible.

In the next step, the eigendecomposition of the correlation matrix is computed. The eigenvectors from the current decomposition correspond to the temporal modes of the dataset, which are identical to the time-coefficients in the Direct Method. The spatial coefficients, Φ_s , can therefore be obtained from the eigenvectors by using Eqn. [2.29](#).

$$\Phi_s = U_s^T A_s \quad (2.29)$$

This equation calculates the spatial coefficients by projecting the transposed snapshot matrix, U_s^T , onto the temporal-mode matrix, A_s . As the spatial coefficients are not from the eigendecomposition, it is orthogonal, whereas the temporal modes are orthonormal. Therefore, a normalisation of the spatial coefficients and a scaling of the temporal modes are required to match the Direct Method results. In the Snapshot Method, the approach of finding the contribution of individual spatial mode is analogous to the Direct Method. The equation is written as Eqn. 2.30 below, in which the modal contribution, \tilde{U}_{sk} , can be computed by the multiplication of the k th column of the time-coefficient matrix, a_s , and the transpose of the k th column of the (normalised) spatial coefficient matrix, Φ_s , where k is the mode number.

$$\tilde{U}_{sk} = \begin{pmatrix} a_s(1, k) \\ \vdots \\ a_s(N_r, k) \end{pmatrix} \begin{pmatrix} \Phi_s(1, k) & \cdots & \Phi_s(N_c, k) \end{pmatrix} = \begin{pmatrix} \tilde{u}_s^k(1, 1) & \cdots & \tilde{u}_s^k(1, N_c) \\ \vdots & \ddots & \vdots \\ \tilde{u}_s^k(N_r, k) & \cdots & \tilde{u}_s^k(N_r, N_c) \end{pmatrix} \quad (2.30)$$

In summary, the Snapshot Method significantly reduces the matrix size in POD analyses and is superior when applied to the current LES dataset with a relatively small number of time steps ($N_t = 500$). This leads to about three orders of magnitude reduction in the matrix size before the eigendecomposition. Conversely, the Direct Method can be quite practical when used on dataset with small mesh sizes and a large number of time instances. Because of the favourable characteristics of the Snapshot Method used in the current dataset, it is employed in all current POD analyses and the results will be discussed in Chapter 6.

2.4 Vortex Identification Methods

In previous studies, multiple vortex identification methods have been successfully utilised to identify vortices caused by streak instabilities. Brandt and de Lange (2008) and Balzer (2011) employed the λ_2 -criterion (Jeong and Hussain (1995)) for identifying streak instability and related transitional structures. This criterion identifies vortex cores by removing the unsteady straining and viscous effects from the pressure minimum criterion. This involves the calculation of eigenvalues of three velocity gradient tensor invariants. In the

current study, a slightly more computationally efficient approach known as the Q-criterion, is used and is defined in Equation 2.31.

$$Q = \frac{1}{2}(\Omega_{ij}\Omega_{ij} - S_{ij}S_{ij}) \quad (2.31)$$

This monitors only the second invariance of the velocity gradient tensor, with a positive value indicating unsteady structures such as a vortex which is formed due to the imbalance between the vorticity field and the rate of strain tensor.

2.5 Boundary Layer Transition

2.5.1 Bypass Transition

As discussed in the previous chapter, the separated-flow transition under elevated FST has similarities with bypass transition. This includes boundary layer receptivity to free-stream turbulence, boundary layer streaks, and streak instability. A review of the up-to-date understanding of these aspects will be provided here.

Boundary Layer Receptivity to Free-Stream Turbulence

In order for streaks to form, the boundary layer has to receive turbulence energy from the freestream. The boundary layer receptivity to free-stream turbulence can be found in two locations on a typical flat plate. The first site is where free-stream turbulence packets impinge on the leading edge of the flat plate, introducing disturbances into the boundary layer through viscous diffusion. Inside the boundary layer, these could cause a significant increase in the stream-wise vorticity (Wundrow and Goldstein (2001)). This process is described by the receptivity theory, which, states that energy from the turbulence packets penetrates the boundary layer through vortex stretching and low-frequency selection. Second, further localised receptivity can be observed at the junction where the elliptic leading edge joins the flat surface. According to Kerschen (1993), such localised receptivity is due to the discontinuity of surface geometry causing a short-scale adjustment to the mean boundary layer flow. In the receptivity process, Saric et al. (2002) reported that the wavelength of the naturally occurring free-stream turbulence was significantly different from those existing inside the boundary layer. As a result, a wavelength-conversion process is required. In order to make such an adjustment, Alfredsson and Matsubara (2000)

have observed that the boundary layer amplifies low-frequency contents while damping high-frequency ones. This conclusion was drawn by comparing velocity time traces inside and outside the boundary layer. [Jacobs and Durbin \(2001\)](#) described such a conversion process as the shear sheltering phenomenon. The shear layer acts as a low-pass filter to frequencies from the free-stream disturbances, with only low-frequency contents penetrating the boundary. The high-frequency content remains in the freestream, causing lifted low-speed streaks ([Zaki and Durbin \(2005\)](#)). This shear sheltering process has been further demonstrated theoretically by [Zaki \(2011\)](#). They point out that the penetration of free-stream disturbances into the boundary layer is dependent on the ratio of wall-normal diffusion and on the shear force.

Boundary Layer Streaks

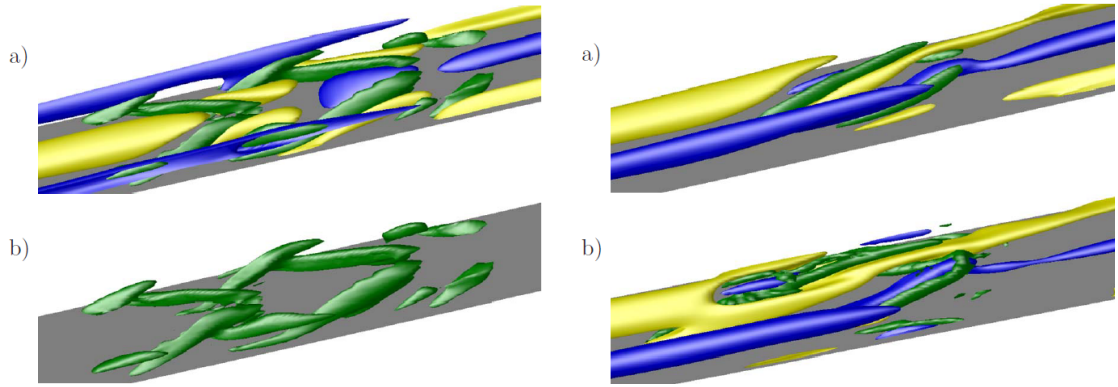
Due to boundary layer receptivity to the free-stream turbulence, large amplitude span-wise modulations are reported inside the laminar boundary layer ([Dryden \(1936\)](#)). These are elongated streak structures which are formed, and which propagate, inside the boundary layer. They were widely recognised after the works by [Klebanoff et al. \(1961b\)](#) and [Klebanoff \(1971\)](#). A widely used terminology was later established after the work by [Kendall \(1985\)](#) and these are now known as Klebanoff streaks. Characteristically, these boundary layer streaks are dominated by a stream-wise velocity fluctuations component ([Taylor \(1939\)](#)). The Klebanoff streaks can cause thinning and thickening of the boundary layer and hence play an important role in turbulent spot inception via the secondary instability stage. Both primary and secondary instability stages of bypass transition are caused by development of the boundary layer streaks. A secondary instability analysis, using linearly optimal streaks, has been performed by [Andersson et al. \(2001\)](#). They reported that streaks needed to reach a very high amplitude (26%) of the free-stream velocity in order to develop into the first unstable mode. The transition process caused by the boundary layer streaks is reported to have been initiated not only near the edge of the boundary layer but also near the wall surface ([Nagarajan et al. \(2007\)](#)). This indicates that more than one streak-instability mode exists in the transition process.

Streak Secondary Instability

The two secondary instability modes in bypass transition are found to be comparable to the two secondary instabilities from the Görtler flow by [Swearingen and Blackwelder \(1987\)](#). These are known as varicose and sinuous instabilities, which are defined according to the symmetry of the streaks interaction. Respectively, they are caused by the span-wise symmetric and antisymmetric streak interactions in bypass transition. [Brandt and de Lange \(2008\)](#) have demonstrated the differences between these two breakdown modes by using idealised streaks and minimal background disturbances in a DNS simulation. The varicose mode is found to be caused by a head-on collision of two different momentum streaks. The resultant instability wave is amplified when the surface shear is promoted by a high-momentum streak going over a low-momentum one, whereas, in the sinuous mode, this is a result of a partial overlap collision of two different momentum streaks, in which the high-momentum streak is bent sideways to form an instability with a sinuous pattern. Different breakdown vortices are also caused by these two instability breakdowns. The varicose mode is found to cause a series of alternating Λ -vortices pointing in an opposite direction, which have been termed Λ and V structures, as shown in [Figure 2.3a](#). In the later stage, only the Λ -vortex is amplified. In the breakdown of the sinuous mode, two vortices are identified, corresponding to the two different momentum streaks as shown in [Figure 2.3b](#). A Λ -vortex is formed after a low-speed streak, and an elongated vortex is formed after the high-speed streaks.

In numerical work by [Vaughan and Zaki \(2011\)](#), two secondary instability modes have been predicted by the linear stability analysis. These are known as inner and outer mode streak instability. The outer mode is found to be caused by increased shear between a lifted low-speed streak and the high-speed free-stream fluid. In this mode, the critical layer is found to be located near the boundary layer edge. The inner mode streak instability arises due to the increased shear between a high-speed streak and low-speed fluid below. The critical layer of this mode is close to the plate surface and a phase speed is about half of the free-stream velocity. [Hack \(2014\)](#) reported that, when under an adverse pressure gradient, the near wall inflection point was caused by an interaction of a high-speed and a low-speed streak. [Vaughan and Zaki \(2011\)](#) reported that the inner mode had a span-wise wavelength which was identical to the streak span-wise wavelength. This is a result of the varicose symmetric instability. For the outer mode, it is found to be the subharmonic of

the base streak span-wise wavelength, and the varicose and sinuous instabilities coexist.



(a) Varicose breakdown vortex, (Brandt and Lange, 2008).

(b) Sinuous breakdown vortex (Brandt and Lange, 2008).

Figure 2.3: Gold: High-speed streaks, Blue: Low-speed streaks, Green: Breakdown vortices.

2.5.2 Separated-flow Transition

Under Minimal FST

Some pioneer research works have been carried out on separated-flow transition, such as the LES study conducted by [Yang and Voke \(2000\)](#). This study can be considered as a high-resolution LES study that important flow regions have resolution close to DNS. The separated-flow transition process was induced by a semi-circular flat plate leading edge with almost no background disturbances. There is clear evidence of boundary layer separation and it is inviscidly unstable to disturbance, indicating that the dominant transition mechanism is indeed the well-known K-H instability. Frequency space was also examined with a range of vortex shedding frequencies that are within the unstable region of the K-H instability criterion. The K-H associated vortex shedding activity was also reported and the vortex shedding Strouhal number was found to be 0.005-0.0011. A similar conclusion was drawn by an experimental study of separated-flow transition on a flat plate surface under 0.5%-FST ([Dähnert \(2013\)](#)). This transition process on a flat plate was induced by applied adverse pressure gradient. The K-H instability was found to dominate in the transition process and the vortex shedding Strouhal number satisfies the correlation suggested by [Yang and Voke \(2001\)](#). The shear layer instability frequency was also detected, which consists of a frequency from inviscid K-H instability.

K-H instability as the dominant transition mechanism in separated-flow transition has also been reported by [Spalart and Strelets \(2000\)](#). This DNS study was conducted on a flat plate with transition process induced by local adverse pressure gradient. They noticed the wavering behaviour of the separated shear layer before the formation of K-H instability. After transition onset, K-H related vortices were observed rapidly developed into three-dimensional flow structures without the vortex pairing stage. Such secondary instability stage would normally occur after the primary K-H instability in planar shear layer transition. This observation is supported by LES studies from [Abadalla and Yang \(2004\)](#) and [Abadalla and Yang \(2005\)](#).

K-H instability as the dominant instability mechanism for separated-flow transition in minimal FST conditions is also supported by other studies, such as [Burgmann et al. \(2008\)](#), [Abdalla et al. \(2009\)](#), [Satta et al. \(2010\)](#), [Dähnert et al. \(2012\)](#), [Yang \(2013\)](#), and [Serna and Lazaro \(2015\)](#). K-H instability also shares similarities to planar shear layer transition, as reported by [\(Ho and Huerre \(1984\), Rogers and Moser \(1993\), Danaila et al. \(1997\), and Urbin and Metais \(1997\)\)](#).

Under Elevated FST

In a typical separated-flow transition, the elevated FST can lead to a different transition scenario than that under minimal FST. [Langari and Yang \(2013\)](#) compared a geometry-induced separated-flow transition under both low- and high-FST levels of 0.2% and 5.6%. In the low-FST case, two-dimensional span-wise K-H rollers are clearly identified and turbulent breakdown was found to start with the bending of the third span-wise K-H roller. In the high-FST case, neither the cross-span K-H rollers, nor the K-H correlated frequency, can be identified from the transition process. This implies that the K-H related span-wise shear layer roll-up has been bypassed in the transition process under elevated FST conditions.

A similar transition mechanism was also identified in separated-flow transition on a flat-plate surface by [McAuliffe and Yaras \(2010\)](#). Their DNS study compared the transition process under FST levels of 0.1% and 1.45%. In their high-FST study, no K-H related span-wise rollers can be identified. Instead, boundary layer unsteadiness, known as Klebanoff streaks, was found to be propagating near the laminar boundary layer surface prior to separation. The formation mechanism of these boundary layer streaks is comparable to

that in bypass transition, which also occurs via the shear sheltering mechanism. These streaks further extended into the separated shear layer and eventually disappeared in the transitional flow. The shear layer breakdown is believed to be caused by the streak secondary instability being identical to the bypass transition. Nevertheless, no varicose or sinuous instability was observed prior to the breakdown process. The secondary instability also possesses a frequency peak identical to that of the K-H frequency. This indicates that the exact transition mechanism of the separated-flow transition under elevated FST remains a mystery, which will be investigated in the current work.

The separation bubble size is found to reduce as the FST level increases (Hillier and Cherry (1981) and Castro and Haque (1988)). In Yang and Abdalla (2005), there is a 14% reduction in the bubble size when the FST level is increased to 2%. Earlier breakdown and a different secondary instability stage can also be observed with 2% FST. Volino (2002a) and Volino (2002b) reported that the transition process moved upstream as the Reynolds number and the FST level were increased. Noticeably, the level of FST has direct influence on the size of the separation bubble. However, the actual mechanism remains unclear.

The differences between the transition process in the minimal-FST and the elevated-FST case can be significant. This is mainly due to Klebanoff streaks formed upstream of the transition location, which play an important role in the transition process (Li and Yang (2016)). Meanwhile, the K-H instability is still at work. This is supported by the fact that a K-H frequency was detected by McAuliffe and Yaras (2010) and by Yang and Abdalla (2005) in their LES work on separated-flow transition, respectively under 1.45% FST and 2% FST. Also, boundary layer streaks and part-span K-H rollers were reported by Coull and Hodson (2011) in their experimental work on the flat plate transition process with 3.0% FST. In this experimental work, boundary layer separation is induced by adverse pressure gradient from a high-lift low-pressure turbine blade. Aligned with the experimental work, similar boundary layer streaks and part-span K-H structures have also been predicted numerically using LES by Nagabhushanan et al. (2013) in their work on the flat-plate transition process. Observations from these studies imply the coexistence of the K-H instability and the streak-related instabilities in the transition process under elevated FST. Balzer and Fasel (2016) later confirmed this speculation in their DNS investigation of separated-flow transition. In their work, boundary layer streaks were found even in their lowest-FST case (0.05%), as well as, in their highest-FST case (2.5%). In the

latter case, strong magnitude streaks were observed to connect with the turbulent flow structures without eliminating the separation bubble. This provides explicit evidence of the coexistence of boundary layer streaks and K-H instability. Transition onset is triggered by the combination of these instability mechanisms.

In recent experimental work on an NACA 0018 airfoil, by [Istvan and Yarusevych \(2018\)](#), the separated-flow transition under a variety of FST levels (0.06%, 0.32%, 0.51%, and 1.99%) was investigated using high-speed two-component PIV measurements. The vortex shedding is clearly observable in both the low- and high-FST cases, indicating that the K-H instability is still present. The boundary layer streaks are also found to play an important role in the transition process. Using POD analysis, streaks are found to contribute more towards the total kinetic energy than part-span rollers from the K-H instability. Consequently, the streak instabilities are considered to have dominated in this case.

Experimental work by [Simoni et al. \(2017\)](#) investigated the separated-flow transition under 0.65%, 1.2%, and 2.87% FST with different Reynolds numbers ($Re = 40000, 75000, 90000$). In two lower Reynolds number cases, a separation bubble is still present in all three levels of FST. In contrast, no boundary layer separation was detected in the highest Reynolds number case with 2.78% FST, in which the separation bubble had been eliminated. This finding has been reinforced by their POD analysis which shows that no vortex shedding related energy was detected in the case with 2.87% FST and $Re = 90000$. This study characterised the separation bubble dynamics and statistical properties under different FST levels and Reynolds numbers. The reduction in separation bubble length and height in higher FST levels (fixed Reynolds number) is due to strong boundary layer streaks penetrating the separation bubble. Otherwise, no other characteristic of boundary layer streak is provided.

In a recent DNS study by [Hosseini-verdi and Fasel \(2018\)](#), their simulation mimics a water-tunnel experiment, with boundary layer separation achieved by placing an inverted airfoil (modified NACA 643-618 profile) in close proximity to the flat plate. In the numerical simulation, the airfoil is replaced by an equivalent wall-normal velocity profile which is placed on the free-stream boundary of the computational domain. The resolution of this numerical simulation can be classified as highly resolved DNS, in which Δx^+ , Δy^+ (at $y = 9$), and Δz^+ are respectively 1.58, 0.44, and 2.7, and 25 control vol-

umes within the region of $y^+ < 9$. The total number of control volumes is 88.85×10^6 ($N_x \times N_y \times N_z = 1815 \times 240 \times 200$). In total, six levels of FST were investigated in this study ($Tu = 0.0\%$, 0.1% , 0.5% , 1.0% , 2.0% , and 3%). In cases with 0.0% - 0.1% FST, inviscid K-H instability is the dominant mechanism in causing transition, whereas in cases with 0.5% - 1.0% FST, both K-H instability and streak instability, blended together, cause the transition onset. Finally, in cases with 2.0% - 3.0% FST, streak instability is most energetic and considered to be the dominant mechanism causing transition onset. However, a separation bubble still exists. Part-span K-H waves are much weaker compared to lower FST cases, and were not captured by lower modes of their POD analysis.

2.6 Overview and Objectives of the Present Research

The primary aim of the current research is to provide further understanding of the boundary layer separated-flow transition under elevated FST. Due to the increased FST level, boundary layer streaks are formed and propagate inside the boundary layer. The transition process herein is considered much more complex than that without influence of FST. The complexity is caused by the coexistence of multiple instability mechanisms in a higher-FST environment. In contrast, only K-H instability is found in the transition process when FST is approaching zero, which has been confirmed by both experimental and numerical investigations. When under elevated FST, even as small as 0.51% , multiple instability mechanisms, a combination of streak instability and K-H instability, were reported. The dominant instability mechanisms in the transition process also depend on the FST level. K-H instability is found to dominate in a low-FST environment, such as between 0.0% to 0.5% . In cases with higher FST levels, such as between 0.5% to 2.0% , these two instability mechanisms equally dominated in the transition process. When the FST level reached 2.8% , [Simoni et al. \(2017\)](#) reported neither a separation bubble nor K-H instability existing in the transition process on an airfoil profile. Streak instability dominates; and the transition process can be considered as bypass transition. In the most recent work by [Hosseinvardi and Fasel \(2018\)](#), they have concluded that, up to 3.0% FST, streak instability is the most energetic mechanism leading to transition onset, with separation bubble and much weaker K-H instability still existing. The relevant literature on this subject is very scarce and discrepancy is found in two of the most recent studies. The current understanding is far from established. Additionally, in both these studies with

higher FST levels, the adverse pressure gradient provided by the employed geometry can be considered as different to those from a turbine blade. Therefore, the current study will investigate separated-flow transition from a geometry that closely represents a turbine blade profile. Second, studies of separated-flow transition under even higher levels of FST are rather rare and this aspect will be investigated. Most importantly, the dynamics of the transition process due to multiple instability mechanisms (streak instability and K-H instability) has not been reported previously. Therefore, the current study is aimed at providing further understanding of this aspect of the transition process. The breakdown of tasks for each section of this thesis is outlined below:

Part-1

- a. To confirm the existence of K-H instability in the 3% FST case. If the K-H instability does not exist, what is the actual transition mechanism?
- b. To confirm the existence of the K-H related secondary instability. If this is bypassed, what will be the bypass mechanism?
- c. To confirm the existence of Klebanoff streaks; also to verify if these boundary layer streaks can lead to any turbulence spot inception or the onset of bypass transition.

Part-2

- a. To investigate the effect of elevated FST and to examine the difference in the transition process under even higher levels of FST.

Part-3

- a. To examine the coexistence of both K-H instability and streak instabilities; also to identify the dominant transition mechanism should both exist.
- b. To confirm the transition mechanism of the separated-flow transition with boundary layer streaks. Will it be caused by the two streak instability modes normally found in the bypass transition?

Part-4

- a. To understand the streak instability modes in the current separated-flow transition. What are the instability mechanisms linked to these streak instabilities?

Chapter 3

Numerical Details

3.1 The DELTA Solver

The numerical calculations in the current study were performed using a finite volume in-house LES solver: DELTA. This CFD solver is written in the combination of C and FORTRAN programming languages. The unsteady Navier-Stokes equations were solved on a curvilinear structured mesh, which has been divided into multiple blocks for parallelisation. The collocated mesh arrangement was employed with all the flow variables and pressure stored at an identical location. This can greatly reduce the solver complexity and enhance its efficiency. However, the well-known ‘checkerboard’ effect is anticipated. An improved Rhie-Chow interpolation (Yi et al. (2016)) was adopted to suppress the pressure-velocity decoupling, which is believed to be the root cause of the “checkerboard” effect. This interpolation method will be further discussed in Section 3.1.2.

In the DELTA solver, the SIMPLE (Semi Implicit Method for Pressure Linked Equations) algorithm is used to relate the discrete face velocities from the continuity equations to the discrete pressure field in the momentum equations. This yields a velocity field that satisfies both the continuity and the momentum equations. The SIMPLE algorithm is implemented in the inner iteration process of DELTA. The detailed procedures will be discussed in the forthcoming Section 3.1.1. The QUICK (Quadratic Upwind Interpolation for Convective Kinematics) scheme was used for the discretisation of the convective terms in both the continuity and the momentum equations, whereas the diffusive terms in the momentum equations were discretised by the second-order central difference scheme. Furthermore, the temporal discretisation is achieved by an implicit single-stage backwards

Euler scheme which was found to be more stable for the current unsteady calculation. More details of this CFD code can be found in [Pokora et al. \(2011\)](#).

The DELTA solver has been validated in a variety of flow scenarios, such as external or internal, compressible or incompressible and free or wall-bounded flows ([Page \(2005\)](#); [Page et al. \(2002\)](#); [Pokora et al. \(2011\)](#); [Langari \(2013\)](#)). Most importantly, the DELTA solver has been successfully used in the boundary layer separated-flow transition studies by [Langari \(2013\)](#) and [Langari and Yang \(2013\)](#). This boundary layer transition is comparable to the separated-flow transition in the current investigation.

3.1.1 Solution Procedures - SIMPLE Algorithm

In the DELTA solver, the solution procedure at each time step is summarised as follows. This provides a brief description of how the SIMPLE algorithm is implemented in the DELTA solver.

1. In each time step, viscosity is frozen over all iterations; therefore, the turbulence viscosity, μ_t , is predicted before the start of any inner iteration. This prediction uses the so-called dynamic SGS turbulence model with velocity fields from the previous time step. More details about this model can be found in Section 2.2. After updating all the necessary variables, such as velocity, pressure, and viscosity vectors, the inner iteration begins.

2. At the beginning of each inner iteration, the initial face velocity is extrapolated from the velocities of adjacent nodes. Meanwhile, the boundary conditions are configured, using inputs from the boundary-condition files, and variables of the boundary planes are then stored in the corresponding locations of the variable matrix.

3. In the next steps, the discretised momentum equations are solved. When solving these equations, the coefficient matrix is first constructed and then the Line Gauss-Seidel solver is used to find the resultant velocity field. This velocity field is known as the intermediate velocity field due to a guessed pressure field being used for its prediction.

4. The discretised energy equation is then solved by the Line Gauss-Seidel solver before the continuity equations.

5. When solving the continuity equations, the improved Rhie-Chow interpolation ([Yi et al. \(2016\)](#)) is applied to the cell face velocities to suppress any pressure-velocity decoupling. The coefficient matrix for the continuity equation is then constructed, and

is solved by the Line Gauss-Seidel solver. This yields uncorrected mass fluxes at the control-volume faces.

6. The pressure correction equation is then solved and produces a pressure correction term for the correction of the face mass fluxes, face pressure, and cell-centre pressure, whereas the cell-centre velocities are corrected using the face pressure. The inner iteration is completed once all corrections have been completed.

7. The inner iteration repeats until reaching the preset numbers of inner iterations, or the preset convergence criterion before starting a new time step.

3.1.2 Improved Rhie-Chow Interpolation

The well-known disadvantage of the collocated mesh arrangement is the odd-even decoupling (“checkerboard”) effect. This is caused by storing pressure value at the cell-centre location. When calculating the face-centre velocity, only pressure values from alternative cell-centres are used. As a result, the calculated advective velocity has a very high tendency to oscillate. The Rhie-Chow interpolation (Rhie and Chow (1983)) is widely adopted to alleviate such undesirable numerical effects.

The original Rhie-Chow formulation is written below. These formulae are written on a cell, P , and its neighbour cell, E , with an intermediate cell face, e . The discretised momentum equation can be expressed as Eqn. 3.1 and Eqn. 3.1, where a_P is the diagonal coefficient of the linear equation and u_P^n/dt is the explicit part of the time derivative term, $\partial u_P/\partial t$; H_P , consisting of implicit off-diagonal terms, other explicit terms, and source terms of the momentum equations.

$$a_P u_P^{n+1} = H_P - (\nabla p)_P + \frac{u_P^n}{dt} \quad (3.1)$$

$$a_E u_E^{n+1} = H_E - (\nabla p)_E + \frac{u_E^n}{dt} \quad (3.2)$$

When considering a 1D case with a uniform mesh, $a_e = a_P = a_E$, and $(\nabla p)_e = (p_E - p_P)/dx$, the face-centre velocity can be calculated by combining Eqn. 3.1 and Eqn. 3.2, which yields:

$$a_e u_e^{n+1} = (H_E + H_P)/2 - (\nabla p)_e + \frac{(u_P^n + u_E^n)}{2dt} \quad (3.3)$$

with ∇P replaced by $\partial p/\partial x$:

$$u_e^{n+1} = \frac{1}{2}(u_P^{n+1} + u_E^{n+1}) - \frac{1}{a_e} \left[\left(\frac{\partial P}{\partial x} \right)_e - \frac{1}{2} \left(\frac{\partial p}{\partial x} \right)_P - \frac{1}{2} \left(\frac{p}{\partial x} \right)_E \right] \quad (3.4)$$

where

$$\left(\frac{\partial P}{\partial x} \right)_e - \frac{1}{2} \left(\frac{\partial p}{\partial x} \right)_P - \frac{1}{2} \left(\frac{p}{\partial x} \right)_E = -\frac{dx^2}{8} \left(\frac{\partial^3 p}{\partial x^3} \right)_e \quad (3.5)$$

When the viscosity term is discretised explicitly, $a_e = \rho/dt$, which yields:

$$u_e^{n+1} = \frac{1}{2}(u_P^{n+1} + u_E^{n+1}) + \frac{dx^2}{8} \frac{dt}{\rho} \left(\frac{\partial^3 p}{\partial x^3} \right)_e \quad (3.6)$$

Apparently, with a small time-step size, such as in the order of 10^{-4} , the dP term can vanish. This clearly indicates that the effectiveness of the original Rhie-Chow interpolation is heavily dependent on the time-step size. The smoothing function can be greatly reduced when the time-step size is small, and the pressure-velocity decoupling effect remains. [Yi et al. \(2016\)](#) propose an improved Rhie-Chow interpolation to minimise its dependency on the time-step size, which can be described as:

$$u_e^{n+1} = \frac{1}{2}(u_P^{n+1} + u_E^{n+1}) - \frac{1}{a_e} \left[\left(\frac{\partial P}{\partial x} \right)_e - \frac{1}{2} \left(\frac{\partial p}{\partial x} \right)_P - \frac{1}{2} \left(\frac{p}{\partial x} \right)_E \right] + \frac{u_e^n}{dt} - \frac{(u_P^n + u_E^n)}{2dt} \quad (3.7)$$

since

$$\frac{u_e^n}{dt} - \frac{(u_P^n + u_E^n)}{2dt} = -\frac{dx^2}{8dt} \left(\frac{\partial^2 u}{\partial x^2} \right)_e \quad (3.8)$$

As shown in Eqn. 3.8, a second derivative term calculated from velocities of the previous time step is added to the original interpolation.

$$u_e^{n+1} = \frac{1}{2}(u_P^{n+1} + u_E^{n+1}) + \frac{dx^2}{8} \frac{dt}{\rho} \left(\frac{\partial^3 p}{\partial x^3} \right)_e + \frac{dx^2}{8dt} \left(\frac{\partial^2 u}{\partial x^2} \right)_e \quad (3.9)$$

This term becomes significant when the time-step size is small, which offsets the decreasing dP term. Therefore, the smoothing function provided by the Rhie-Chow interpolation can remain effective. This term has been added to Rhie-Chow interpolation equations in the DELTA solver to enhance the suppression of the pressure-velocity decoupling effect in current simulations.

3.1.3 Free-stream Turbulence Generation

A realistic inlet turbulence is essential for both the LES approach and the boundary layer flow transition prediction. LES is a time-dependent calculation that requires turbulence information to be input into the computational domain at every time step. Traditional RANS inlet turbulence generation methods are unfit for this purpose. Therefore, different kinds of inlet turbulence generation methods are presented for the LES approach. These are broadly classified into three methods: the spectral method, the synthetic fluctuations method, and the synthetic eddy method. Additionally, the inlet turbulence structure also plays a critical role in the boundary layer transition prediction. The characteristics of the inlet free-stream turbulence can greatly influence the onset location and transition lengths, such as free-stream turbulence intensity.

In order to maintain a balance between generating realistic inlet turbulence, computational cost, and coding difficulty, a synthetic fluctuation approach is chosen in the current flat plate study. A numerical tripping method, used in [Langari and Yang \(2013\)](#) and [Pokora et al. \(2011\)](#), was employed here to generate a desirable level of inlet free-stream turbulence. In this approach, turbulent perturbation, u' , is first added to the mean velocity profile from the inlet plane. An additional perturbation, u'_b , is then applied to an immersed plane inside the inlet channel. This plane has an orientation that is identical to the inlet plane and normally it is configured a few cells distance downstream.

At each time step, random velocity perturbation, u'_{ijk} , with zero mean and unit variance distribution, are added to the instantaneous velocity field, U_{ijk} , of a stencil around a given control volume of the immersed plane. This procedure is implemented to the velocity field in all three directions and can be represented by the following equations. An example of a stencil in the stream-wise direction is demonstrated in [Figure 3.1](#) below.

$$\begin{aligned}
 u_{ijk} &= u_{ijk} + u' \\
 u_{i\pm 1,j,k} &= u_{i\pm 1,j,k} + 0.5u' \\
 u_{i,j\pm 1,k} &= u_{i,j\pm 1,k} + 0.5u' \\
 u_{i,j,k\pm 1} &= u_{i,j,k\pm 1} + 0.5u' \\
 u_{i\pm 2,j,k} &= u_{i\pm 2,j,k} + 0.25u' \\
 u_{i,j\pm 2,k} &= u_{i,j\pm 2,k} + 0.25u' \\
 u_{i,j,k\pm 2} &= u_{i,j,k\pm 2} + 0.25u'
 \end{aligned}$$

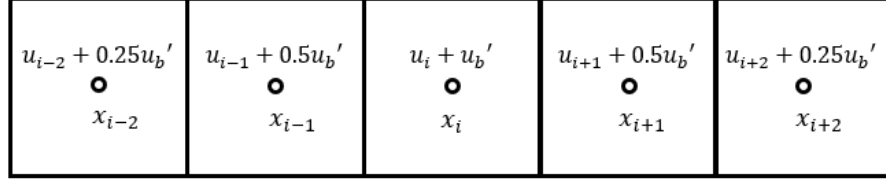


Figure 3.1: An example of stream-wise stencil around a cell, x_i , in the immersed plane.

Considering the synthetic nature of the current approach, a longer inlet channel is also configured to allow appropriate development of the synthetic turbulence. After the initial dampening of uncorrelated high-frequency contents, realistic turbulence is sustained and yields 3.0% turbulence intensity near the flat plate leading edge. The current turbulence intensity closely matches the experimental study by [Coull and Hodson \(2011\)](#). Additionally, the free-stream turbulence spectrum near the flat plate leading edge is demonstrated in Figure 3.2, of which no distinct frequency peak exists in the free-stream energy spectrum. This indicates that the generated free-stream turbulence does not contain any undesirable frequency content.

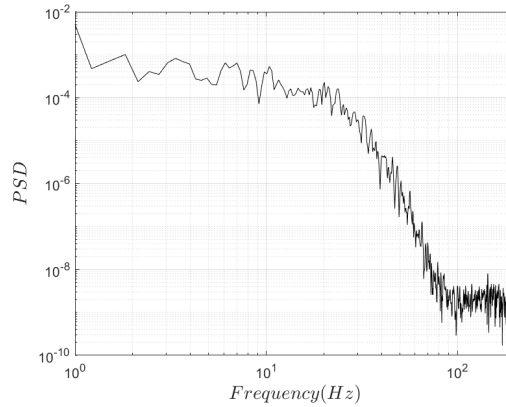


Figure 3.2: Free-stream turbulence spectrum near the flat plate leading edge.

3.1.4 Convective Outflow Boundary Condition

Similar to the inlet turbulence generation method, the outflow boundary condition from the RANS approach is unfit for LES applications. The traditional zero-gradient velocity outflow boundary condition, developed for RANS calculation, is described below in Eqn. 3.10.

$$\frac{\partial u}{\partial x} = 0 \quad (3.10)$$

This zero-gradient outflow boundary condition is not designed for the LES unsteady calculation, as it can cause velocity stiffness at the outlet boundary. As a result of having constant velocity at this location, the pressure fluctuations are reflected back into the computational domain, causing a non-physical flow phenomenon inside the flow domain. A solution to alleviate this problem is to use the convective outflow boundary condition shown in Eqn. 3.11 below.

$$\frac{\partial u}{\partial t} + U_m \frac{\partial u}{\partial x} = 0 \quad (3.11)$$

In this approach, the mean velocity, U_m , is first calculated by the mass flux of an upstream location and then the velocity gradient between the upstream location and the outlet plane is solved by the backward-difference scheme. Subsequently, the discretised Eqn. 3.12 can be used to compute the outflow velocity at the next time step.

$$u^{n+1} = (-\Delta t)U_m\left(\frac{u_i - u_{i-1}}{\Delta x}\right) + u_i^n \quad (3.12)$$

In this equation, the superscript, n , denotes the current time step, and $n + 1$ denotes the next time step.

3.2 DELTA Solver Improvements

In the DELTA solver, there are a few important features and modifications that are essential for the current boundary layer transition investigation. These features and modifications were added to the solver by the author during this study. One of the improvements is the implementation of the improved Rhie-Chow interpolation and the convective outflow boundary condition, respectively discussed in Sections 3.1.2 and 3.1.4. Other improvements and modifications, such as improving the dynamic SGS turbulence model, and additional data exportation methods for post-processing, are discussed below.

In the original version of DELTA, the dynamic SGS turbulence model subroutine was written in an ad-hoc manner, with many sections of the code written for a specific simulation. These sections were later modified by the author, so that they can be used in different geometries and simulations. Also, in the main subroutine, an identical section of code to apply wall treatment for the dynamic SGS turbulence model has been repeatedly used on numerous occasions. This makes the code particularly difficult to read and it only

works for a specific geometry and simulation. These were modified and moved into new subroutines. As discussed previously in Section 2.2, an additional test filtering operation is required by the dynamic SGS turbulence model. The original filtering operation was applied to a plane with constant stream-wise location. This has been modified to apply to a plane with a constant wall-normal location, which has been suggested by [Sylvain et al. \(2012\)](#). This modification allows the filtering operation to take into consideration flow variations in the stream-wise direction. The same modification has also been applied to the test filtering operations in the calculation of M_{ij} (Eqn. 2.17), which is needed in the calculation of the $|\widetilde{S}|_{ij}$ term on the right-hand-side of the equation.

The DELTA solver achieves parallelisation by the so-called blocking approach. This requires the geometry to be divided into blocks before being input into the solver. However, there was a limit (error) in the original DELTA solver, in that it can only solve mesh that is divided into no more than 30 blocks. This also implies that only 30 processor cores can be used in the parallel calculation. This number is considered very small for the current LES calculation, or for a typical LES calculation. The author has increased this limitation by resolving some geometry-linkage and memory-allocation issues.

During the post-processing stage of the DELTA solver, ASCII data is normally written as an output file for visualisation via a post-processing package, TECPLOT. It has a native binary file format (a file with .plt suffix) that offers great IO (input or output) performance and smaller file size over the traditional ASCII format. Therefore, the DELTA data output subroutine has been modified to export the TECPLOT binary format file as an additional feature. This modification has significantly optimised the post-processing workflow between the DELTA solver and TECPLOT. When exporting data from the current simulation, there is about an 88% reduction in time and a 77% reduction in file size. Remarkably, such improvement makes exporting three-dimensional time-series data from an LES calculation computationally viable. Therefore, another feature of exporting time-series data in TECPLOT binary format has been added to the DELTA solver. In order to achieve this, velocity and pressure field data needed to be transferred efficiently to the master processor from the worker processors. This has been done via the Message Passing Interface (MPI) framework. This communication process is configured to happen at the end of each time step. The master processor then gathers data from all worker processors and exports it to a file. Although the TECPLOT binary data format offers

excellent IO performance and a much more compact file size, nevertheless, to export time-series data of the complete computational domain from the current simulations at every time step is not yet possible. This is due to the limitation in computational resources. As a result, time-series data of blocks above the upper flat plate surface were exported at every 20 time steps. The resultant TECPLOT binary data size is approximately 40GB. After the calculation of the required variables, such as fluctuation velocities, vorticities, etc., the file size can increase to 146GB for the region near the upper flat plate surface. This time-series data is used for the POD and three-dimensional flow visualisation.

Other post-processing features, such as exporting mid-plane data and exporting sampling point time-series data, are also implemented in the DELTA solver, with none included in the original version. The relatively small size of the mid-plane data was used to provide preliminary results, and to monitor convergence history and other aspects during the simulation. Moreover, the time-series data of an array of approximately 560 sampling points were exported at every time step. This data set was used for the power spectral density calculations and other unsteady analysis.

3.3 Computational Resources

The governing Navier-Stokes equations were solved using the classical domain-decomposition approach, with the computational domain divided into multiple blocks and the calculation of each block assigned to one processor core. A high-efficiency message passing interface (MPI) is used to handle the communications among worker processors, as well as between worker processors and the master processor. Such an arrangement requires a number of processor cores identical to the number of blocks, plus one extra core for the master processor. Because of the limited computational resources, only 32 processor cores were available in the early stages of this study and great effort has been put into achieving a good balance between the resolution and the length of the simulation. Later, the author has constructed a small cluster consisting of one master node, one storage node, and six computing nodes. Each computing node has two sockets which consist of two Intel Xeon E5 V4 processors. The communications within a single computing node are via the OpenMP (Open Multi-Processing) framework, whereas the communications between the computing nodes and the storage node are achieved via the RDMA (Remote Direct Memory Access) protocol over an FDR Infiniband network interconnect, which offers a

low latency data transfer rate of up to 56Gbit/s. This cluster increased the available computational resources to 144 processor cores, which allows the computational domain to be decomposed into 55 blocks with 8.67×10^6 control volumes. With this improved blocking topology, the computational mesh can be divided more evenly across all blocks, significantly improving the load balance among all worker processors. The simulation time for one case is about three months, which has been increased although not dramatically so due to the mesh size increasing from 5.1×10^6 to 8.67×10^6 control volumes. The increased storage space and IO performance via the Infiniband interconnect, also makes exporting TECPLOT time-series three-dimensional data possible within an acceptable time frame.

3.4 Implementation of POD method

As discussed in Section 2.3, the POD Snapshot Method is employed here to analyse the current transition process. As three-dimensional TECPLOT time-series data being already extracted from the flow field during the simulation, implementation of the POD method becomes a rather straight forward task. First, two-dimensional data is extracted from the three-dimensional flow field, and is stored as unstructured data at every time step. The data set is then interpolated into a structured format, in which the discretised form of POD formulae can be used for the calculation of POD modes. One of the disadvantages of this approach is that the spectral resolution is limited to half the sampling frequency of the three-dimensional data due to the Nyquist limit. Nevertheless, the current spectral resolution is about 250Hz and is considered sufficient for the current transition analysis.

Chapter 4

Separated-flow Transition on Flat Plate

4.1 Introduction

Separated-flow transition on an elliptical leading edge flat plate and under 3% FST is investigated here. Boundary layer separation is induced by adverse pressure gradient, imposed by two contour walls respectively mounting opposite to both plate surfaces. The contour wall geometry employed here generates pressure distribution that is considered more representative of those from a low-pressure turbine blade suction-side surface. The objective of this study is to complement and advance current understanding on the separated-flow transition process. To date, no definite answer remains as to what the transition mechanism is when separated-flow transition is under elevated FST. This is due to a such transition process being extremely sensitive to surrounding flow conditions and the formation of propagating boundary layer streaks. Is K-H instability still the dominant instability mechanism? Is K-H instability bypassed in the current case with 3.0% FST (measured at the flat plate LE)? What role do these streaks play in the transition process, and how do they interact with K-H instability? The current study addresses these questions numerically, using the LES approach.

Contents, discussions, and conclusions provided in this chapter (Chapter 4) were published in a journal article: Hua J. Li and Z. Yang, 2019, Separated boundary layer transition under pressure gradient in the presence of free-stream turbulence, *Physics of Fluids*, 31(10), 104106(2019).

4.2 Simulation Configuration and Overview

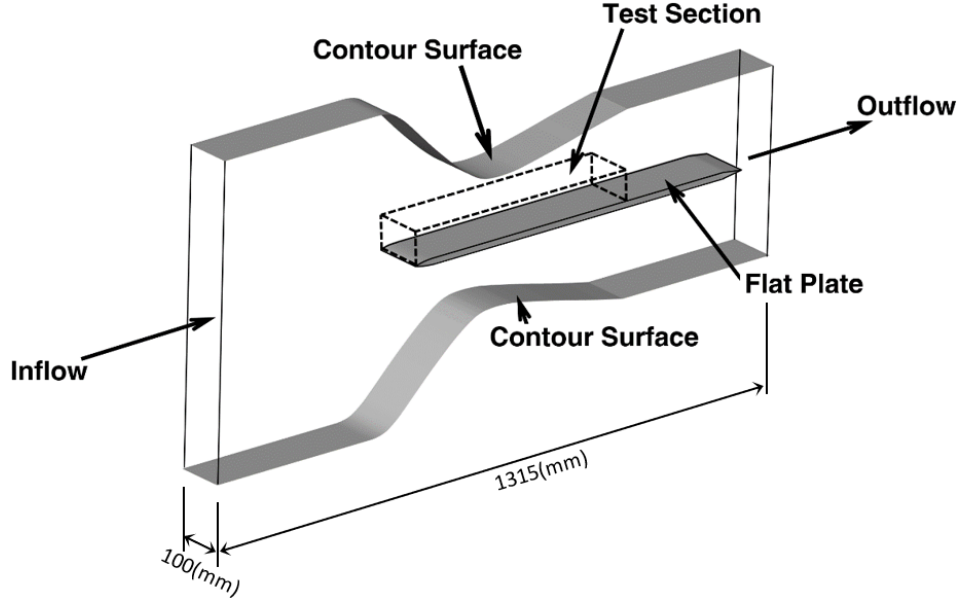


Figure 4.1: Schematic of the computational domain.

The geometry for investigating the boundary layer flow transition is shown in Figure 4.1. This geometry is originally used in the experimental study by [Coull and Hodson \(2011\)](#), where the current computational domain is the working section of their wind tunnel. The geometry consists of an elliptic leading edge flat plate with a thickness of $d = 12.8(mm)$ locating at the mid-height of the computational domain. Two identical contour surfaces (top and bottom) are employed to impose pressure distribution on both plate surfaces. This pressure distribution is taken from the T106 low-pressure turbine blade suction surface, allowing similar separated-flow transition to be studied on a flat plate surface. There are several advantages in using this geometry to study the separated-flow transition. Studying the linear boundary layer on a flat plate surface is more straight forward than on the curved surface of a turbine blade. The flow field variation due to the surface curvature change can be neglected and hence the complexity and cost of the numerical investigation can be greatly reduced. Additionally, the existing experimental data can be used to validate the prediction from the current LES calculation.

As shown in Figure 4.1, the computational domain has a total stream-wise length of 1315(mm) and a width of 100(mm). The span-wise width has been chosen to match the experimental value. It is slightly larger than three times the inlet turbulence length

scale. The width used here is also more than the value used in the studies by [Yang and Voke \(2001\)](#) and [Langari and Yang \(2013\)](#). They considered twice the plate thickness to be sufficient for separated-flow transition induced by a curvature change at the flat plate leading edge, and there are no significant changes in the transition process when doubling up this number. Additionally, in the study of pressure-induced separated boundary layer transition by [McAuliffe and Yaras \(2008\)](#), their computational domain width is about twice the transition wavelength at the reattachment location. In the current study, the investigation of pressure-induced transition is very similar to that of the one from McAuliffe and Yaras. However, a slightly larger computational domain width is used. The current width of $100(mm)$ is approximately four times the averaged Λ -vortex width at the turbulence breakdown location, which is an important three-dimensional coherent structure found inside the boundary layer. The width is considered sufficient to account for any span-wise inhomogeneous flow structures. Furthermore, the boundary layer transition in the mid-span region should be unaffected by any unrealistic flow structure resulting from using a less realistic boundary condition on the side boundaries.

Virtually all important flow features related to boundary layer transition can be found inside the rectangle box named “Test Section” in [Figure 4.1](#). The length of the “Test Section” is $S_0 = 500(mm)$. This S_0 value will be used to normalise all length in the current flat plate study, an approach identical to the experimental work. A uniform velocity distribution, $U_{in} = 1.34(m/s)$, is applied at the inlet plane. This yields a time-mean stream-wise velocity, $U_{out} = 2.5(m/s)$, at the test section nominal exit at $x/S_0 = 1.0$. The Reynolds number, based on the nominal exit velocity and test section length is, $Re_{S_0} = 84000$, defined as:

$$Re_{S_0} = \frac{U_{out}S_0}{\nu} \quad (4.1)$$

Below the flat plate, the lower passage is included in the simulation which provides a correct instantaneous mass flow variation similar to the experimental case. Due to the instantaneous shrinking and expanding of the separation bubble, the amount of mass flow passing through the upper and the lower passage varies temporally. This effect would be completely neglected if only half of the computational domain (only the upper passage) was modelled and the boundary layer, as well as the predicted velocity field could deviate from the experiment.

Figure 4.2A shows the computational mesh that contains approximate 5.1×10^6 control volumes created using the ICEM-CFD multi-blocking approach. This computational mesh has been divided into outer and inner regions in order to achieve a good resolution mesh for important flow features. This approach can also avoid having excessive dense mesh in less important regions of the computational domain. In the outer region with black mesh lines, the computational mesh has covered most of the free-stream flow. The number of mesh points in x, y, z directions are $N_x, N_y, N_z = 428, 130, 50$, whereas for the inner region with red mesh lines, the computational mesh has covered the flat plate boundary layer. Therefore, C-grid is used for better refinement within the boundary layer. In total, 72 exponentially distributed mesh points are configured along the wall normal direction. A detailed view of mesh around the flat plate leading edge (highlighted by blue edges) is shown in Figure 4.2B.

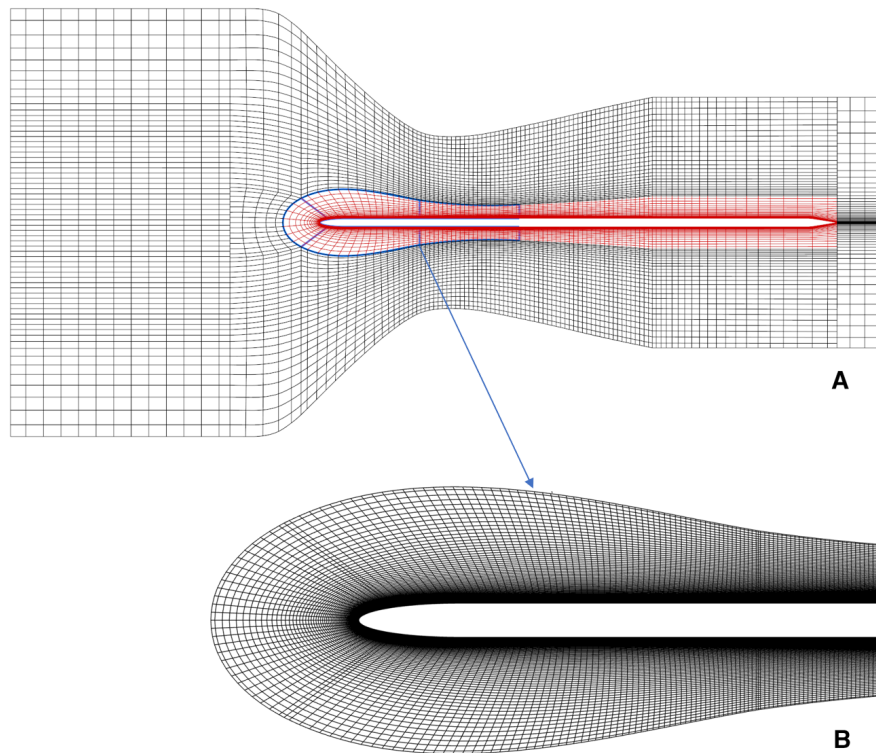


Figure 4.2: A: An overview of the computational mesh with mesh points omitted for better visualisation. Regions coloured in red and the exit domain: every 4th point in x and y is shown. The remaining region: every 4th point and every 2nd point in x and y are shown respectively. B: Detailed view of the computational mesh (all points shown) around the flat plate leading edge that is highlighted by blue edges in A.

Based on the friction velocity measured in the fully developed turbulence region at

$x/S_0 \approx 1.2$, the minimum non-dimensional wall distance inside the “Test Section” is $\Delta y^+ = 0.84$, the minimum non-dimensional stream-wise distance is $\Delta x^+ = 13.89$ and the minimum non-dimensional span-wise distance is $\Delta z^+ = 16.8$. The time step size of 1.0×10^{-4} seconds is used to ensure that the maximum CFL number is below 0.3. The initial calculation is allowed to run for 20 flow-through periods to achieve numerical convergence and a fully established flow field. This condition is defined using both the residuals from the governing equations and from the separation bubble characteristics. The former is considered as a reference, whereas the latter is what really defines the fully established condition of the current transition simulation. As shown in Figure 4.3, the bubble length, l_{bubble} , calculated from the difference between the separation and the reattachment location, has no significant change after the 20th flow-through. The collection of data for the time-average calculation started at this point and was gathered for a further 20 flow-through periods with samples taken at every time step. Time-dependent data of sampling points is also collected at every time step for frequency domain analyses and at every 20 time steps for three-dimensional flow visualisation and POD analysis. A summary of the most significant simulation parameters can be found in Table 4.1

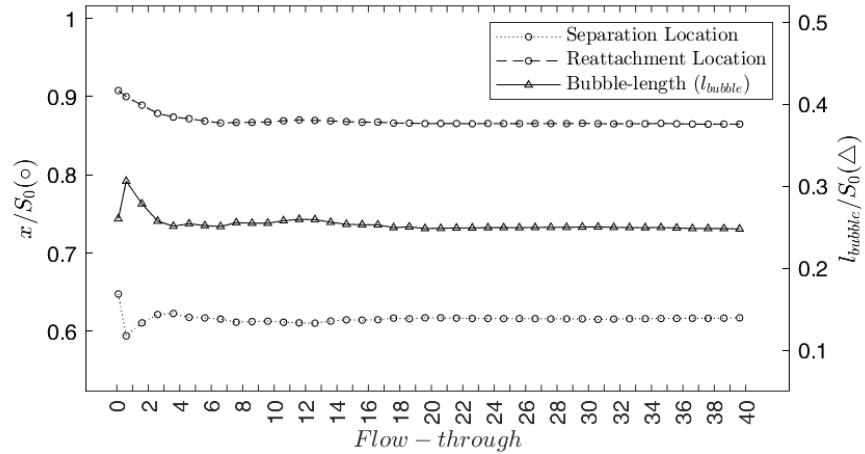


Figure 4.3: The temporal change of separation bubble characteristics. Left y-axis: Scales for the separation and reattachment locations with symbol (\circ). Right y-axis: Scales for the bubble length, l_{bubble} , with symbol (Δ).

Plate thickness	d	12.8(mm)
Test section length	S_0	500(mm)
Plate span	l_{span}	100(mm)
Inflow velocity	U_{in}	1.34(m/s)
Test-Section nominal exit velocity	U_{out}	2.5(m/s)
Reynolds number	Re_{S_0}	84000
Turbulence intensity near leading edge	T_u	3.0%
Total mesh size		5.1×10^6
Δy^+		< 1
Time-step size		$1.0 \times 10^{-4}(s)$
CFL number		< 0.3

Table 4.1: Flow configuration and numerical details.

4.3 Computational Mesh Analysis

In a typical LES simulation with implicit filtering, the computational mesh functions as a low-pass filter separating the turbulent flow into different scales. The filter cut-off point, defined by the control-volume size, normally lies in the Inertial Scale region (Figure 2.1) smaller than the Integral Scale (largest scale), but larger than the Kolmogorov Scale (smallest scale). Consequently, the time-dependent solutions of the governing equations can change after the refinement of the computational mesh or the change of the filter cut-off point. The unique solution can only be obtained when the computational mesh is sufficient to resolve all the turbulence length-scale. This includes the Kolmogorov Scale which has the lowest energy contribution generated from the molecular diffusion and heat dissipation. Such simulation is known as Direct Numerical Simulation (DNS), which has not been widely utilised due to its excessive computational requirements.

Although a mesh-independent study normally conducted in RANS simulation does not provide a tangible conclusion about LES mesh quality, it is still conducted here to check if there is any significant change after the refinement of the computational mesh. Solutions from two computational meshes with a different number of control volumes and blocking topologies are compared. One mesh has 5.1×10^6 control volumes, and the other mesh has 8.76×10^6 control volumes. The computational requirements and timeframe to solve

the latter case has reached the maximum available computational capacity for the current study and, therefore no further refinement has been done. Details of these two cases are summarised in the table below.

Case	Control volumes ($\times 10^6$)	N_{blocks}	N_z	Aspect Ratio ($l_{x_{min}} : l_{y_{min}} : l_z$)	Size ratio
Mesh-5M ^b	5.10	30	51	13.9 : 1 : 16.8	1.00
Mesh-8M	8.76	55	71	12.3 : 1 : 14.3	1.93*

Table 4.2: Details of two cases under investigation, (“ b ” : the base-line case; “ * ” : this value is calculated based on the three-dimensional mesh sizes around the separation bubble).

Apart from the size difference, the blocking topology is also different in these two cases. The base-line case, Mesh-5M, has a total of 30 blocks, and four blocks are above the upper plate surface. The second case, Mesh-8M, has a total of 55 blocks, and seven blocks above the upper plate surface. In the base-line case, only a block with $(N_x \times N_y \times N_z) = (122 \times 72 \times 51)$ encloses the entire separation bubble (the transition region). In contrast, three blocks are used to cover the same region with a size of $(N_{x_{total}} \times N_y \times N_z) = ((50+74+41) \times 72 \times 51)$ in the second case. The resultant size ratio is 1.93 in this region. As shown in Table 4.2, the aspect ratio for the smallest control volume above the plate surface, denoted by, $l_{x_{min}} : l_{y_{min}} : l_z$, remains different in the two cases. In the case of Mesh-8M, the most significant refinement is in the region covering the boundary layer and especially in regions around the separation bubble.

Figure 4.4 shows the comparison of the velocity profiles between the two cases under investigation. Overall, a minor effect from the refinement can be identified in the transition region between $x/S_0 = 0.6$ and $x/S_0 = 0.85$. In this region, the velocity profiles from the two simulations have relatively small discrepancies and are nearly identical in the near wall region below $y/S_0 < 0.5$. In the boundary layer breakdown and fully turbulent region between $x/S_0 = 0.9$ to $x/S_0 = 1.1$, identifiable improvements can be found in the near wall region below $y/S_0 = 0.010$. Overall, only limited amount of improvements can be found after adding an extra 3×10^6 control volumes or approximately 170% increase in mesh size. This aligns with the hypothesis that a limited amount of turbulence flow is further resolved by the refined mesh; nevertheless, the effect of the refinement is considered as

rather insignificant in terms of the current study. This is due to these downstream locations with most improvements being further apart from the transition region.

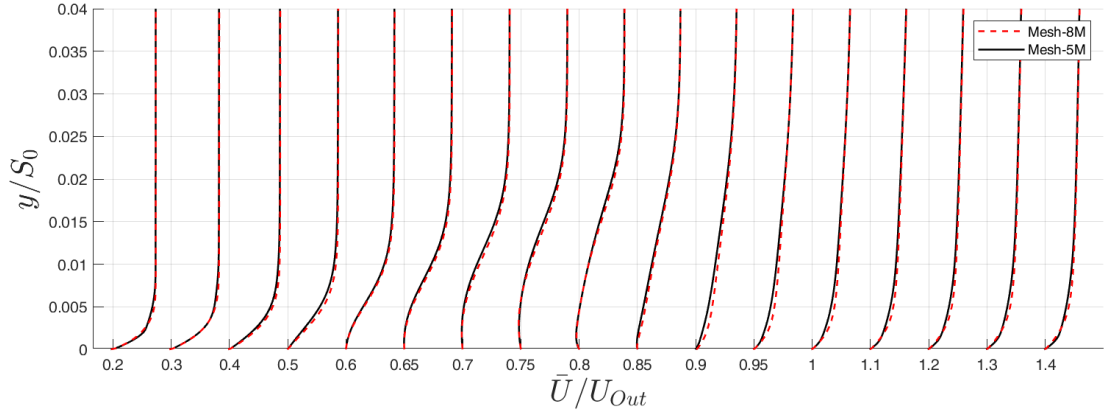


Figure 4.4: Comparison of velocity profiles between the two cases.

A similar observation can also be made from the velocity distribution plot shown in Figure 4.5. Minor differences can be identified after $x/S_0 = 0.85$, but otherwise results from the two cases remain almost identical in other locations. This indicates that the refinement has a minor impact on the flow field near the boundary layer edge. Similar to the previously discussed velocity profile plot, the largest discrepancy can be found at $x/S_0 = 0.90$. This location is considered less significant in the context of the current study.

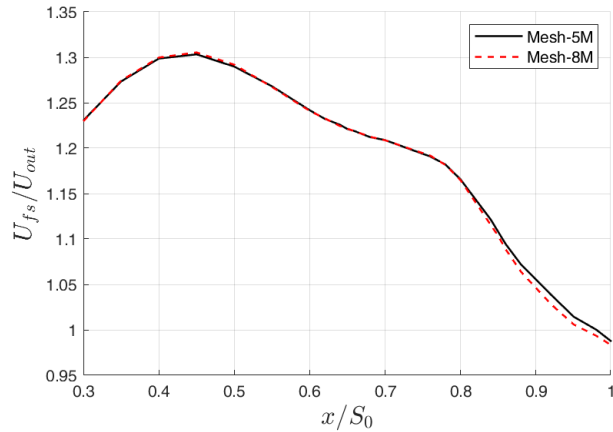


Figure 4.5: Comparison of velocity distribution between the two cases.

In terms of the separation and reattachment locations, the predictions from both cases are comparable. The separation and reattachment locations for the base-line case, Mesh-5M, are $x/S_0 = 0.616$ and $x/S_0 = 0.866$, respectively. The two locations predicted in

the refined case, Mesh-8M, are $x/S_0 = 0.618$ and $x/S_0 = 0.860$, respectively. Again, a trivial difference can be found, and this is mainly due to the aspect ratio change of the first control volume above the plate surface. In the near wall low Reynolds number region, such as inside the separation bubble, the boundary layer flow is considered non-turbulent. The dynamic SGS turbulence model is designed to switch off in this region. Therefore, the unrefined mesh size is considered sufficient in this near wall region.

After investigating both cases in the flow field near the boundary layer edge from the velocity distribution plot (Figure 4.5), inside the boundary from the velocity profile plots (Figure 4.4), and the separation and reattachment locations on the plate surface, only minor discrepancies can be identified after the mesh refinement. These differences are mainly found in the boundary layer break-up and the fully turbulence region at $x/S_0 = 0.09$ and downstream, whereas in the transition region, results from both cases are almost identical. Considering the computational cost of running the simulation and post processing, in addition to the improvement in accuracy, the smaller mesh (Mesh-5M) is selected to be used in the forthcoming investigations in Chapter 4 with 0.0% and 3.0% FST. The refined mesh (Mesh-8M) is used in cases with 4.7% and 8.0% FST in Chapter 5.

4.4 Flow Characteristics

4.4.1 Mean Flow Characteristics

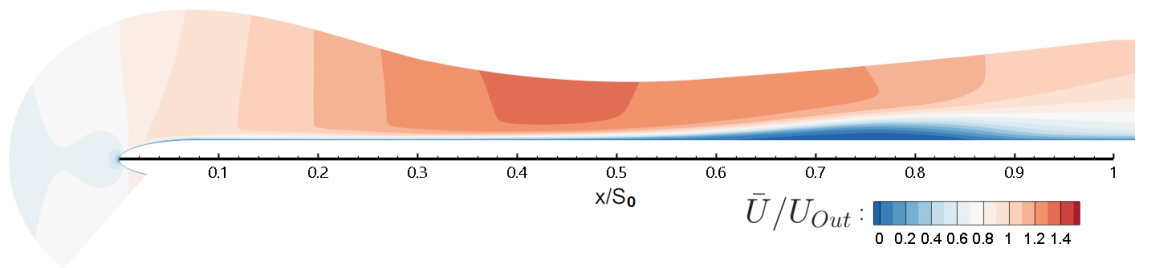


Figure 4.6: Time-mean u -velocity contour of the computational domain at mid-plane (only the mesh blocks next to the plate surface are shown). For the purposes of providing a clear illustration, the wall-normal dimension has been scaled to 1.5 times the stream-wise dimension.

Figure 4.6 shows an overview of the time-mean stream-wise velocity contour near the flat plate leading edge and upper surface. The flow field shown in Figure 4.6 contains

the most important flow structures inside the upper passage of the computation domain. This includes the upper surface boundary layer, which is the primary focus of the current investigation. In terms of the lower surface boundary layer, its temporal averaged characteristics are identical to those of the upper one and will not be investigated in detail.

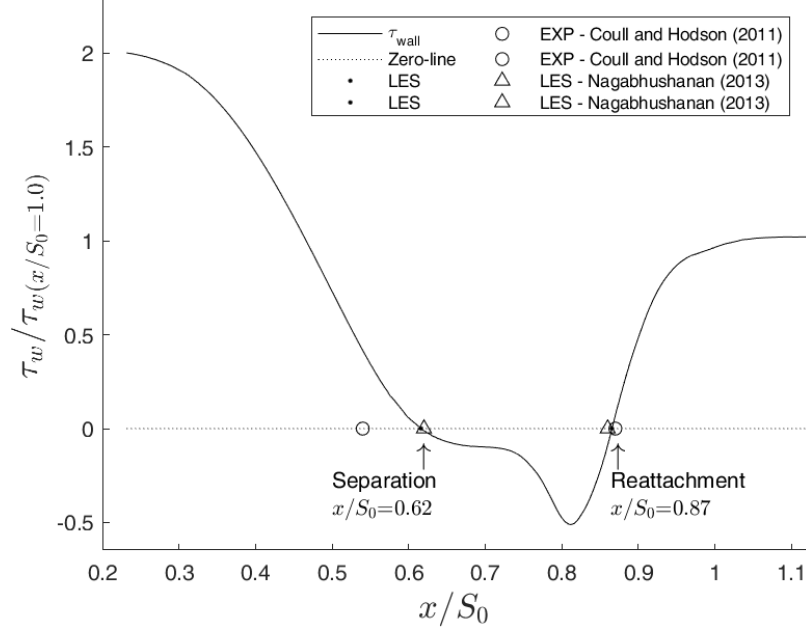


Figure 4.7: Solid line: Time-mean stream-wise wall shear stress from the current LES calculation. Symbols: Separation and reattachment locations. Current LES: (‘ · ’), Experiment data: [Coull and Hodson \(2011\)](#) (‘ ◦ ’), LES data: [Nagabhushanan et al. \(2013\)](#) (‘ Δ ’).

The boundary layer of a separated-flow transition separates from the surface after the minimum pressure location at $x/S_0 = 0.398$. The corresponding wall shear stress, τ_w , reaches zero at the separation location. The wall shear stress then becomes negative in the following region with laminar separated shear layer and reversed flow. Finally, the time-mean boundary layer reattaches to the surface, and the wall shear stress returns to zero. Therefore, two locations with zero wall shear stress corresponded respectively to the separation and reattachment locations. As shown in Figure 4.7, these two locations associate to two points on the wall shear stress curve crossing the zero dash line. In the current study, the predicted time-mean separation and reattachment locations are at $x/S_0 \approx 0.62$ and $x/S_0 \approx 0.87$. These two locations were measured in the experimental study by [Coull and Hodson \(2011\)](#) as $x/S_0 = 0.54$ and $x/S_0 = 0.85$, respectively. Their

measurement was based on the surface-mounted hot film sensors and oil-and-dye flow visualisation. In the previous LES study by Nagabhushanan et al. (2013) using their in-house solver, these two locations were predicted as $x/S_0 = 0.62$ and $x/S_0 = 0.86$.

Figure 4.8 shows the time-mean velocity profiles at 10 stream-wise locations between $x/S_0 = 0.50$ and $x/S_0 = 1.00$. These results from the current simulation closely agree with the experimental PIV data from Coull and Hodson (2011) particularly onward of the reattachment location at $x/S_0 = 0.85$. The major discrepancy can be found at $x/S_0 = 0.80$ near the boundary layer edge and at the reverse flow region. Nevertheless, the differences are within 3% of deviation. It is also possible to observe similar discrepancies from the previous LES results from Nagabhushanan et al. (2013).

Another major discrepancy was found at $x/S_0 = 0.50$, with the predicted velocity near the boundary layer surface deviating from the experimental observation. The same discrepancy can also be found when observing the LES study by Nagabhushanan et al. (2013). Both LES studies have predicted a later separation point, as shown in Figure 4.7. However, the cause of this discrepancy is unclear and requires further investigation.

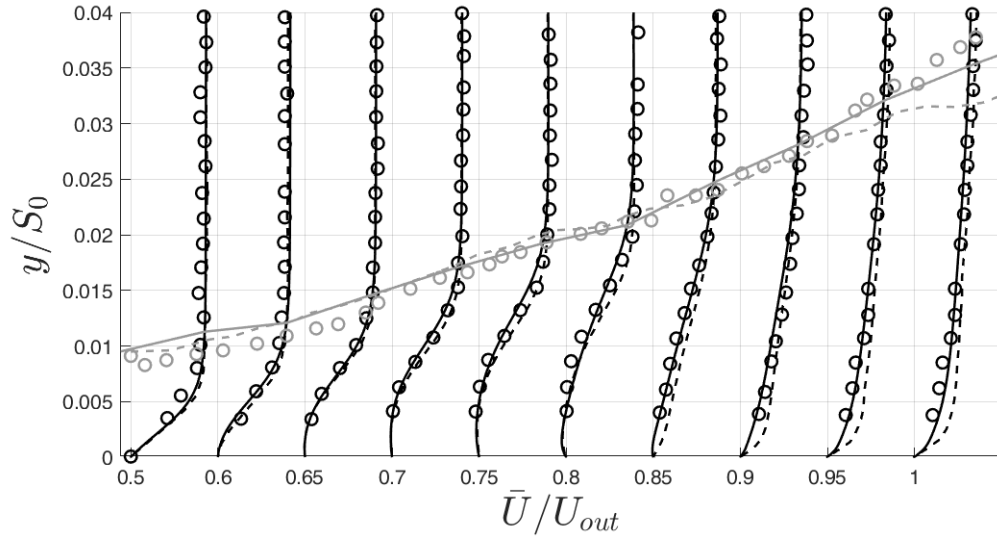


Figure 4.8: Black colour: Time-mean velocity profiles at $x/S_0 = 0.50, 0.60, 0.65, 0.70, 0.75, 0.80, 0.85, 0.90, 0.95, 1.00$. Gray colour: Boundary layer thickness at δ_{95} . Symbols: Current LES: (' - '), Experiment data (Coull and Hodson (2011)): (' o '), LES data (Nagabhushanan et al. (2013)): (' - - ').

At $x/S_0 = 0.86$, this location is where the boundary layer break-up is initiated and occasionally multiple shear layers and vortical structures can be observed. The μ_t value

also increases dramatically at this location, with the possibility of μ_t/μ rising suddenly to an order of magnitude larger. This indicates that the SGS model begins to function intensively at this location. A finer mesh was used to alleviate the input from the SGS model without successfully improving the situation. The cause of the deviation remains unclear at this stage.

In Figure 4.8, the boundary layer thickness, δ_{95} , can be studied from the grey lines indicating the wall-normal locations with 95% of the free-stream velocity. The solid line representing the current LES result matches the general trend of the experimental data shown by symbols. The small differences are caused by the known limitation in the evaluation of the boundary layer edge velocity with a non-uniform free-stream velocity. The change in local pressure gradient can lead to the variation of the free-stream velocity along the wall-normal direction, which makes the evaluation of δ_{95} more difficult. Also, in order to maintain an affordable computational mesh, the use of less dense mesh near the less important opposite contour wall has been a conventional approach achieving this goal. This can increase the uncertainty of the predicted free-stream velocity, which is reflected in the deviation of boundary layer thickness parameters.

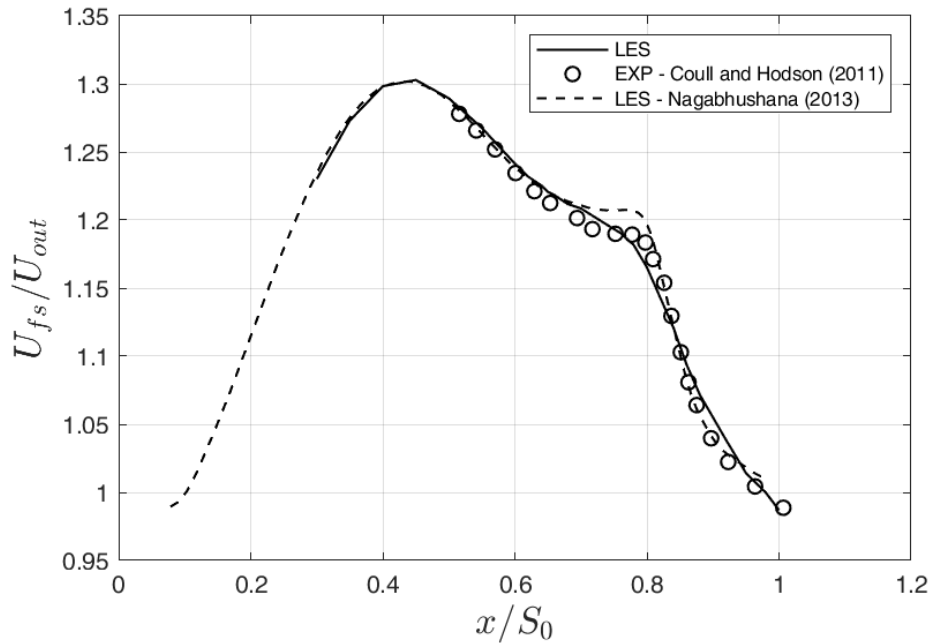


Figure 4.9: Free-stream velocity distribution along the flat plate surface. Symbols: Current LES: (‘ - ’), Experiment data (Coull and Hodson (2011)): (‘ o ’), LES data (Nagabhushanan et al. (2013)): (‘ - - ’).

Despite the already known limitations, the error from the boundary layer thickness calculation itself can be significant. In order to calculate the δ_{95} rigorously, the approach taken by Coull and Hodson (2011) is adopted here. This approach has been further improved in both the calculations of boundary layer thickness and edge velocity, which is discussed below in details. After the calculation using the improved approach, the small discrepancy of δ_{95} between the current LES prediction and the experimental observation is trivial. Overall, the current prediction of the time-mean boundary layer thickness, δ_{95} , is accurate and reliable.

The normalised free-stream velocity distribution (U_{fs}/U_{out}) along the upper plate surface is compared in Figure 4.9. When calculating the free-stream velocity of each velocity profile, the free-stream section tends to vary in the wall-normal direction due to local pressure variations. This makes the evaluation of a correct free-stream velocity, U_{fs} , very challenging. The approach from Coull and Hodson (2011) is adopted here with an improvement to evaluate U_{fs} . In their approach, a linear regression analysis was used to find the straight line that best fits the free-stream part of the velocity profile. The first intersection between the straight line and the velocity profile is taken as δ_{100} , as well as U_{fs} . The line of best fit and its first intersection with the velocity profile is discovered here to depend mostly on the selected free-stream section of a velocity profile, which has a major impact on the outcome. Therefore, an iterative process is implemented to identify the correct free-stream section. In each iteration, the velocity ratio of the velocity, U_{99}^n , at the first point of the current selected free-stream section (same as δ_{99}) to the velocity, $U_{100}^{(n+1)}$, at a newly generated intersection ($\delta_{100}^{(n+1)}$) is checked, which should satisfy the relationship of $U_{99}^n = 0.99U_{100}^{(n+1)}$. If this is not the case, a new iteration is executed with an adjusted free-stream section starting with a new $\delta_{99}^{(n+1)}$ that is calculated using $0.99 \times \delta_{100}^{(n+1)}$. A new line of best fit and the first intersection location are again calculated. The iterative process continues until the velocity ratio is satisfied and the velocity at the corresponding free-stream location (δ_{100}) is used as U_{fs} . As clearly shown by the normalised U_{fs} in Figure 4.9, a good agreement has been obtained between results from the current LES study and the experimental investigation, especially in the region just before and after $x/S_0 = 0.8$.

Overall, the comparisons between the current time-mean flow field, the experimental data, and the previous LES result indicate that, despite the small discrepancy found at the

aft portion of the separation bubble, the current LES prediction is considered accurate and reliable. Highly favourable agreements can be found in these comparisons between the current prediction and the experimental observation, whereas the small discrepancies in these comparisons are believed to be caused by the limitation from the SGS model in predicting the current complex transitional activities. DNS could be employed to settle the modelling limitation and to provide further understanding of the current highly complex transitional boundary layer. However, such an approach is too expensive to be considered at this stage.

4.4.2 T-S Instability

Figure 4.10 shows vertically displaced power spectral density (PSD) plots along the stream-wise direction. 10 sampling points are placed inside both the attached boundary layer and the separated laminar shear layer respectively before and after the minimum pressure location ($x/S_0 = 0.396$). A distinct frequency peak of approximately 150Hz exists in the PSD of several stream-wise locations. This frequency peak can be detected from the flat plate leading edge up to a downstream location at $x/S_0 = 0.18$. Thereafter, no distinct frequency peak is detected through the time-mean separation location ($x/S_0 = 0.62$) until the last measurement point ($x/S_0 = 0.65$) inside the separated laminar shear layer. The occurrence of such frequency peaks may suggest that viscous instability is happening near the flat plate leading edge, possibly through the T-S routine. In order to confirm this speculation, leading edge boundary layer parameters at $x/S_0 = 0.12$ are input into the correlation from Walker (1989) in Equ. 4.2. This yields the T-S wave maximum amplification frequency to be 125Hz. In Figure 4.10, the frequency peaks (150Hz) between $x/S_0 = 0.10$ and $x/S_0 = 0.18$ are found to have a slightly higher content than that predicted by Walker's correlation ($f_{TS(unstable)} = 125\text{Hz}$). Nevertheless, Walker's approach is an empirical correlation that only detects the T-S wave receiving maximum amplification. According to the linear stability theory, slightly higher frequency waves receiving moderate amplification can also become unstable. Consequently, the detected frequency peak is considered comparable. A viscous T-S instability is considered at the current flat plate leading edge upstream of $x/S_0 = 0.18$.

$$f_{TS(unstable)} = \frac{3.2u^2}{2\pi\nu Re_{\delta^*}^{3/2}} \quad (4.2)$$

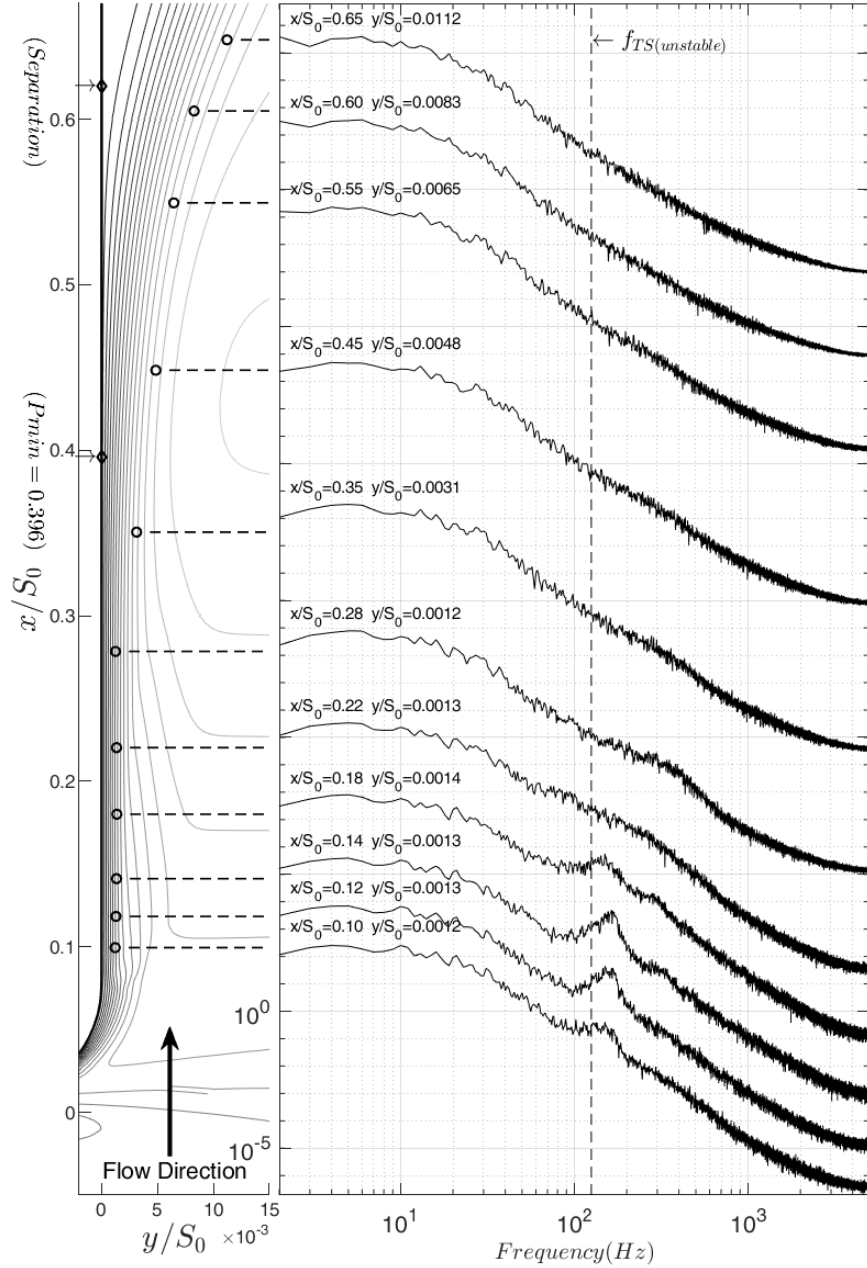


Figure 4.10: Left: Flat plate (placed vertically) and PSD sampling points ('o') within the boundary layer showing by u -velocity line contour. Right: Displaced frequency spectra of u' -velocity at stream-wise locations between $x/S_0 = 0.10$ and $x/S_0 = 0.65$. Dash line: the T-S wave maximum amplification frequency, $f_{TS(unstable)} = 125\text{Hz}$, predicted by the correlation from Equ. 4.2. In the vertical scale of the displaced frequency spectra plot, one increment between two major ticks is 1.0×10^5 .

In Figure 4.10, these frequency peaks disappear at the downstream boundary layer between $x/S_0 = 0.28$ and $x/S_0 = 0.65$. This region is under the favourable pressure gradient, along with the strongest free-stream acceleration, and the boundary layer may

have undergone the so-called reverse flow transition or “relaminarization”. Therefore, any boundary layer instability wave can be suppressed under such free-stream conditions. In order to quantify the magnitude of the current free-stream acceleration near the leading edge, the free-stream acceleration parameter, $K = v/u^2(du/dx)$, is evaluated at a location immediately before any detectable frequency peak. According to [Mayle \(1991\)](#), a reversed flow transition is known to occur when the free-stream acceleration parameter is greater than 3×10^{-6} , and this parameter is evaluated to be $K = 1.35 \times 10^{-4}$ near the current flat plate leading edge. The current, K , value is about two orders of magnitude greater than the suggested value, in which reverse flow transition or “relaminarization” can be confirmed. This suggests that the detected T-S wave frequency near the flat plate leading edge has the tendency to be suppressed by the strong free-stream acceleration due to the local favourable pressure gradient. It is also reasonable to believe that the boundary layer has returned to the laminar state before the downstream boundary layer separation. Consequently, as the downstream separated-flow transition is the main context of the current investigation, it can be treated as a normal separated-flow transition process without interruption from the upstream flow events.

4.4.3 K-H Instability

With increased free-stream turbulence intensity, streaks can be found inside the boundary layer. They travel inside both the attached and the separated boundary layer, and finally merge into the transition region. As shown in [Figure 4.11](#), the presence of streaks has caused the stream-wise RMS velocity, $\sqrt{u'u'}$, to increase. As a result, a remarkable peak appears in each $\sqrt{u'u'}$ profile. This has happened for all profiles both before and after the separation point at $x/S_0 = 0.62$. whereas, in an identical simulation with zero free-stream turbulence intensity, as shown in [Figure 4.12](#), the upstream attached boundary layer is much quieter and the maximum stream-wise RMS velocity remains almost zero, only gradually increasing after the time-mean separation location at $x/S_0 = 0.59$. Inside the separated boundary layer in both simulations, the peak in the RMS velocity profiles aligns with the velocity profile point of inflection ($d^2U/dy^2 = 0$). This is expected for the separated-flow transition under adverse pressure gradient and 0%-FST, of which unsteadiness is accumulated at the lower edge of the separated shear layer. However, the point of inflection in the 3%-FST case is further apart from the boundary layer edge. This

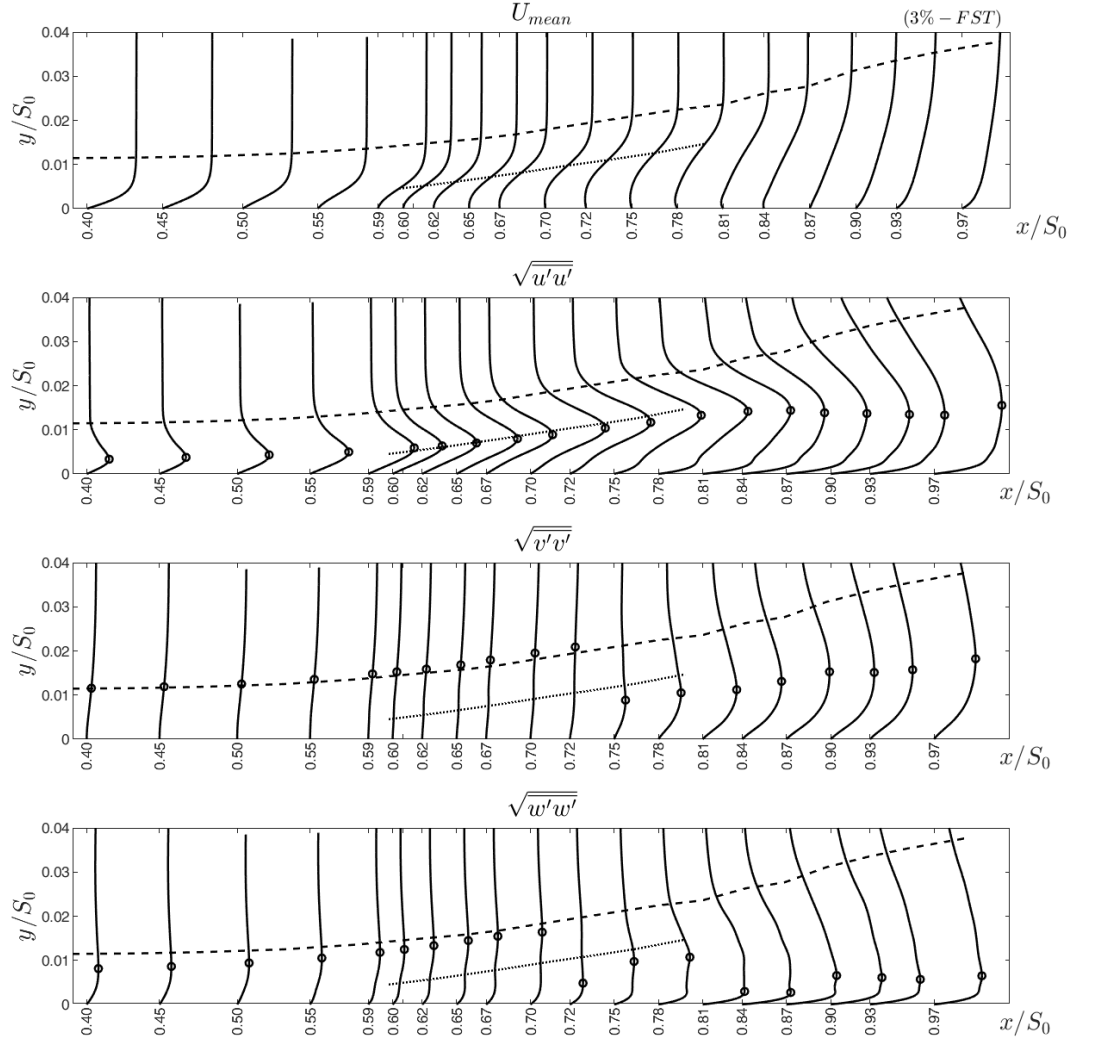


Figure 4.11: Boundary layer velocity profiles in the 3%-FST case. Solid line: Velocity profiles (U_{mean} , $\sqrt{u'u'}$, $\sqrt{v'v'}$, and $\sqrt{w'w'}$) between $x/S_0 = 0.40$ and $x/S_0 = 0.97$. Dash line: Boundary layer edge. Dotted line: Boundary layer profile point of inflection ($d^2U/dy^2 = 0$). Symbol: The maximum value of RMS velocity profile.

reveals that the thickness of the separated shear layer has increased with streaks, and that its stability condition may also have been altered. The presence of streaks alters not only the stream-wise velocity component but also the span-wise component. The maximum value of the span-wise RMS velocity profiles, $\sqrt{w'w'}$, can be identified near the edge of the attached boundary layer in the 3%-FST case, rather than close to the surface as in the 0%-FST case. For the wall-normal RMS velocity profiles, $\sqrt{v'v'}$, comparable locations of the

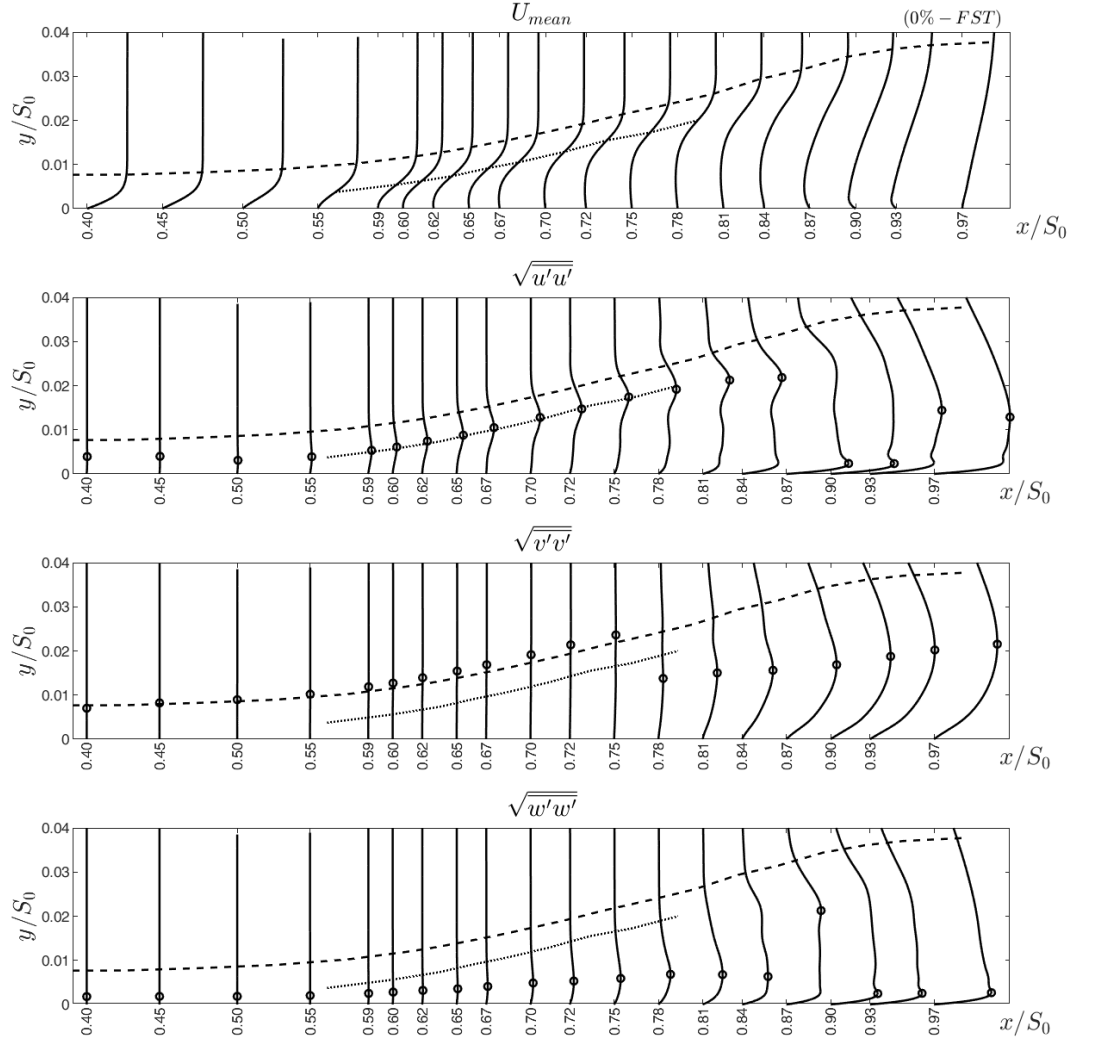


Figure 4.12: Boundary layer velocity profiles in 0%-FST case. Solid line: Velocity profiles (U_{mean} , $\sqrt{u'u'}$, $\sqrt{v'v'}$, and $\sqrt{w'w'}$) between $x/S_0 = 0.40$ and $x/S_0 = 0.97$. Dash line: Boundary layer edge. Dotted line: Boundary layer profile point of inflection ($d^2U/dy^2 = 0$). Symbol: The maximum value of RMS velocity profile.

maximum value, can be found between the two cases. Overall, the increased stream-wise RMS velocity components in the 3%-FST case indicate that perturbations exist inside the boundary layer before the laminar separation.

The existence of perturbations can cause a turbulence spot to form in the attached boundary layer and transition may even occur before the boundary layer separation. This is known to happen in bypass transition. The possibility of this happening herein has

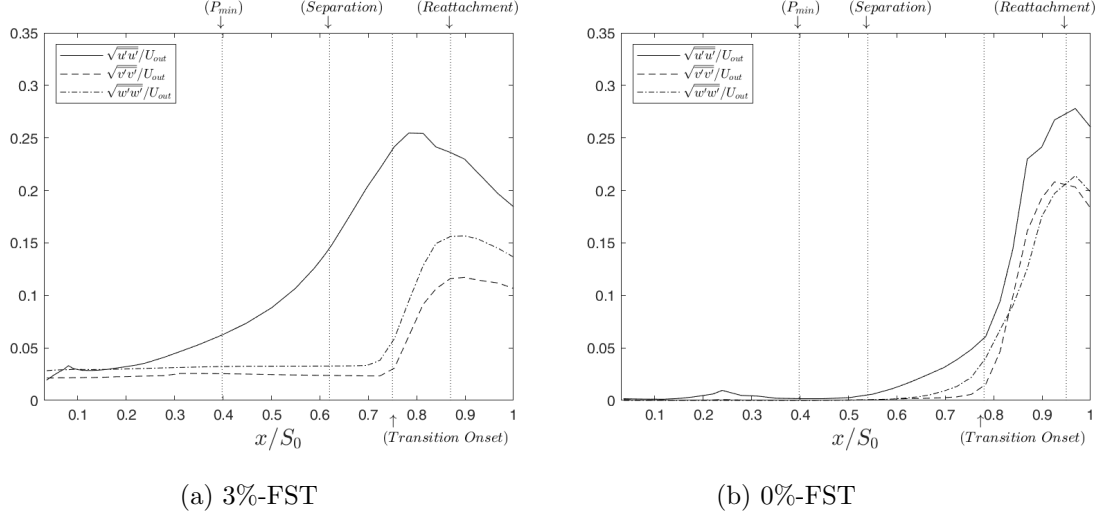


Figure 4.13: Maximum RMS velocities along the stream-wise direction. $(\sqrt{u'u'})_{max}/U_{out}$: (‘ - ’); $(\sqrt{v'v'})_{max}/U_{out}$: (‘ - - ’); $(\sqrt{w'w'})_{max}/U_{out}$: (‘ -.- ’).

been ruled out when studying the maximum RMS velocity plot in Figure 4.13a. This figure was created by joining the maximum value of each RMS velocity profile in Figure 4.11. In this maximum RMS velocity plot, both $\sqrt{v'v'}$ and $\sqrt{w'w'}$ components remain relatively constant, at approximately 0.08, and start to grow rapidly at $x/S_0 \approx 0.75$. The maximum value of both components has been reached at $x/S_0 = 0.87$, indicating that the boundary layer has evolved into a transition process. The starting location, $x/S_0 = 0.75$, can reasonably be considered as the onset location of transition. Conversely, the gradually increasing $\sqrt{u'u'}$ component before the boundary layer separation may be reminiscent of the turbulence spot formation. However, its growth rate is too steady to be related to any transitional activity. The gradually increasing $\sqrt{u'u'}$ component is caused by streak amplitude growing whilst travelling through the boundary layer. Consequently, due to the rapid growth of RMS velocity components, $\sqrt{v'v'}$ and $\sqrt{w'w'}$, identified after the boundary layer separation, the possibility for the formation of a turbulence spot and the onset of bypass transition has been excluded here.

Figure 4.13b shows the maximum RMS velocity plot of the 0%-FST case. This plot is created using the maximum value extracted from each RMS velocity profile in Figure 4.12. In this figure, two stages of the RMS velocity growth can be identified between the separation and reattachment location (inside the separation bubble). As shown in this figure, all three velocity components begin to increase gradually near the time-mean separation location at $x/S_0 = 0.54$ until $x/S_0 = 0.78$. The growth of RMS velocities in this

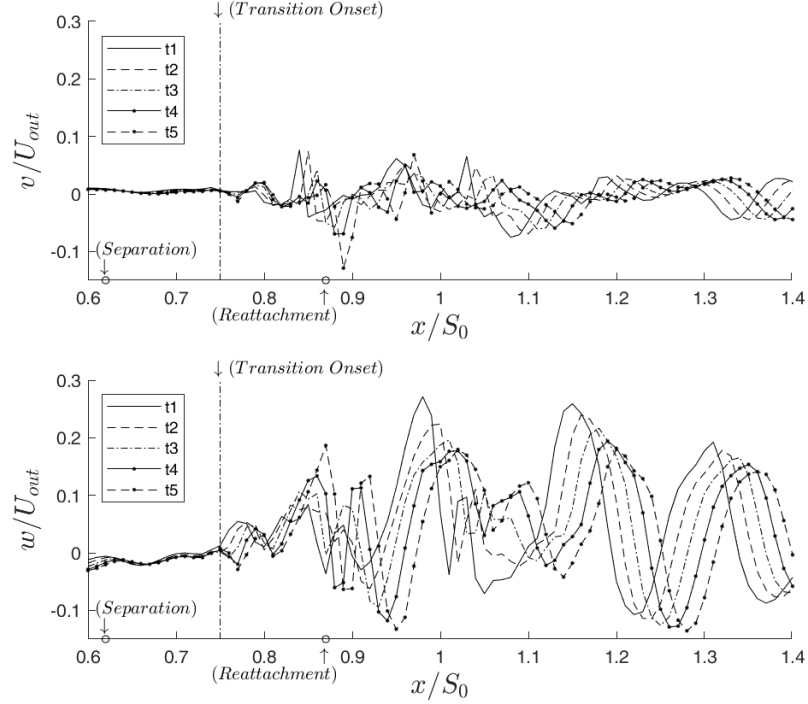
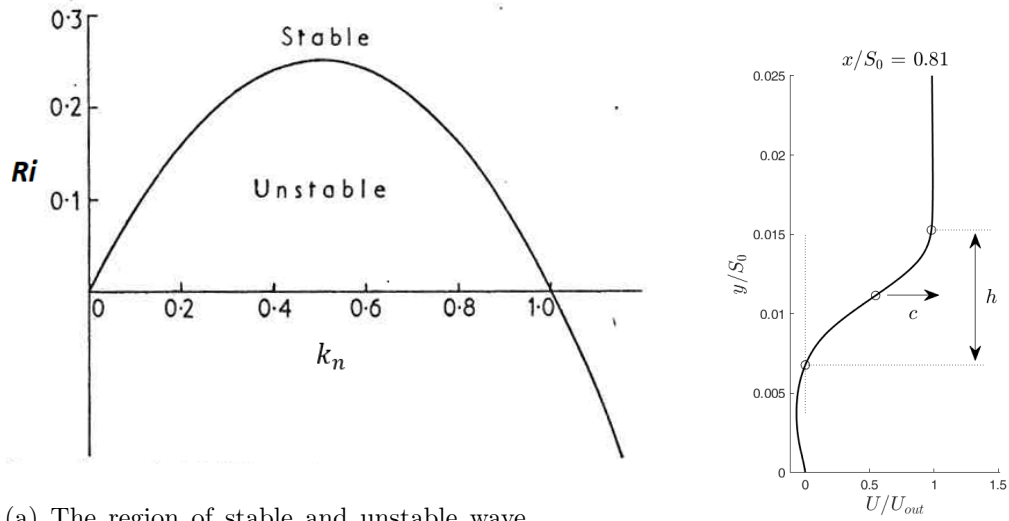


Figure 4.14: Instantaneous wall-normal and span-wise velocity components at five consecutive time steps.

region can be classified as the stage-1 growth before transition onset, with this stage having a total distance of $x/S_0 = 0.24$. In stage-2, the growth rate starts to accelerate at the transition-onset location at $x/S_0 = 0.78$ and the maximum value is reached at $x/S_0 = 0.95$ (reattachment location). This has happened within a distance of $x/S_0 = 0.17$. Whereas, in the 3%-FST case, $\sqrt{u'u'}$ velocity grows gradually since $x/S_0 = 0.1$ until the transition onset location at $x/S_0 = 0.75$. Thereafter, $\sqrt{u'u'}$, shortly reaches the maximum value at $x/S_0 = 0.80$. For the other two velocity fluctuations, $\sqrt{v'v'}$ and $\sqrt{w'w'}$, start to grow rapidly between $x/S_0 = 0.75$ and $x/S_0 = 0.87$. The total distance of $x/S_0 = 0.12$ for these velocity fluctuations to grow in the 3%-FST case is much shorter than in the 0%-FST case, resulting in a smaller separation bubble ($l_{bubble(3\%-FST)}/S_0 = 0.25$) in the 3%-FST case compared with the 0%-FST case ($l_{bubble(0\%-FST)}/S_0 = 0.41$). Clear evidence shows that the streaks have caused the change in the separation bubble size and the underlying mechanism will be further investigated in Chapter 7. Additionally, both $\sqrt{v'v'}$ and $\sqrt{w'w'}$ velocities have grown to a much stronger magnitude in a longer distance in the 0%-FST case than have those in the 3%-FST case. This has led to a more rapid stage-2 growth for the 0%-FST case. Respectively, these growth rates are 2.16% per (x/S_0) and 1.48% per

(x/S_0) for the 0%-FST and for the 3%-FST case.



(a) The region of stable and unstable wave numbers of K-H instability (Chandrasekhar (1968)).

(b) A typical separated boundary layer velocity profile from the 0%-FST case.

Figure 4.15: ‘ Ri ’: is the Richardson number, ‘ k_n ’: is the wave number, ‘ h ’: is the free shear layer thickness, and ‘ c ’: is the velocity at the point of inflection.

The transition-onset location can be further confirmed by studying the instantaneous velocity components, v and w , at five consecutive time steps. These velocity data were sampled from a constant y -location slightly below the edge of the boundary layer at mid-span. As shown in Figure 4.14, both velocity components remain steady and identical up to the location at $x/S_0 = 0.75$. Thereafter, they become and remain unsteady. Further downstream after the reattachment location at $x/S_0 = 0.87$, coherent patterns from different temporal locations can be observed. This indicates that the boundary layer is in the breakdown stage. Consequently, the boundary layer transition has happened in the region between $x/S_0 = 0.75$ and $x/S_0 = 0.87$. The initial location where the unsteadiness arises at $x/S_0 = 0.75$ can be confidently defined as the transition-onset location for the current separated-flow transition.

Due to the transition-onset location, downstream of the boundary layer separation, a separated boundary layer transition can be confirmed. Nevertheless, perturbation has been identified inside the boundary layer both upstream and downstream of the separation location. There is a strong possibility that the normal separated-flow transition routine has been altered, and that either the separated-flow transition may no longer be initiated with the primary K-H instability, or the K-H instability is no longer dominant in the

x/S_0	h/S_0	$k_n S_0$	c/U_{out}	$f_{KH(unstable)}$
0%-FST	(Mid-span)	$z/S_0 = 0.098$		
*0.78	0.0157	63.84	0.53	$0 < f < 26.99(Hz)$
0.81	0.0170	58.77	0.55	$0 < f < 25.58(Hz)$
0.84	0.0189	53.02	0.60	$0 < f < 25.34(Hz)$
3%-FST	(Mid-span)	$z/S_0 = 0.098$		
0.72	0.0166	60.17	0.56	$0 < f < 26.98(Hz)$
*0.75	0.0174	57.45	0.60	$0 < f < 27.24(Hz)$
0.78	0.0189	52.84	0.70	$0 < f < 29.61(Hz)$

Table 4.3: Frequency ranges are unstable to K-H instability. (‘ * ’: the transition-onset location).

primary instability stage. This speculation is due to the existence of streaks that travel inside the boundary layer and interrupt the normal separated-flow transition process. For a rigorous examination of the existence of the primary K-H instability, the stability analysis employed by [Yang and Voke \(2001\)](#) is adopted here. This analysis is based on the inviscid instability criterion given by [Chandrasekhar \(1968\)](#), as shown in [Figure 4.15a](#). A free shear layer with hyperbolic tangential velocity profile ($U = \tanh(y)$) and constant density (Richardson number, $R_i = 0$) is unstable to the K-H instability if $0 < k_n h < 1.0$, where k_n is the wave number and h is the free shear layer thickness. The definition of h is shown in [Figure 4.15b](#). Meanwhile, the PSD analysis of the fluctuation velocity can be used to find frequencies that match the results from the stability analysis.

After rearranging the instability criterion for the hyperbolic tangential velocity profile, this yields an unstable wave number in terms of free shear layer thickness, $0 < k_n S_0 < 1.0/(h/S_0)$. At the flat plate mid-span ($z/S_0 = 0.098$) and $x/S_0 = 0.81$ in the 0%-FST case, the free shear layer thickness is evaluated as $h/S_0 = 0.0170$. A range of wave numbers unstable to K-H instability is then calculated to be $0 < k_n S_0 < 58.77$. To find the corresponding unstable frequencies range, the angular wave number equation, $k_n = 2\pi f/c$, is used. In this equation, c is the wave-speed at the boundary layer profile point of inflection. This location is defined when the second derivative of the velocity profile, d^2U/dy^2 , is equal to 0. For the velocity profile at $x/S_0 = 0.81$ in [Figure 4.15b](#), the wave-speed is evaluated as $c/U_{out} = 0.55$. As a result, a range of characteristic frequencies

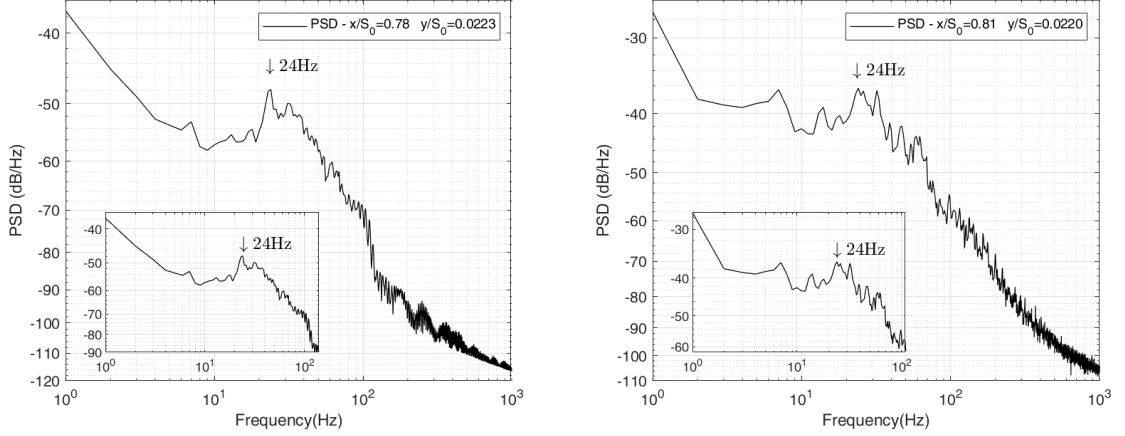


Figure 4.16: u' -velocity frequency spectra at two stream-wise locations of $x/S_0 = 0.78$ and $x/S_0 = 0.81$, and at span-wise location $z/S_0 = 0.098$ for the 0%-FST case.

unstable to the K-H instability are evaluated to be $0 < f_{KH(unstable)} < 25.58\text{Hz}$. Upon repeating this analysis at other upstream and downstream locations at $x/S_0 = 0.78$ and $x/S_0 = 0.84$, this yields different ranges of unstable characteristic frequencies, as shown in Table 4.3. In the 0%-FST case, PSD in both locations of $x/S_0 = 0.78$ and $x/S_0 = 0.81$ possesses an identical frequency peak of 24Hz as shown in Figure 4.16. This frequency peak is within the K-H unstable frequency range of $0 < f_{KH(unstable)} < 25.58(\text{Hz})$, in which the K-H instability can be confirmed to dominate in the primary instability stage with 0%-FST.

Figure 4.17 shows a vertical displaced PSD of eight stream-wise locations from the 3%-FST case. Despite the first location being sampled before the separation location, others are placed inside the separated shear layer. Of these points, one has been placed at the transition-onset location ($x/S_0 = 0.75$) and the last measurement point has been placed downstream of the shear layer trailing edge. No distinct frequency peak in the PSD can be observed from these locations. Further downstream, near the reattachment location ($x/S_0 = 0.87$), sampling points have not been displayed. However, the spectrum content of these locations has been carefully examined and no distinct frequency peak in the PSD was found either. The dominant frequency from the K-H instability, like the one found in the 0%-FST case, does not exist in the current case with elevated FST.

Remarkably, three less noticeable frequency peaks of 70Hz, 103Hz, and 140Hz (harmonic frequency of 70Hz) can be observed in both locations of $x/S_0 = 0.70$ and $x/S_0 = 0.72$ in Figure 4.18. Another frequency peak of 180Hz becomes more apparent only at

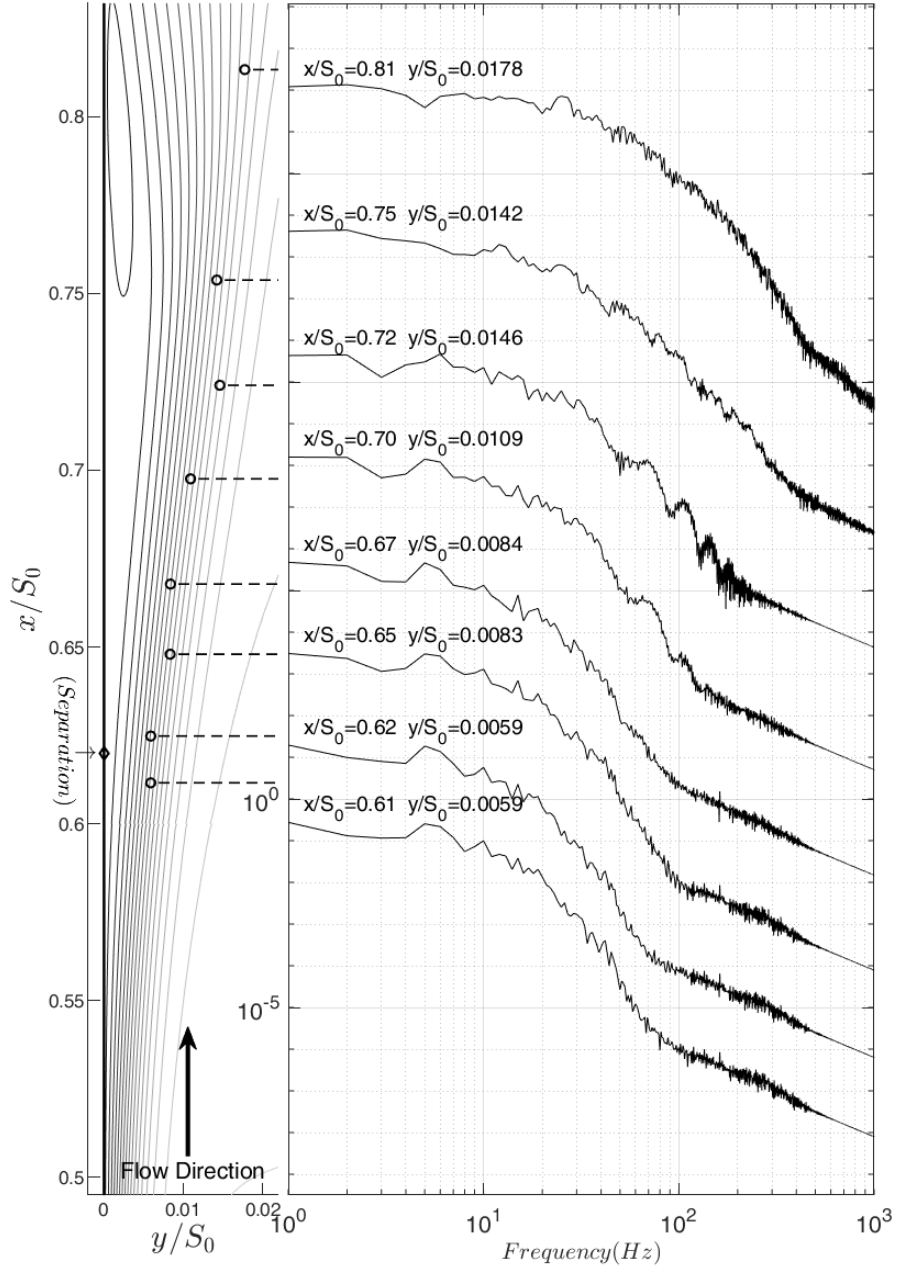


Figure 4.17: Left: Flat plate (placed vertically) and PSD sampling points ('o') within the boundary layer showing by u -velocity line contour. Right: Displaced frequency spectra of u' -velocity at stream-wise locations between $x/S_0 = 0.61$ and $x/S_0 = 0.81$. In the vertical scale of the displaced frequency spectra plot, one increment between two major ticks is 1.0×10^5 .

the location of $x/S_0 = 0.72$. The fundamental frequency of 70Hz corresponds to the vortex shedding Strouhal number ($St_\theta = f\theta/\bar{U}$) of, $St_\theta = 0.018$. This number is slightly above the one observed by [Ho and Huerre \(1984\)](#), as well as in several other experimental and computational studies. When the shear layer is under external forcing, the vortex-

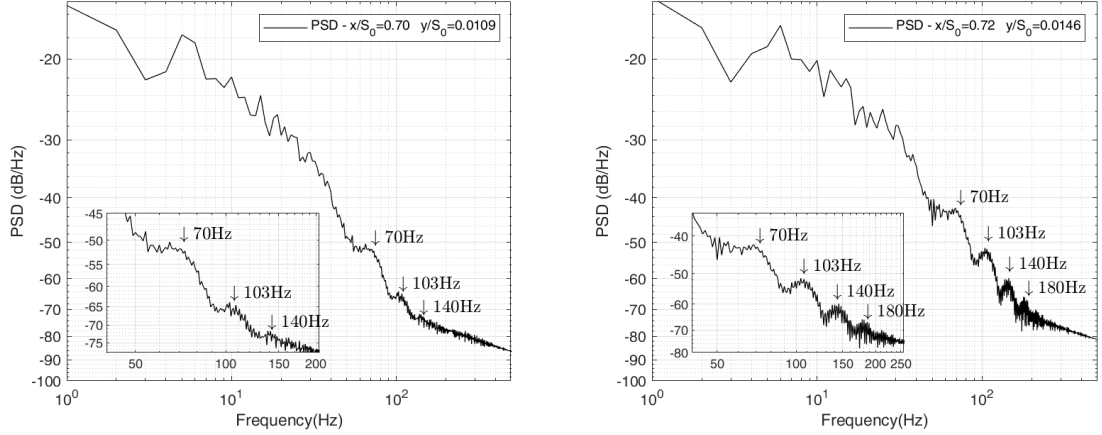


Figure 4.18: u' -velocity frequency spectra at two stream-wise locations of $x/S_0 = 0.70$ and $x/S_0 = 0.72$, and at span-wise location $z/S_0 = 0.098$ of the 3%-FST case.

formation Strouhal number should be less than 0.016 if unstable to K-H instability. The current Strouhal number ($St_\theta = 0.018$) is slightly above this value and is identical to the one calculated in the bypass flow transition, with 5.6% FST, by McAuliffe and Yaras (2008). The second fundamental frequency of 103Hz corresponds to the Strouhal number of 0.032. This coincidentally aligns with the Strouhal number of the most amplified K-H frequency, $St_\theta = 0.032$, from the unforced mixing layer in Ho and Huerre (1984). The highest frequency of 180Hz is far too large to correspond to any vortex shedding activities.

Although the first frequency peak of 70Hz, with a Strouhal number ($St_\theta = 0.018$), is slightly larger than the established value of $St_\theta = 0.016$, K-H instability is still believed to exist locally. This is because vortex shedding is a classical phenomenon of the free shear layer being inviscidly unstable to K-H instability. Nevertheless, due to the 3%-FST and streak formation, the free shear layer is intermittently disturbed. This leads to a change in the local flow conditions and a less opportunity for K-H instability to happen. Consequently, the K-H footprint in the frequency domain is very indistinct. Additionally, the occurrence of two vortex shedding Strouhal numbers not only provides strong evidence for the existence of the K-H instability, but also indicates different vortex shedding phenomena, as well as different-frequency K-H waves existing in the transition process. These are most likely to be associated with the disturbed K-H wave with a shedding Strouhal number, $St_\theta = 0.018$, or with the normal K-H wave (undisturbed) with a shedding Strouhal number, $St_\theta = 0.032$.

Flow visualisations of the transition process in both the 0%-FST and the 3%-FST

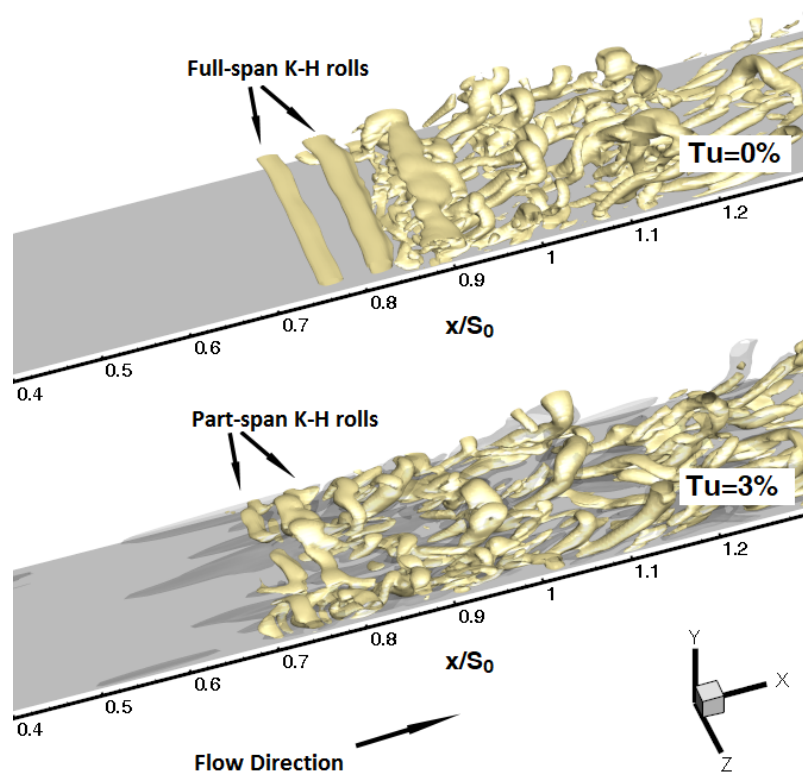


Figure 4.19: Q-criterion iso-surface flow visualisation of the transition process between the 0%-FST and the 3%-FST cases. Gold colour: Iso-surfaces at Q-criterion value of 2000, Dark colour (only in the 3%-FST case): Visualisation of streaks using the wall-normal vorticity.

cases are shown and compared in Figure 4.19. In the 0%-FST case, full-span rollers, as a result of the K-H instability, can be observed at the initial stage of the transition-onset (near $x/S_0 = 0.78$). These rollers are then further disturbed and grow exponentially. The maximum disturbance with a disturbed span-wise roller is found after $x/S_0 = 0.90$, followed by the formation of turbulent coherent structures. Whereas in the 3%-FST case, the cross-span K-H rollers have been interrupted by streaks near the transition-onset location. This leads to the formation of part-span K-H rollers, such as those appearing between $x/S_0 = 0.75$ and $x/S_0 = 0.80$. However, these part-span K-H rollers still shed off locally to form coherent structures. In Figure 4.20, a free shear layer shedding has been captured and the development of the corresponding vortex cascade has been demonstrated in this time-series plots. Due to the rapid shedding process, the K-H billow prior to turbulent breakdown, such as the one appearing in the 0%-FST case at $x/S_0 = 0.90$ (Figure 4.19), does not exist in the 3%-FST case. Nevertheless, The shedding of the part-

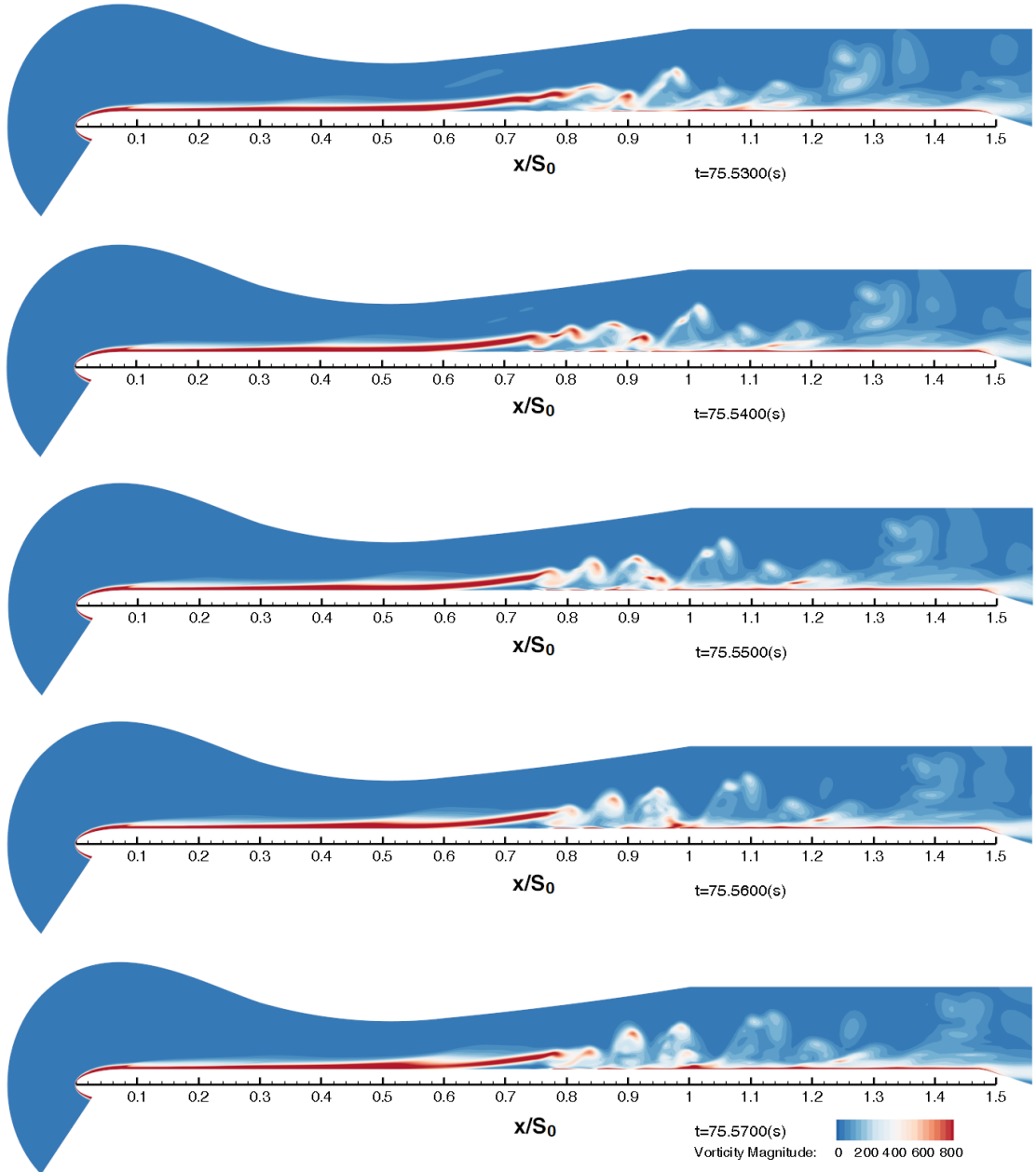


Figure 4.20: Separated shear layer vortex shedding in the 3%-FST case with the development of a vortex cascade.

span K-H rollers, and the formation of the coherent structures, provide evidence for the existence of K-H instability in the 3%-FST case. Due to indistinct features from the K-H instability, it is believed not to be the dominant mechanism triggering transition in the 3%-FST case. Other mechanisms, such as streak interaction and instability, are most likely to be responsible for the transition-onset. However, the underlying mechanism of how streak interactions can trigger separated-flow transition requires detailed investigation.

4.5 Summary

Separated-flow transition on an elliptical leading edge flat plate has been numerically investigated in detail using LES. The computational domain has been configured with two identical contour walls, mounted opposite each plate surface, which mimic the pressure distribution of the T106 low-pressure turbine. Boundary layer separation and transition on the flat plate surface is induced by the applied adverse pressure gradient. The LES approach, using the dynamic SGS turbulence model, has been employed to conduct this investigation. Large-scale, energy-contained turbulence motions are completely resolved by LES and the less important small-scale turbulence motions are modelled by the SGS turbulence model. Hence, the computational requirement can be greatly reduced, but high-fidelity resolution remains. The computational mesh has been designed carefully with high resolution mesh used to resolve important flow features. The input of the SGS turbulence model has therefore been greatly reduced to increase the accuracy of the simulation. Consequently, the predicted time-mean flow field has a good agreement with both the experimental observation and a previous numerical study.

Boundary layer transition under both 0%-FST and 3%-FST has been considered, with distinct flow structures observed. In the 0%-FST case, both the K-H frequency and the K-H related flow structures, such as cross-span K-H rollers, can be observed. Therefore, transition via the well-known K-H instability can be confirmed. In the 3%-FST case, no K-H related frequency peak is detected. Instead, streaks are formed inside the boundary layer near the plate leading edge and propagating inside both the attached and separated shear layers. The presence of these streaks is known to cause the turbulence spot formation in bypass transition. However, this type of transition is ruled out here by the investigation of three velocity fluctuations. Two of the velocity fluctuations (v' and w') increase only at the transition-onset location ($x/S_0 = 0.75$) after the boundary layer separation. In contrast, the u' -velocity fluctuation is found gradually increasing in the attached boundary layer. However, its growth rate is too low to be related to any kind of turbulence spot formation. Using flow visualisation, part-span 2D rollers can be observed, which are severely distorted by the streaks, resulting in weaker vortex shedding. Several low-energy frequency peaks, corresponding to these shedding activities, also exist in the PSD spectra. Consequently, the current transition process under 3%-FST is considered to be caused by both the streak-related instability and the well-known K-H instability. In addition, due to distortion from

the passing streaks, the span-wise 2D transitional flow structures are found to be severely disrupted and to develop rapidly into 3D motions, such as the formation of Λ -vortex. This has resulted in the bypassing of the usual secondary instability stage, which is followed by a much shorter transition length and separation bubble.

Chapter 5

Effect of Free-stream Turbulence Intensity

5.1 Introduction

The characteristics of separated-flow transition can be influenced by the changes in free-stream turbulence intensity (FSTI) and the relevant physics can also be different. As in Chapter 4, the transition mechanism is rather different between 0% and 3% FST. When under no influence from the FST, the transition process is dominated by the well-known K-H instability. However, the transition process is governed by both the streak instability and the K-H instability when FSTI is increased to 3.0%. For this reason, we ask what the transition process is when FSTI is further increased. Does a novel transition mechanism exist? Most importantly, is it similar to that under 3.0% FST and, if so, what has been changed? In order to answer these questions, the effect of FSTI is investigated in this chapter and comparison is made between four levels of FSTI.

5.2 The Simulation Configuration

In these four simulations, the employed computational domain is identical to that used in the previous chapter. The FST in these simulations were generated by the numerical tripping method discussed in Chapter 3.1.3. The resultant FSTI near the flat plate leading edge varies from 0.0% to 8%. The sampling location for these measurements is also identical to the previous studies in Chapter 4. Due to a converging diverging section present in the computational domain upstream of the transition process, free-stream flow

is accelerated in the converging section; meanwhile, the FST is suppressed and stretched. The free-stream flow is then under expansion in the diverging section. Eventually, the FSTI decreases after exiting the section, resulting in lower magnitude than that measured near the flat plate leading edge. To provide references, the FSTI was sampled again in the freestream at $x/S_0 = 0.576$ before the boundary layer separation in all cases, with the results provided in Table 5.1 .

Case	Tu (LE)	Tu_2 ($x/S_0 = 0.576$)	Δy^+ (τ_w at $x/S_0 = 0.12$)	Δx^+	Δz^+
Case-0.0	0.0	0.0	0.78	12.84	15.53
Case-3.0	3.0	2.1	0.84	13.89	16.81
Case-4.7	4.7	2.5	0.69	8.52	9.87
Case-8.0	8.0	4.0	0.67	8.22	9.53

Table 5.1: Non-dimensional mesh sizes in four simulations with different FSTI. In this table, Tu : free-stream turbulence intensity sampled near the flat plate LE; Tu_2 : free-stream turbulence intensity sampled before boundary layer separation at $x/S_0 = 0.576$.

In each case, the non-dimensional mesh sizes, Δy^+ , Δx^+ , and Δz^+ calculated from the wall shear stress value, τ_w at $x/S_0 = 1.2$, are also included in Table 5.1. Apparently, smaller Δx^+ and Δz^+ values can be found in both high FSTI cases, Case-4.7 and Case-8.0, in which the refined mesh (Mesh-8M) is used in these simulations. Details of this refined mesh can be found in Section 4.3. The reason for employing the refined mesh (Mesh-8M) is that the Δx^+ and Δz^+ values in Case-3.0 are approaching the desirable level of $\Delta x^+ < 15$ and $\Delta z^+ < 20$ for a wall-resolved LES calculation (Choi and Moin (2011)). A value at these thresholds indicates that the near wall control-volume aspect ratio is becoming critical for the given flow field. The two higher FSTI cases can have even stronger velocity variation than the 3.0% FST case. As in Case-8.0, velocity can fluctuate between $\pm 8.0\%$, which respectively yields an estimated maximum Δx^+ and Δz^+ to be 15.012 and 18.155. Despite this estimation being based only on an ideal situation with linear relationship between the FSTI and near wall control-volume dimensions, the estimated Δx^+ value is already above the desirable value of $\Delta x^+ < 15$. The refined mesh is therefore selected to allow a better resolved flow field in the two high FSTI cases. The resultant values of Δx^+ and Δz^+ show a positive outcome from using the refined mesh,

with these two values being lowered to less than 10.

In the two high FSTI simulations, Case-4.7 and Case-8.0, the time-step size of 1.0×10^{-4} is used, identical to that used in the two lower FSTI cases. When compounded with the refined mesh, the resultant CFL number is below 0.3 in regions around the separation bubble. The sampling strategies in the two higher FSTI cases are similar to those employed in the two lower FSTI cases which can be found in Section 4.2. Time-averaged sampling of the complete flow domain and collection of time-dependent data from sampling points are executed at each time step. The three-dimensional velocity and pressure data of blocks near the upper flat plate surface are collected at every 20 time steps for flow visualisation.

5.3 Time-averaged Flow Characteristics

5.3.1 Time-averaged Wall Shear Stress

Figure 5.1 shows the comparison of wall shear stress distributions from different FSTI cases.

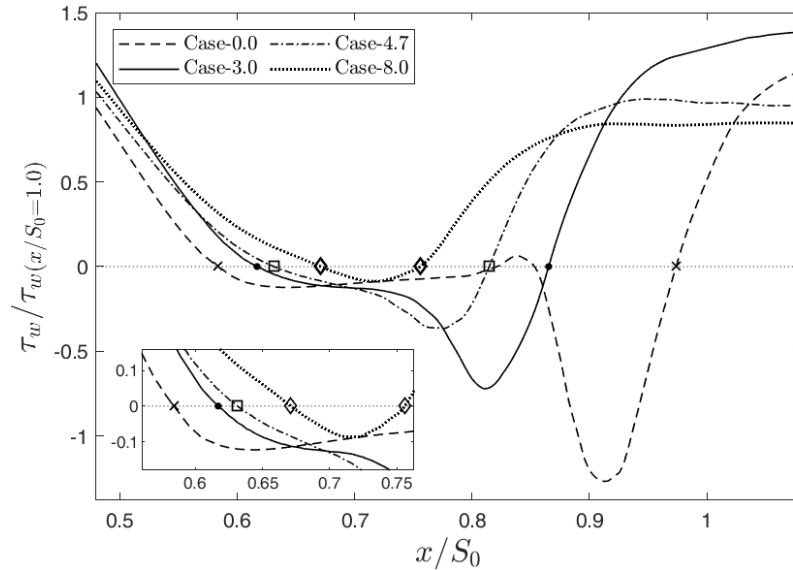


Figure 5.1: Comparison of wall shear stress under the influence of different FSTI. Symbols are showing the boundary layer separation and reattachment locations respectively located on the left-hand-side and right-hand-side.

Apparently, the largest separation bubble, defined by the difference between separation and reattachment location, can be found in Case-0.0. In this case, the boundary layer is under no influence from the FST. The time-mean separation happened in the most up-

stream location at $x/S_0 = 0.584$ and the reattachment happened in the most downstream location at $x/S_0 = 0.974$. This results in the longest separation bubble, $l/S_0 = 0.390$, among the four cases under investigation. When under no influence from the FST, the time-mean wall shear stress briefly becomes positive at $x/S_0 = 0.8$. This is mainly caused by the reversed flow being trapped inside the separation bubble, which is formed when K-H rollers trying to break up from the free shear layer and roll into the plate surface. This causes a brief increase in velocity adjacent to the plate surface, as well as leading to positive wall shear stress. Similar observation of a positive wall shear stress within the separation bubble was also reported by [Hosseinverdi and Fasel \(2018\)](#) in their 0.0% FST case. After briefly becoming positive, the wall shear stress decreased rapidly to the lowest value at $x/S_0 = 0.916$. This is when the K-H rollers completely detach from the shear layer and are in the process of so-called vortex shedding. In this process, the K-H roller gradually rolls away towards the downstream. The wall shear stress returns to a positive value after the reattachment location and when the boundary layer becomes fully turbulent.

Case	Tu (LE)	Tu ₂ ($x/S_0 = 0.576$)	SepX (x/S_0)	ReaX (x/S_0)	l_{bubble} (l_{bubble}/S_0)	h_{bubble} (h_{bubble}/S_0)	TR_{onset} (x/S_0)
Case-0.0	0.0	0.0	0.584	0.974	0.390	0.106	0.82
Case-3.0	3.0	2.1	0.617	0.865	0.248	0.075	0.75
Case-4.7	4.7	2.5	0.631	0.815	0.184	0.072	0.73
Case-8.0	8.0	4.0	0.671	0.756	0.085	0.066	0.70

Table 5.2: Separation bubble characteristics in different cases. In this table, Tu : free-stream turbulence intensity sampled near the flat plate LE; Tu_2 : free-stream turbulence intensity sampled before boundary layer separation at $x/S_0 = 0.576$; $SepX$: separation location; $ReaX$: reattachment location; l_{bubble} : separation bubble length; h_{bubble} : separation bubble maximum thickness; TR_{onset} : transition onset location.

When FSTI was increased to 3.0% in Case-3.0, the time-mean separation location moved slightly towards the downstream at $x/S_0 = 0.617$ and the time-mean reattachment location also moved. However, this movement was towards the upstream at $x/S_0 = 0.865$. This yielded a time-mean separation bubble length of $l_{bubble} = 0.248$, which is about 36% shorter than that under no influence from FST. The minimum negative wall shear

stress in Case-3.0 is also found to be higher than the one in Case-0.0. This is due to the formation of a localised K-H roller and the associated vortex shedding is no longer a sustained event under the presence of FST. The period for these events to occur takes longer when the level of FST becomes higher. This aligns with the finding from Chapter 4 that weaker vortex shedding activities were discovered in the higher FST case (3.0%). This phenomenon can also be observed from the wall shear stress distribution in Case-4.7, with the even higher FSTI of 4.7%, where the minimum wall shear stress has doubled from Case-3.0 and more than tripled from Case-0.0. As a result, the separation bubble length in Case-4.7 has reduced to $l_{bubble} = 0.184$, which is about a 26% reduction from Case-3.0. In Case-8.0, with 8.0% FSTI measured near the flat plate leading edge and 4.0% FSTI measured before the transition onset location, the large concave of wall shear stress found in the previous cases no long exists. The overall appearance of the wall shear stress curve is rather similar to that in bypass transition, as reported by [Bhushan et al. \(2018\)](#) and [Jacobs and Durbin \(2001\)](#). Nevertheless, negative wall shear stress can be found between $x/S_0 = 0.671$ and $x/S_0 = 0.756$, which indicates the existence of a reverse flow region. Also, a separation bubble still exists with further reduced length of $l_{bubble} = 0.085$. This suggests that a free shear layer and vortex shedding may still exist in the current highest FSTI case; however, this can be a rather rare event. Consequently, the transition process is considered to be predominantly caused by the streak instability which is also an instability mechanism found in bypass transition ([Jacobs and Durbin \(2001\)](#)). However, the occasionally occurring vortex shedding from K-H instability leads to the wall shear stress going below the zero-line. Therefore, the current transition mechanism can be the combination of the two instability mechanisms, which can randomly occur in space and time. Additionally in Case-8.0, the negative portion of the wall shear stress curve has an inverse parabolic appearance. This is rather different in the lower FSTI cases. As in Case-0.0, the initial separated shear layer is represented by a small inclined curve between $x/S_0 = 0.584$ and $x/S_0 = 0.800$ (the dash line in Figure 5.1). This reveals that the increased FSTI has significantly reduced the length of the initial separated shear layer at the initial stage of the transition process. The underlying mechanism may also be caused by the formation of boundary layer streaks.

5.3.2 Boundary Layer Shape Factor

In boundary layer theory, thickness parameters consist of displacement thickness, δ^* , momentum thickness, θ^* , and shape factor, H . These parameters are respectively defined by Eqn. 5.1, Eqn. 5.2, and Eqn. 5.3. The displacement thickness, δ^* , is defined as the displacement area in potential flow due to the decrease in velocity in the boundary layer. The momentum thickness, θ^* , is defined as the momentum deficit of free-stream flow due to the presence of the boundary layer and its viscous effect. Lastly, the shape factor is defined as the ratio between the displacement thickness, δ^* , and the momentum thickness, θ^* .

$$\delta^* = \int_0^{\infty} \left(1 - \frac{u}{U_{fs}}\right) dy \quad (5.1)$$

$$\theta^* = \int_0^{\infty} \frac{u}{U_{fs}} \left(1 - \frac{u}{U_{fs}}\right) dy \quad (5.2)$$

$$H = \frac{\delta^*}{\theta^*} \quad (5.3)$$

Figure 5.2 shows the boundary layer shape-factor curves in different FSTI cases. At $x/S_0 = 0.44$ before any boundary layer separation in all cases, the shape factor value is almost identical in all four cases, which is approximately $H = 2.46 \pm 2\%$. This value is close to the Blasius boundary layer shape factor value of $H = 2.59$ in laminar flow. In the downstream developed boundary layer at $x/S_0 = 1.2$, the shape factor value is also very similar in all cases, which is approximately $H = 1.56 \pm 2.0\%$. The Blasius boundary layer shape factor for a typical turbulent flow is $H = 1.4$. Both the current shape factor values are close to the Blasius boundary layer, but not identical. These discrepancies are expected as the Blasius boundary layer shape-factor value was concluded from laminar boundary layer flow. Furthermore, the transition onset location can be obtained using the shape-factor curve in Figure 5.2. The stream-wise location of the maximum shape factor value can be defined as the transition onset location. In this location, the momentum thickness dramatically increases and the displacement thickness decreases. As shown in the last column of Table 5.2, the transition onset locations are at, $x/S_0 = 0.82, 0.75, 0.74$ and 0.70 , respectively, for Case-0.0, Case-3.0, Case-4.7, and Case-8.0.

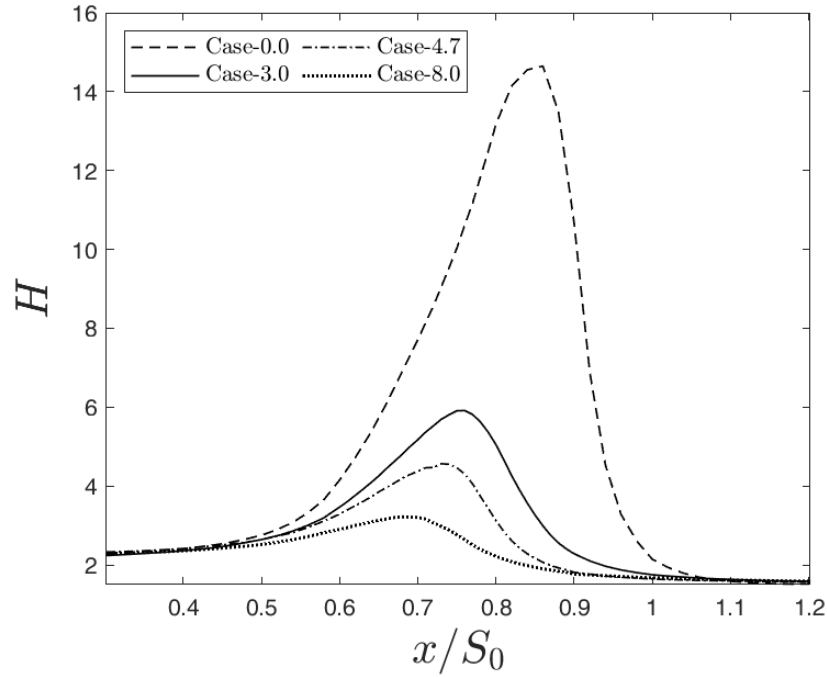


Figure 5.2: Comparison of boundary layer shape-factor curves under the influence of different FSTI.

5.3.3 Time-averaged Velocity Profiles

Figure 5.3 shows the comparison of time-averaged velocity profiles under the influence of different FSTI. Aligned with findings from the wall shear stress distribution in Figure 5.1, the longest separation bubble can be identified in Case-0.0. Not only this separation bubble is the longest, but it is also the thickest when under no influence from FST. Under elevated FST, the separation bubble size decreases in both length and thickness. This yields a separation bubble thickness of $h_{bubble}/S_0 = 0.106, 0.075, 0.072$, and 0.066 , respectively, for Case-0.0, Case-3.0, Case-4.7, and Case-8.0. Clearly, the relationship between FSTI and separation bubble thickness is non-linear. Significant reduction ($h_{bubble}/S_0 = -0.031$) can be found when the FSTI is increased from 0.0% to 3.0%, and only minor differences exist ($h_{bubble}/S_0 = -0.009$) when FSTI increases from 3.0% to 8.0%. The separation bubble height is found to be very sensitive to the presence of FST, such as switching FST on and off. However, after FST is switched on, the sensitivity reduces dramatically when FSTI is further increased from 3.0% to 8.0%. This is found to be caused by the formation of boundary layer streaks which have significantly altered the transition process. As reported in Chapter 4, the transition onset is dominated by multiple instability mechanisms in

elevated FST, contrasting with minimal FST that only a single instability mechanism (K-H) is at work. These multiple instability mechanisms are known as streak instability and K-H instability. The characteristics of streak instability can be altered when FSTI varies. Regarding to the transition process, influence from the change of streak characteristics is less significant than the presence of streaks and the occurrence of the multiple instability mechanisms. Therefore, the separation bubble height is significantly reduced when FST is switched on. Conversely, the reduction in bubble size is much less when FSTI increases from 3.0% to 8.0%.

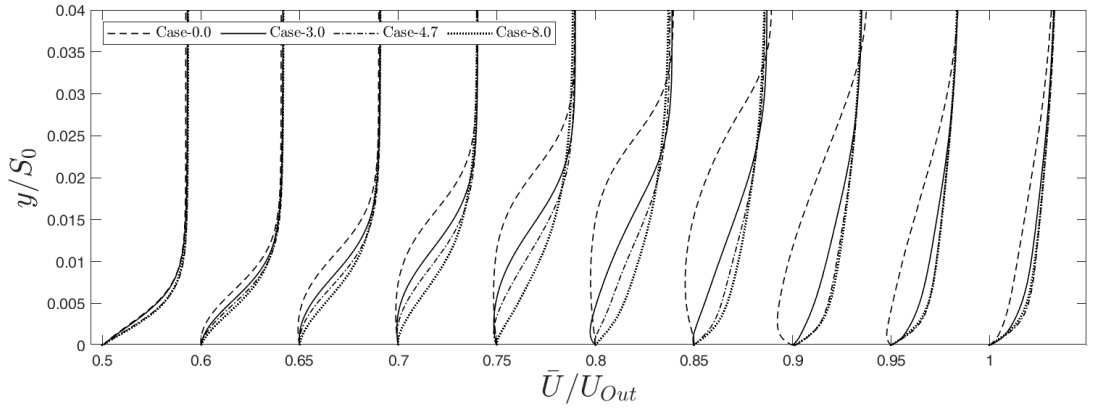


Figure 5.3: Comparison of velocity profiles under the influence of different FSTI.

5.3.4 Time-averaged Velocity Distribution

Further illustration of separation bubble size variation under the influence of FSTI can be observed in Figure 5.4, which shows velocity distribution curves from different cases. Noticeably, a tiny separation bubble exists in Case-8.0 with the transition onset location being immediately after the separation location. The boundary layer separates due to the local adverse pressure gradient, whereas, the strong magnitude streaks travelling inside the boundary layer have disrupted the free shear layer, leading to an early transition. This aligns with findings from the shear stress curve in Figure 5.1, in which an inverse parabolic wall shear stress curve can be found under the zero line, indicating that the corresponding free shear layer existed only briefly. In all cases, the maximum free-stream velocity is found immediately after the transition onset. These locations are $x/S_0 = 0.88, 0.79, 0.76,$ and $0.74,$ respectively, for Case-0.0, Case-3.0, Case-4.7, and Case-8.0, and are considered as the locations of maximum bubble thickness.

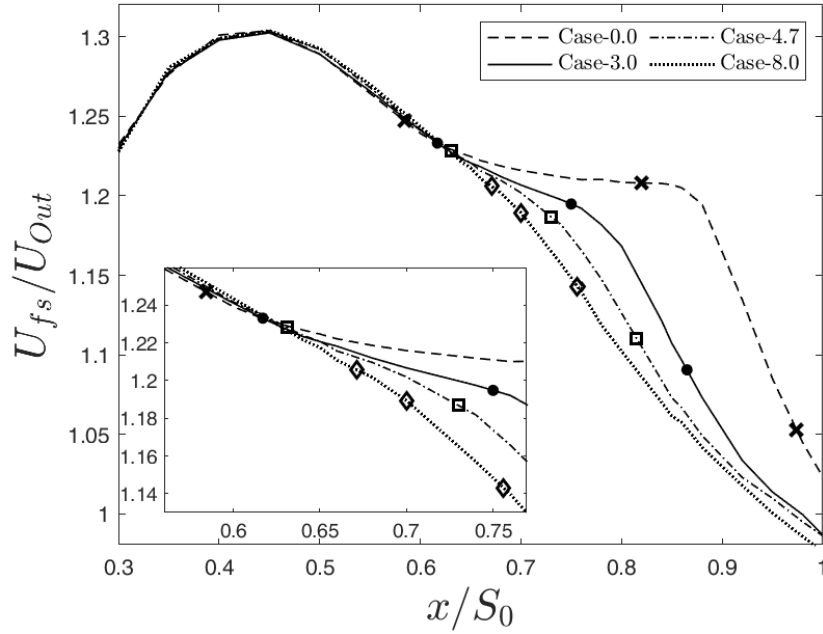
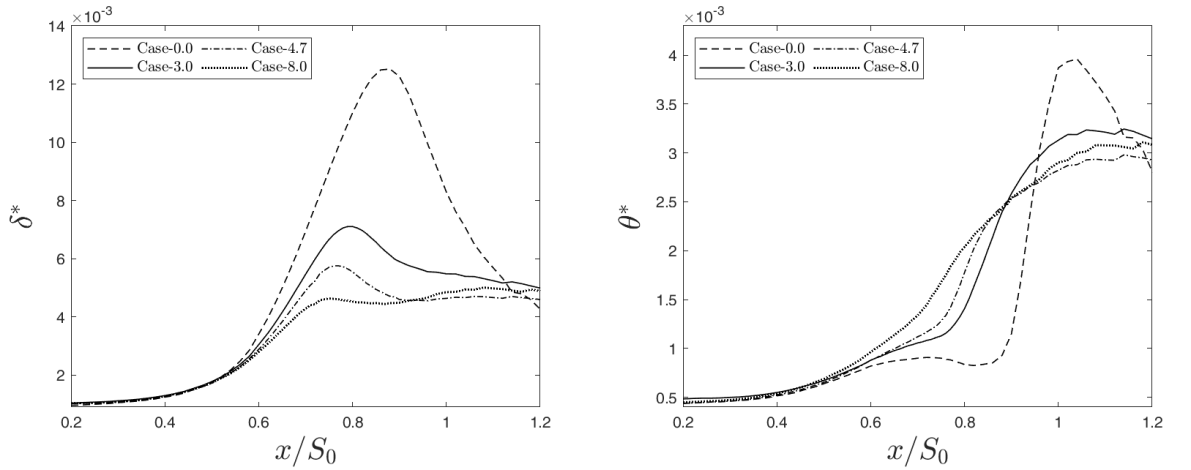


Figure 5.4: Comparison of velocity distribution under the influence of different FSTI. For each curve, the first symbol indicates the separation location, the second symbol indicates the transition onset location, and the third symbol indicates the reattachment location. This order follows the free-stream flow direction.

5.3.5 Displacement and Momentum Thickness

The influence under different levels of FST on boundary layer thickness parameters is studied here. Figure 5.5a and Figure 5.5b, respectively, show the displacement and the momentum thickness. In the displacement-thickness curves shown in Figure 5.5a, the maximum separation bubble displacement thickness can be found from the first peak of each displacement-thickness curve. These locations correspond to the maximum separation bubble thickness found from the free-stream velocity distribution analysis in Figure 5.4. The nonlinear relationship between FSTI and separation bubble displacement thickness can be observed again, and this aligns with the previous discussion in separation bubble thickness. In the first three lower FSTI cases (Case-0.0, Case-3.0, and Case-4.7), the maximum displacement thickness is observed within the separation bubble and is higher than the value in the downstream developed turbulent flow region. However, in Case-8.0 with 8.0% FSTI, the maximum displacement thickness within the separation bubble is 4.63×10^{-3} at $x/S_0 = 0.75$. This value is lower than the maximum value (5.00×10^{-3}) found in the downstream developed region at $x/S_0 = 1.08$. This contrasts with other FSTI

cases. The curve in Case-8.0 is becoming similar to that in bypass transition. In here, bypass transition refers to the dominant instability mechanism, such as K-H instability and associated vortex shedding, which is bypassed due the formation of turbulence spots, and transition onset occurs before the boundary layer separation. The burst of turbulence spots can cause the sudden increase in boundary layer displacement thickness in the developed region. However, a small separation bubble, similar to the current case, has not been previously reported in bypass transition, and wall shear stress in bypass transition does not go below zero. This indicates that the current transition mechanism, even under 8.0% and 4.0% FSTI, measured respectively near the plate LE and upstream of transition, remains fundamentally different to that in bypass transition.



(a) Comparison of displacement thickness, δ^* , under the influence of varying FSTI.

(b) Comparison of momentum thickness, θ^* , under the influence of varying FSTI.

Figure 5.5: Comparison of boundary layer thickness parameters under the influence of different FSTI.

Figure 5.5b shows the momentum thickness plot from Case-0.0. There is a considerable amount of momentum deficit near $x/S_0 = 1.0$, which is the region with vortex shedding activities. This flow phenomenon has caused a major momentum loss during the transition process under 0.0% FST. Conversely, in all elevated FSTI cases (Case-3.0, Case-4.7, and Case-8.0), momentum deficit gradually increases from the separation location, reaching the maximum value after $x/S_0 = 1.0$, which indicates that unsteady events, such as boundary layer streaks, exist even in the early stage of shear layer separation and cause increased momentum deficit. The most linear increase in momentum deficit can be found in Case-8.0 with unsteady events being the strongest among all cases. This agrees strongly with

the wall shear stress plot (Figure 5.1) that laminar separation is considered either not to exist, or to exist only briefly. This is due to the interruption from the strong unsteady events, such as streaks. From both plots, the boundary layer thickness, as well as the transition process, in three elevated FSTI cases (Case-3.0, Case-4.7, and Case-8.0) can be considered quite similar. The onset of the transition process is caused by the previously discussed multiple instability mechanisms which is the combination of streak instability and K-H instability. Boundary thickness curves of the three elevated FSTI cases again show distinct differences to the 0.0% FST case, and their transition mechanism is also different to the 0.0% FST case with transition developed only through K-H instability.

5.3.6 The Maximum RMS Velocities

In Section 4.4.3, the two lower FSTI cases (Case-0.0 and Case-3.0) were ruled out for any turbulence spot formation before transition onset. This also indicates that the transition process in both these cases was not that of bypass transition. For the two higher FSTI cases (Case-4.7 and Case-8.0), the maximum RMS velocity plot is also employed here to examine for turbulence spot formation. As shown in Figure 5.6, the maximum RMS velocity distribution is created by joining the maximum values extracted from each RMS velocity profiles along the stream-wise direction. This approach is also similar to that in Section 4.4.3. As shown in Figure 5.6a, the $\sqrt{u'u'}$ velocity in Case-4.7 gradually increased from the upstream location at $x/S_0 = 0.2$ until reaching the maximum value at $x/S_0 = 0.77$. The growth rate of the current $\sqrt{u'u'}$ curve is similar to that of Case-3.0 in Figure 4.13a, without any rapid increase before transition onset. Similar observations can be made from the corresponding momentum thickness curve in Figure 5.5b which is also without any sudden increase in momentum deficit. For the other two velocity components, $\sqrt{v'v'}$ and $\sqrt{w'w'}$, these remain constant until the transition onset location at $x/S_0 = 0.73$. Thereafter, they grow rapidly and reach the maximum value at $x/S_0 = 0.84$. This rapid growth is caused by the onset of separated-flow transition rather than by any other instability mechanism such as turbulence spot of bypass transition. Both the gradually increased $\sqrt{u'u'}$ velocity and the steady $\sqrt{v'v'}$ and $\sqrt{w'w'}$ velocities before the transition onset indicates that there is no turbulence spot formation in the current case. This also implies that the transition process in Case-4.7 is not bypass transition. The same analysis is also applied to Case-8.0, for which the maximum RMS velocity distribution is shown in Figure 5.6b. As with

Case-3.0 and Case-4.7, the $\sqrt{u'u'}$ velocity gradually increases from the upstream boundary layer before reaching the maximum value shortly after the transition location. The other two velocity components, $\sqrt{v'v'}$ and $\sqrt{w'w'}$, remain constant before the transition onset. They then increase rapidly to reach the maximum value at $x/S_0 = 0.80$. Because there is no sudden increase in RMS velocity before transition onset, the transition process in Case-8.0 is again not that of bypass transition.

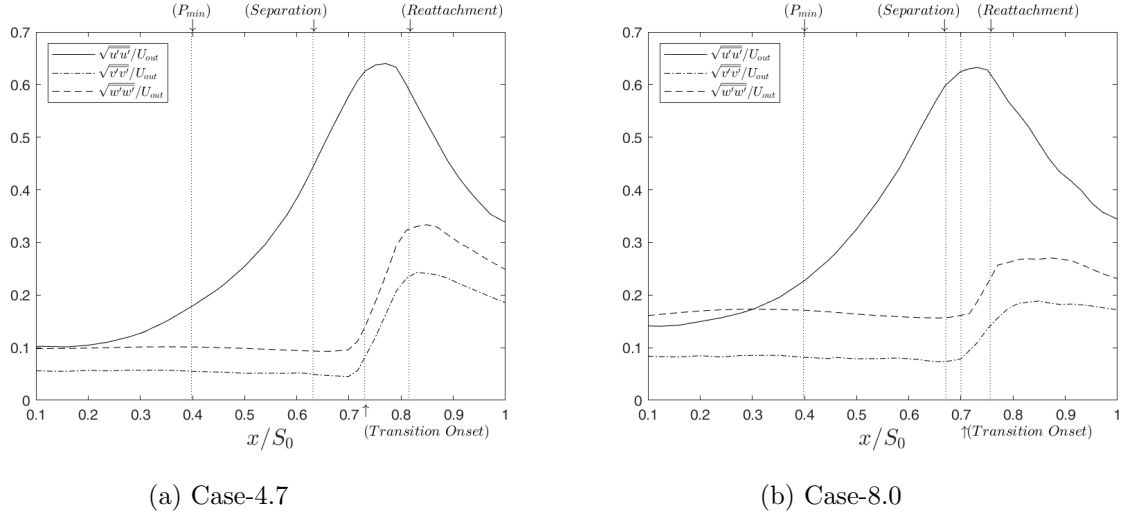


Figure 5.6: Maximum RMS velocities along the stream-wise direction. $(\sqrt{u'u'})_{max}/U_{out}$: (‘ - ’); $(\sqrt{v'v'})_{max}/U_{out}$: (‘ -.- ’); $(\sqrt{w'w'})_{max}/U_{out}$: (‘ - - ’).

Case-8.0 has the highest magnitude in the $\sqrt{u'u'}$ curve at the initial stage of the boundary layer ($x/S_0 = 0.1$), which is about 0.15. This is followed by Case-4.7 with a value of 0.1, and Case-3.0 with a value of 0.074. In contrast, the value in Case-0.0 at $x/S_0 = 0.1$ is close to zero (Figure 4.13b). Clearly, the upstream boundary layer in the three elevated FST cases contains a certain amount of energy according to the increased RMS value. This energy is transferred to the boundary layer by the free-stream turbulence packets through shear sheltering and such energy is believed to be the origin of boundary layer streaks. As FSTI increases, the other two velocity components, $\sqrt{v'v'}$ and $\sqrt{w'w'}$, also have higher magnitudes at similar location. This effect is more significant in $\sqrt{w'w'}$ component, in which the initial value is even higher than the $\sqrt{u'u'}$ component in Case-8.0.

5.4 Flow Visualisation

In the discussion of maximum RMS velocity in the previous Section 5.3.6, the transition process of the two elevated FSTI cases (Case-4.7 and Case-8.0) is not that of bypass transition. With the existence of the boundary layer streaks, the transition process in these two cases is considered equivalent to the previously discussed transition mechanism under 3%-FST. This is most likely to be governed by multiple instability mechanisms, such as streak instability and K-H instability, which are both at work. In order to confirm the existence of the K-H instability, flow visualisation is employed here to capture any vortex shedding activity. This phenomenon is known to be associated with K-H instability. Figure 5.7 shows flow visualisation on a mid-span xy -plane in Case-4.7. In this figure, a localised vortex shedding process is clearly captured. At the beginning of the process, before $t = 65.27(s)$, the separated shear layer starts to ripple. This is followed by the formation of a vortex cascade between $x/S_0 = 0.72$ and $x/S_0 = 0.86$ at $t = 65.29(s)$. In later time steps, the vortex cascade starts to separate and the individual vortex is shedding towards downstream. This captured vortex shedding activity can confirm the existence of the localised K-H instability in Case-4.7. As shown in Figure 5.8, a similar vortex shedding activity is also captured in Case=8.0. This vortex shedding happens even further away from the plate surface with a small amount of “dead air” being contained in the near wall region between $x/S_0 = 0.6$ and $x/S_0 = 0.70$. This aligns with previous findings indicating that the separation bubble indeed exists. Also, the captured vortex shedding can confirm the existence of localised K-H instability in Case-8.0.

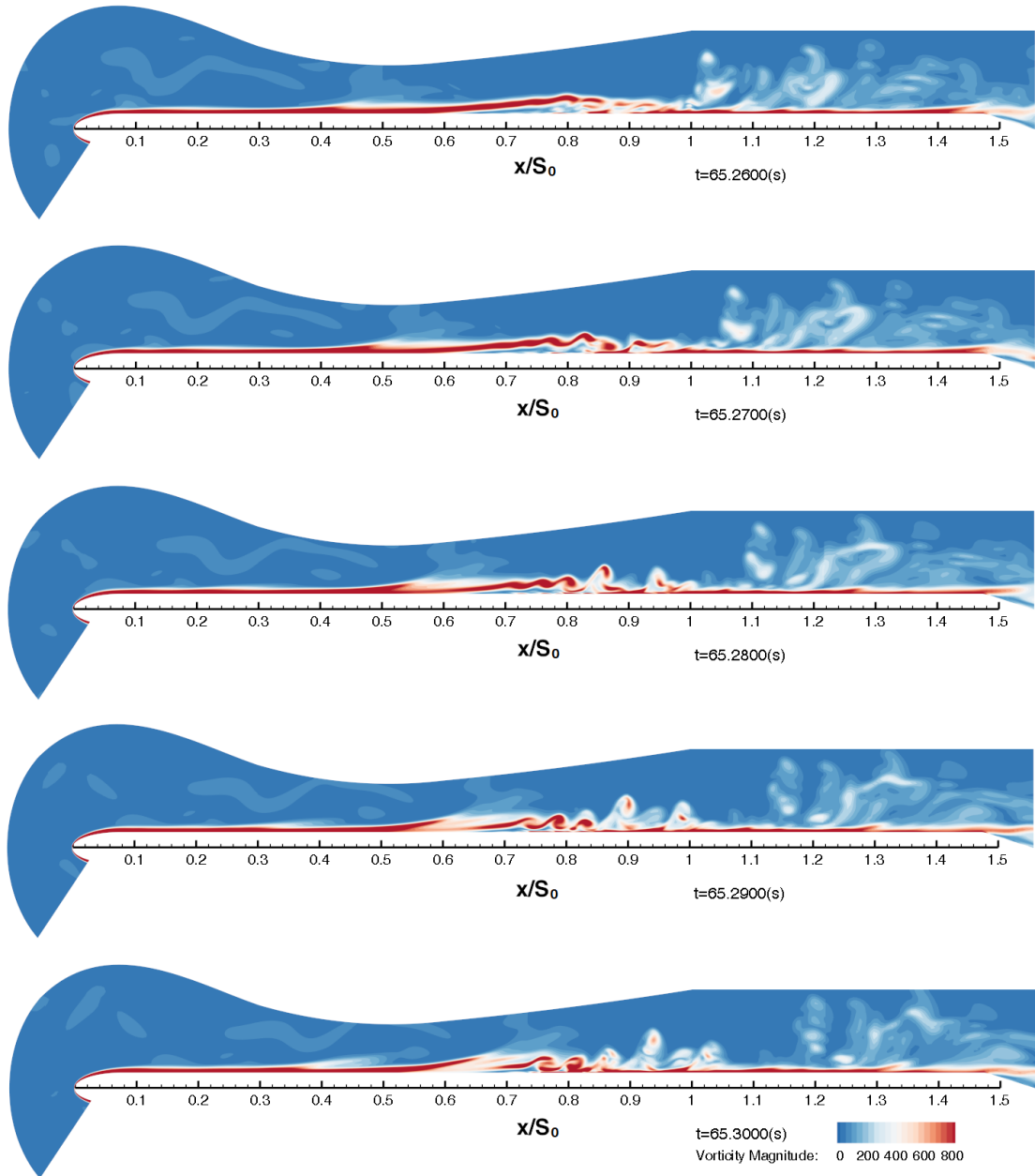


Figure 5.7: Mid-span xy -plane flow visualisation of Case-4.7. Contour shows vorticity magnitude with values between 0 and 800.

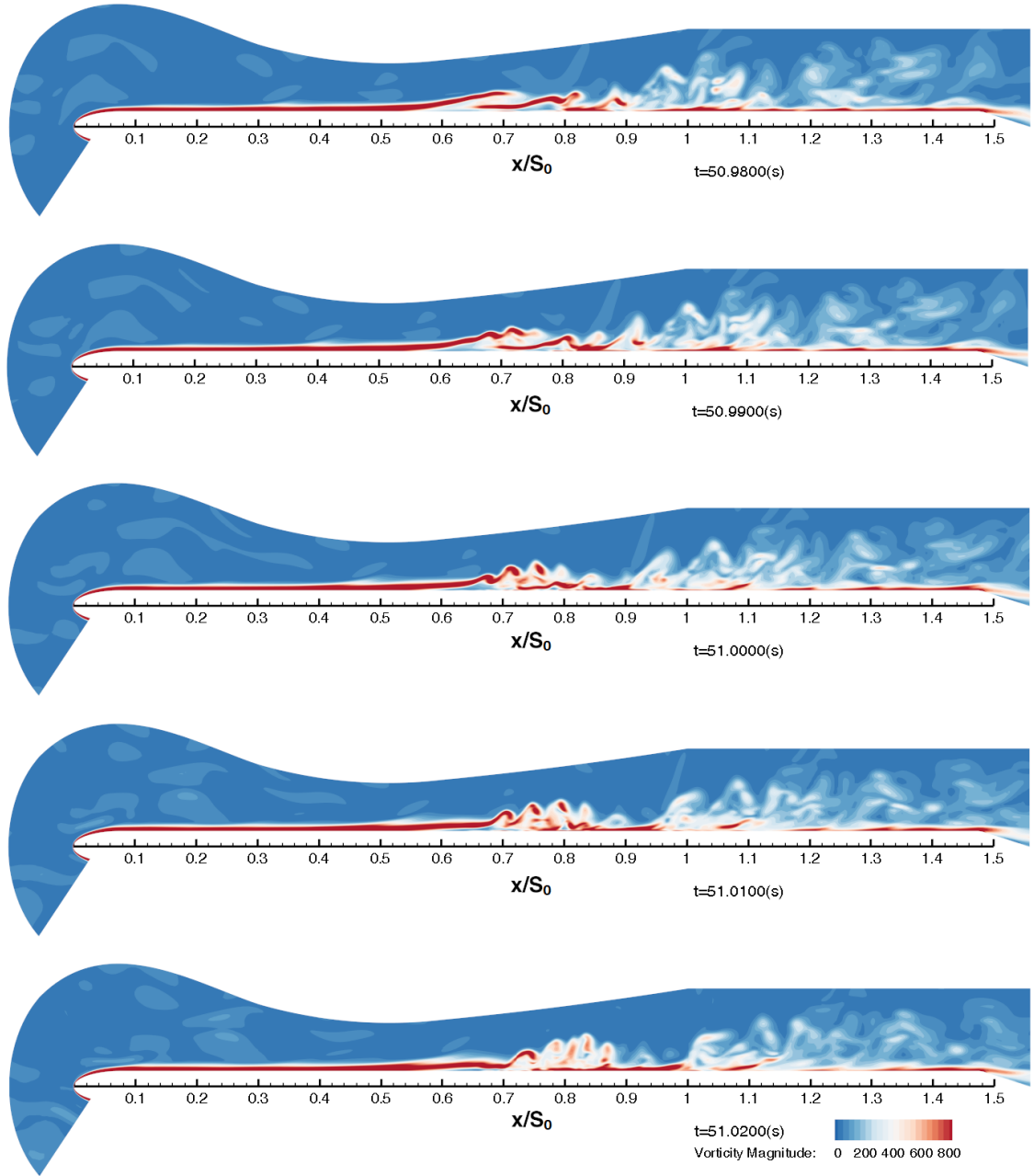


Figure 5.8: Mid-span xy -plane flow visualisation of Case-8.0. Contour shows vorticity magnitude with values between 0 and 800.

5.5 Summary

The effect of different levels of FSTI on separated-flow transition is investigated in this Chapter. This is achieved by comparing results from four simulations with FSTI measured at the LE as 0.0%, 3.0%, 4.7%, and 8.0%, respectively, for Case-0.0, Case-3.0, Case-4.7, and Case-8.0. These simulations were carried out in the identical computational domain, which has a converging and diverging section to induce local pressure gradient. After this section, the FSTI is found to have decreased and is measured again before the boundary layer separation location in all cases. The new measurements of FSTI are 0.0%, 2.1%, 2.5%, and 4.0%, respectively, for Case-0.0, Case-3.0, Case-4.7, and Case-8.0. When FSTI is increased, the separation bubble sizes, both length and thickness, are reduced. The separation location moves towards downstream while the reattachment location moves towards upstream, resulting in a separation bubble with shorter length in the higher FSTI case. The change of separation bubble thickness follows a similar pattern in which thickness is reduced when FSTI is increased. However, the relationship between FSTI and separation bubble thickness is found to be non-linear. The separation bubble thickness is more sensitive to switching FSTI on and off, for example, greater reduction in the bubble thickness when FSTI is increased from 0.0% to 3.0% than when FSTI increased from 3.0% to 8.0%. Apart from the bubble characteristics, the transition onset location is also found moving upstream, associated with a shorter separated shear layer when FSTI is increased.

Even in Case-8.0, with 8.0% and 4.0% FSTI, respectively measured at the flat plate leading edge and before the boundary layer separation, a separation bubble exists with the shortest separated shear layer and the highest value of the minimum negative wall shear stress (weakest vortex shedding) among all cases under investigation. After studying the maximum RMS velocities, turbulence spot formation and bypass transition are ruled out in the two higher FSTI cases (Case-4.7 and Case-8.0). Bypass transition can have a different definition in different transition scenarios. Currently, it refers to early transition before boundary layer separation with the dominant instability mechanism, such as K-H instability and associated vortex shedding activity, being bypassed due to the formation of turbulence spot. With further investigation of the two-dimensional flow structures at mid-span, vortex shedding activities associated with K-H instability are confirmed in both higher FSTI cases (Case-4.7 and Case-8.0). This indicates that K-H instability indeed exists in these cases. The transition onset in these cases is considered to be caused

by multiple transition mechanisms, such as streak instability and K-H instability. The transition onset is predominantly caused by the streak instability in all elevated FST cases under investigation.

Chapter 6

Proper Orthogonal Decomposition (POD) Analysis of Separated-flow Transition

6.1 Introduction

With elevated FST, streaks are found to exist inside the boundary layer even after the time-mean separation location in the current separated-flow transition. They not only disturb the normal K-H wave in the separated shear layer, but interaction between streaks also introduces significant disturbance into the boundary layer. The instability introduced by streak interaction coexists with K-H instability. As summarised in Chapter 4, both these instability mechanisms are at work, leading to the transition onset. Nevertheless, the detailed transition mechanism with multiple instabilities is not understood, for example, the contribution from the streak interactions to the overall energy level during transition has not been established. Therefore, Proper Orthogonal Decomposition (POD) has been employed here to provide insight into this aspect. Additionally, energy decomposition from different POD modes could provide key evidence regarding the dominant mechanism responsible for triggering the transition in the 3%-FST case.

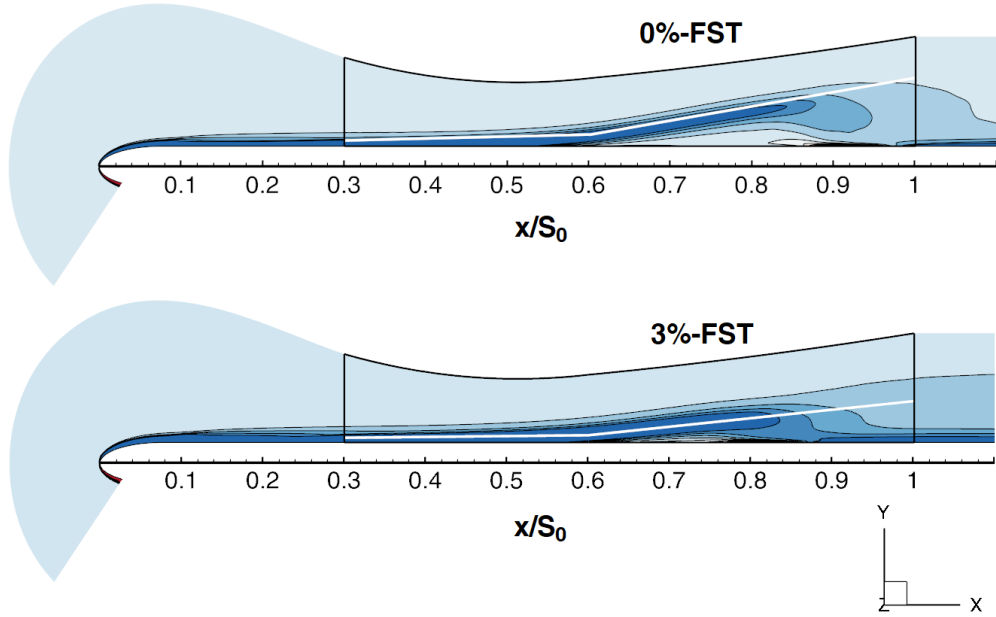


Figure 6.1: Sampling plane locations in the POD analyses. The displayed flow field is within the first layer of blocks next to the flat plate surface, not the entire computational domain. White line: Constant spanned xz -plane. Black line: Enclosing the area of a xy -plane; Line contour: temporal averaged span-wise vorticity field.

6.2 POD Analysis Sampling Locations

Currently, POD has been computed in both cases with 0% FST and 3% FST. Respectively, these two cases are selected to provide a direct comparison between separated-flow transition without and with the influence from FST, The 3%-FST case has the lowest intensity of FST among all calculated cases, also, its results were validated against available experimental data and showing favourable agreement. POD analyses have been carried out on two-dimensional cut-planes extracted from the LES flow field. These include a single xz -plane and different number of xy -planes in each case. The xz -plane in both cases has been configured such that it aligns with the time-mean shear layer. As shown in Figure 6.1, the temporal averaged span-wise vorticity field has been used to visualise the shear layer. The xz -plane, represented by a white-line, is configured close to the shear layer centre line in both cases. Three xy -planes (an area covered by black lines) have been analysed in the 3%-FST case, and are located at the computational domain mid-span ($0.5z$), left-quarter-span ($0.25z$), and right-quarter-span ($0.75z$). In contrast, only one xy -plane at the mid-span has been analysed in the 0%-FST case, with its transition process

known to be two-dimensional. Although POD in xz -plane and xy -plane are calculated independently, the POD results are correlated to each other, therefore, the total number of xy -planes is considered sufficient for the current analyses.

6.3 POD Results

6.3.1 POD Results - 0%-FST Case

Results on xz -Plane

In the 0%-FST case, POD contours of the stream-wise velocity fluctuation, u' , in the xz -plane are shown in Figure 6.3, which contains the first 10 proper orthogonal modes. The contour levels here represent the averaged modal energy contribution, \widetilde{U}_s , which is defined in Equ. 6.1. In this equation, $\widetilde{U}_{sk}(t)$, is the modal energy contribution at a temporal-mode, t , and, N_t , is the total number of temporal-modes.

$$\widetilde{U}_s = \sum_{t=1}^{N_t} \widetilde{U}_{sk}(t)/N_t \quad (6.1)$$

The energy distribution of these 10 POD modes is also computed. As discussed previously, the energy distribution is defined as the ratio between the current eigenvalue and the summation of eigenvalues from all the proper orthogonal modes, written as $\lambda_i/\sum \lambda_k$. As shown in Figure 6.2, the first POD mode (Mode-1) contributes about 60% of the total kinetic energy, and Mode-2 to Mode-4 have contributed a total of 10%. The rest of the modes (Mode-5 to Mode-10) individually contribute less than 2.5%, which can be reasonably disregarded from the analyses. The overall contribution of the first 10 POD modes is about 80% of the total kinetic energy.

This also implies that only a few of the most energised low-order modes is sufficient to properly represent the overall energy structure as found in Figure 6.3. Notably, the first four modes are the most energised modes in this case. Upon further investigating flow structures in these low-order modes, distinct cross-span structures are identified. Their contour levels alternate between correlation ($+\widetilde{U}_s$) and anti-correlation ($-\widetilde{U}_s$). These energy structures with alternating correlation levels are prompted by the cross-span K-H rollers (shown in Figure 4.19, Tu=0%). More specifically, Mode-1 has captured coherent structures that have the highest energy level, such as the secondary instability and the shear layer breakdown process related to the K-H instability. Near $x/S_0 = 0.9$, cross-span

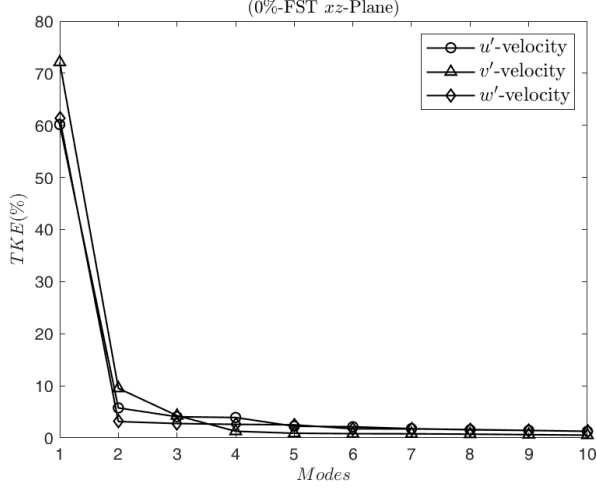


Figure 6.2: Energy distribution of the first 10 POD modes from the xz -plane flow field (0%-FST case).

strips are believed to correspond to the K-H billows in the secondary instability stage. This K-H billow is a cross-span three-dimensional structure formed during the initial breakdown stage of the two-dimensional K-H roller. An example of this three-dimensional structure can be found in Figure 4.19, $Tu=0\%$, at $x/S_0 = 0.9$. Additionally, high energy spots (red) alongside this cross-span strips ($x/S_0 > 0.95$) are related to the vortex breakdown, where shear layer roll-up has gradually evolved into three-dimensional vortices before the fully turbulent boundary layer. Due to the primary K-H instability being less energised, it is predominantly captured by the second POD mode. As a result, the high energy structures in Mode-2 are more organised span-wise strips that link to the full-span K-H rollers. The flow structures in the high-order modes are mostly small localised stochastic structures during the transition and breakdown process, which have relatively low energy levels.

The power spectral density (PSD) results of the corresponding time-coefficient (shown in Figure 6.4) support the existence of the K-H instability. A distinct frequency peak of 25.34Hz appears in the four most energised modes. This frequency agrees strongly with the instability analysis result in Table 4.3 ($x/S_0 = 0.84$ in the 0%-FST case). With such a frequency peak, the separated shear layer is considered unstable to K-H instability. Nevertheless, this peak in the first mode has the lowest energy level among the first four POD modes. This supports the observation that the primary K-H instability has been predominantly captured by Mode-2. The same frequency peak can also be identified from the PSD of other variables (velocities and pressure). This frequency peak has become

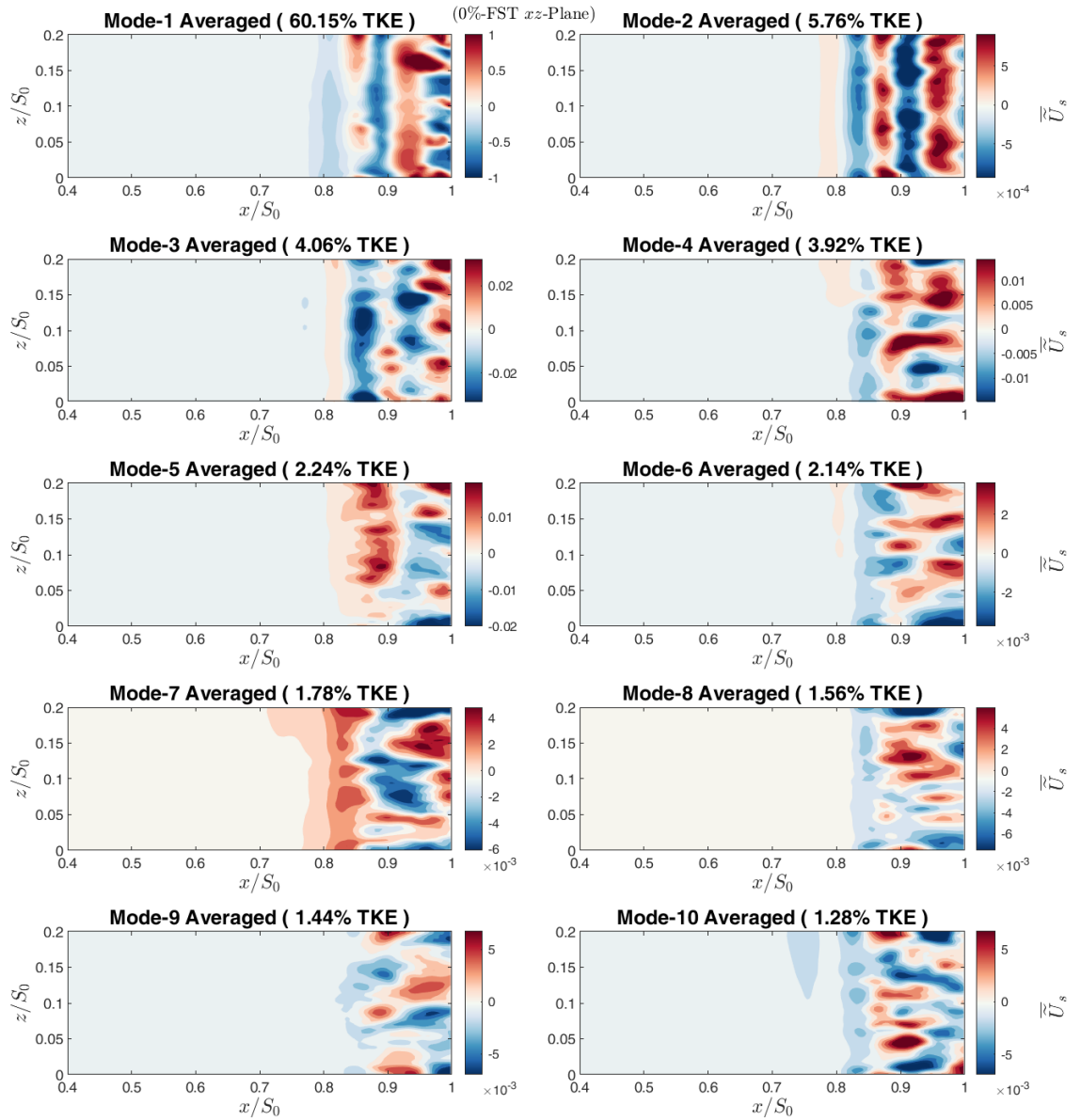


Figure 6.3: POD contour of the u' -velocity from the xz -plane flow field (0%-FST case).

vague in Mode-6 and in other higher order POD modes (not shown). In line with the finding from the previous chapter, the K-H instability indeed exists in the 0%-FST case.

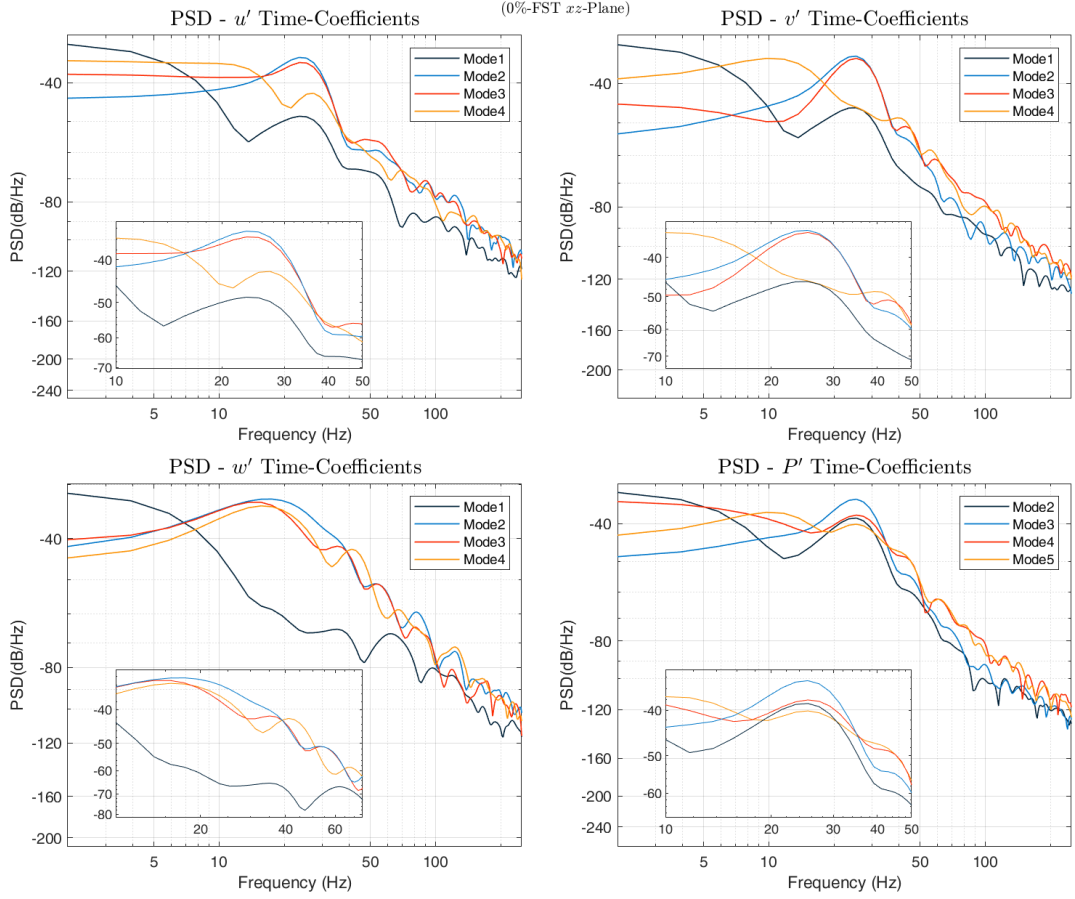


Figure 6.4: Time-coefficient PSD of the xz -plane flow field (0%-FST case).

Results on xy -Plane

In the xy -plane, the POD analysis of the u' -velocity field shows a similar scenario as the previous xz -plane, where the K-H instability is the dominant transition mechanism. As shown in Figure 6.5, the main energy contributions from the primary K-H instability have been captured by the second mode, Mode-2. This contributes approximately 8.4% of the total kinetic energy. Whereas the first mode, Mode-1, has captured the most energised structures in the secondary instability and the shear layer breakdown stage and contributes about 71% of the total kinetic energy.

In Mode-2 and Mode-3 of Figure 6.6, energy structures correlated to the vortex shedding can be clearly observed onward of $x/S_0 = 0.8$. From Figure 6.7, a frequency peak (26.31Hz) also exists in the current time-coefficient PSD. The energy levels of this frequency peak are -42dB, -27.5dB, and -29dB respectively in Mode-1, Mode-2, and Mode-3. This frequency peak (26.31Hz) is again within the frequency range of, $0 < f < 26.99(Hz)$ (in Table 4.3, 0%-FST, $x/S_0 = 0.78$), which the separated shear layer is considered unsta-

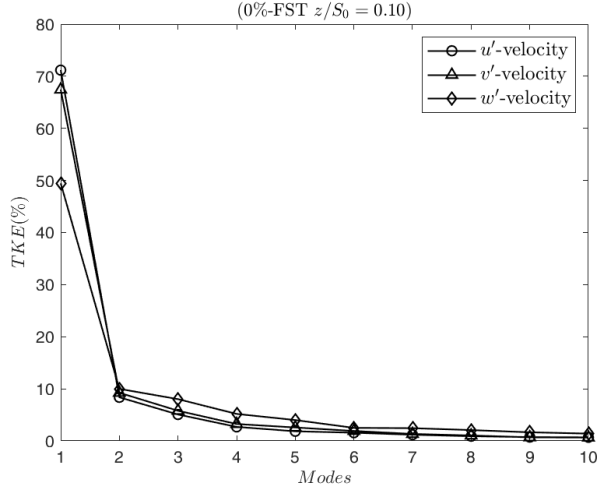


Figure 6.5: Energy distribution of the first 10 POD modes from the mid-span xy -plane flow field ($z/S_0 = 0.10$, 0%-FST case).

ble to K-H instability. An identical frequency peak can also be detected in the v' -velocity and the pressure field PSD. This again supports the previous observation in the xz -plane that the primary K-H instability indeed exists in the current case, and it is the dominant instability mechanism leading to the transition process. This frequency peak (26.31Hz) has the highest energy levels in Mode-2, which also supports the observation that the K-H instability is predominantly captured by this mode.

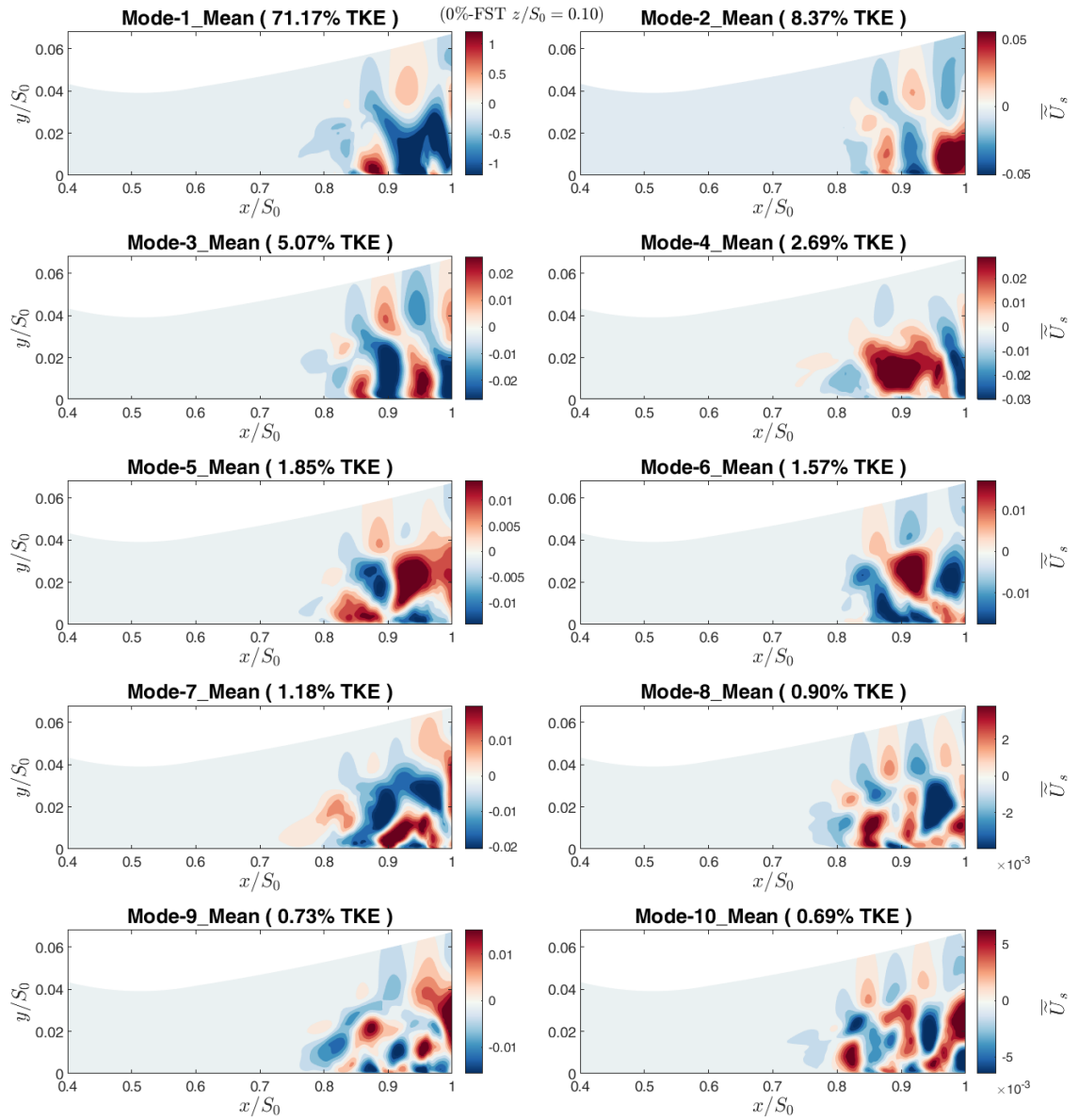


Figure 6.6: POD contour of the u' -velocity from the mid-span xy -plane flow field ($z/S_0 = 0.10$ 0%-FST case).

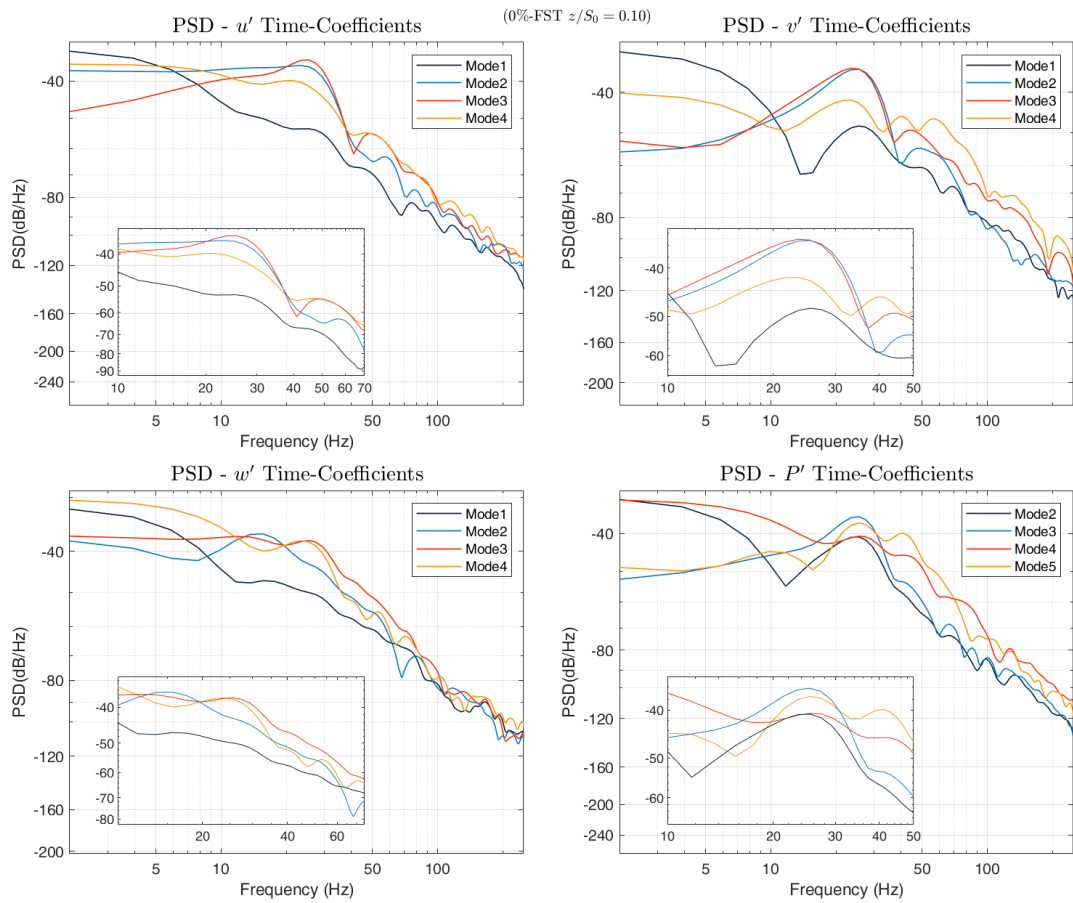


Figure 6.7: Time-coefficient PSD of the mid-span xy -plane flow field ($z/S_0 = 0.10$, 0%-FST case).

6.3.2 POD Results - 3%-FST Case

Results on xz -Plane

Results from the POD analysis in the 3%-FST case are investigated here. In total, 20 proper orthogonal modes of three velocity components and one pressure component were computed. Contour plots of the first 10 POD modes of the stream-wise velocity component are shown in Figure 6.8 and can be compared with results from the 0%-FST case.

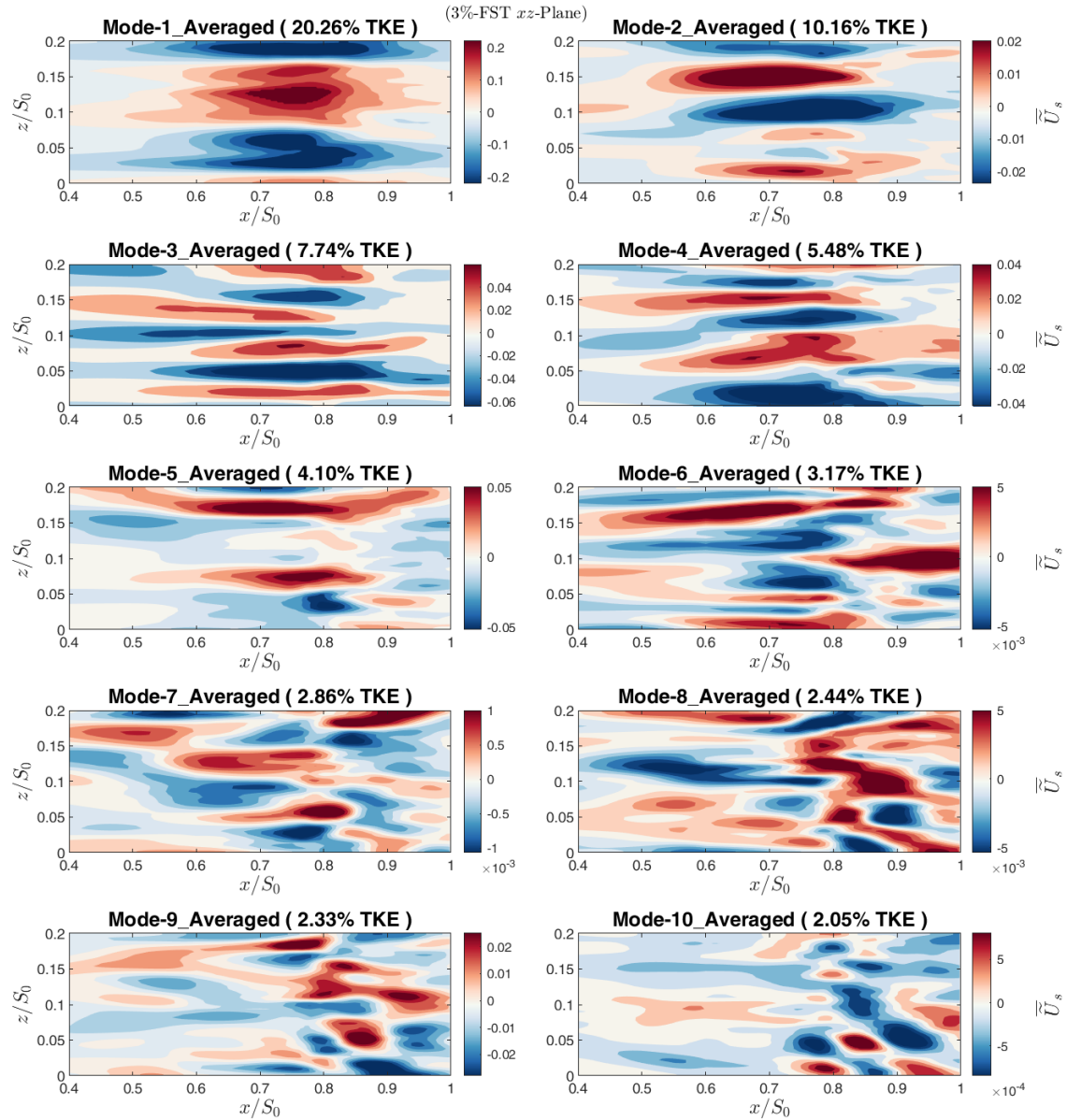


Figure 6.8: POD contour of the u' -velocity from the xz -plane flow field (3%-FST case).

High energy regions with streaky appearance are found in the entire xz -plan in all

computed modes. These streaky structures correlate to boundary layer streaks in the actual flow field. Conversely, in the 0%-FST case, the boundary layer before the transition-onset location (between $x/S_0 = 0.40$ to $x/S_0 = 0.82$) is free from disturbance. Streaky structures in the 3%-FST case have very high energy content within the entire separation bubble between $z/S_0 = 0.62$ and $x/S_0 = 0.87$, represented by the most saturated colour. In contrast to the 0%-FST case, high energy structures are observed on $x/S_0 = 0.82$ and at the downstream location. In the 3%-FST case, the streaky instability structures found within the entire separation bubble are caused by boundary layer streak interactions. Whereas in the 0%-FST case, stream-wise unsteadiness only develops at the transition onset location at $x/S_0 = 0.82$ and is caused by inviscid K-H instability. It is worth noting that the present analysis focuses only on the stream-wise velocity component. A different scenario does exist in other components.

POD energy distribution of the u' -velocity is also remarkably different in the two FST cases. In the current 3%-FST case, as shown in Figure 6.9, the primary mode only contributes slightly more than 20% of the total kinetic energy, and Mode-2 to Mode-10 contribute between 10% to 2%. The rest of the modes individually contribute less than 2% of the total kinetic energy. In the 0%-FST case, the first mode alone contributes the greatest amount of energy (60%). In contrast, 60% of the total kinetic energy is contributed by the first 10 modes in the 3%-FST case. There is about 44% of the total kinetic energy contributed by Mode-1 to Mode-4 in the 3%-FST case. Boundary layer streaks are clearly to be the most energetic elements in these modes. It is reasonable to believe that streak instability is the dominant mechanism leading to transition.

The time-coefficient PSD of the current xz -plane flow field is investigated here. As the u' -velocity PSD shown in Figure 6.10, it does not contain any high energy frequency peaks in all displayed modes. Instead, a variety of low energy frequency peaks can be identified. Conversely, distinct frequency peaks can be identified in both PSD of v' -velocity and w' -velocity. In the v' -velocity PSD, both Mode-1 and Mode-2 have two distinct frequency peaks of 23.45Hz and 31.25Hz, whereas, Mode-3 and Mode-4 both have another two frequency peaks of 23.45Hz and 35Hz. A similar pattern can be found in the PSD of w' -velocity. Mode-1 and Mode-2 have two identical frequency peaks, and Mode-3 and Mode-4 have another two similar frequency peaks. The existence of two sets of frequency peaks reveals a possibility that different transition activities are captured by

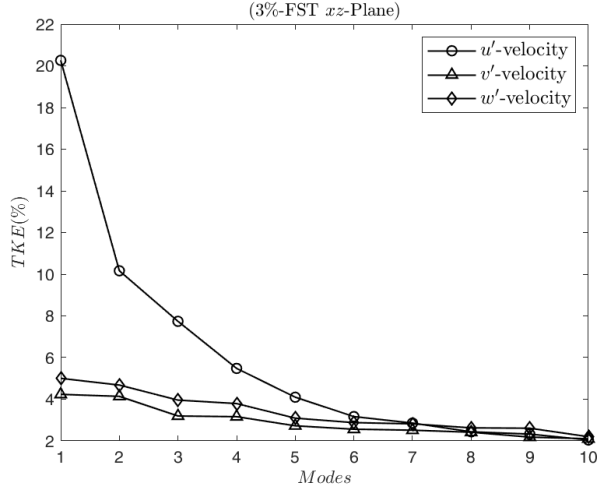


Figure 6.9: Energy distribution of the xz -plane flow field (3%-FST case).

the xz -plane POD analyses.

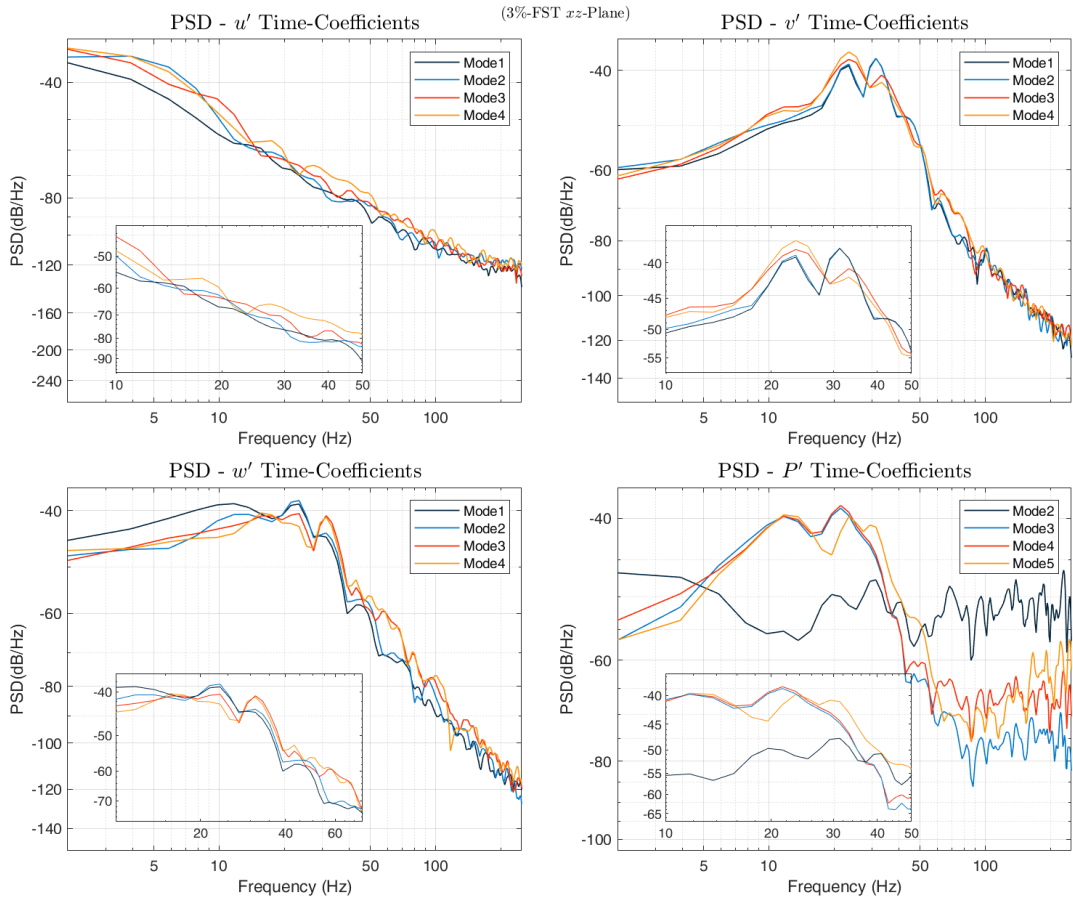


Figure 6.10: Time-coefficient PSDs of the xz -plane flow field (3%-FST case).

After investigation of the v' -velocity POD contour shown in Figure 6.11, different energy structures are identified especially onward of the transition-onset location ($x/S_0 =$

0.75) in Mode-1 to Mode-8. The most energised structures appear as periodic part-span strips. They can be broadly classified into two groups which are longitudinally divided by an imaginary straight line drawn at $z/S_0 \approx 0.08$. Clearly, these two groups of energy structures are linked to the two high energy structures found in Mode-1 of the u' -velocity POD contour. They are considered a result of transition that are triggered by multiple instability mechanisms.

The existence of a multiple instability mechanism is also supported by different energy structures found in the w' -velocity POD contour shown in Figure 6.12. In Mode-1 to Mode-4, two different energy structures can be roughly identified after the transition-onset location ($x/S_0 = 0.75$). Energy structures with larger and stronger scale structures are observed in the lower section (between $z/S_0 = 0.00$ and $z/S_0 = 0.08$) of the frame, and smaller and weaker scale structures are located in the upper section (between $z/S_0 = 0.08$ and $z/S_0 = 0.20$). In the corresponding time-coefficient PSD, multiple distinct frequency peaks can also be identified in all modes shown. The two distinct frequency peaks (23.45Hz and 31.25Hz) found in the v' -velocity also exist here.

In Figure 6.13, the POD results from the fluctuating pressure field also agree with the established observations from the v' and w' velocity fields, which multiple instability mechanisms are observed. In Mode-5 and Mode-6, two energy structures can be distinguished by two groups of periodic structures that are separated at approximately $z/S_0 = 0.08$. In the rest of the modes, especially in Mode-3 and Mode-4, as well as in Mode-7 and Mode-8, one of the two energy structures can be clearly observed dominated, and it is located at the lower section of the frame (between $z/S_0 = 0.00$ and $z/S_0 = 0.08$). Upon investigating the pressure field PSD, two frequency peaks of 13.67Hz and 23.45Hz exist.

In this investigation of the xz -Plane POD results, streaky energy structures dominate in all modes of u' -velocity POD contours in Figure 6.8. In contrast, distinct part-span energy structures exist in Mode-1 to Mode-4 of the v' -velocity POD contour in Figure 6.11. Similar part-span energy structures also exist in the P' POD contour in Figure 6.13. These part-span energy structures initially appear at the transition onset location at $x/S_0 = 0.75$. The appearance of these part-span energy structures is similar to those from K-H instability in Figure 6.3 apart from them being slightly distorted. In the time-coefficient PSD of the v' -velocity component, a distinct frequency peak of 23.45Hz satisfies the K-H instability criterion. As a result, the part-span energy structure is indeed a representation

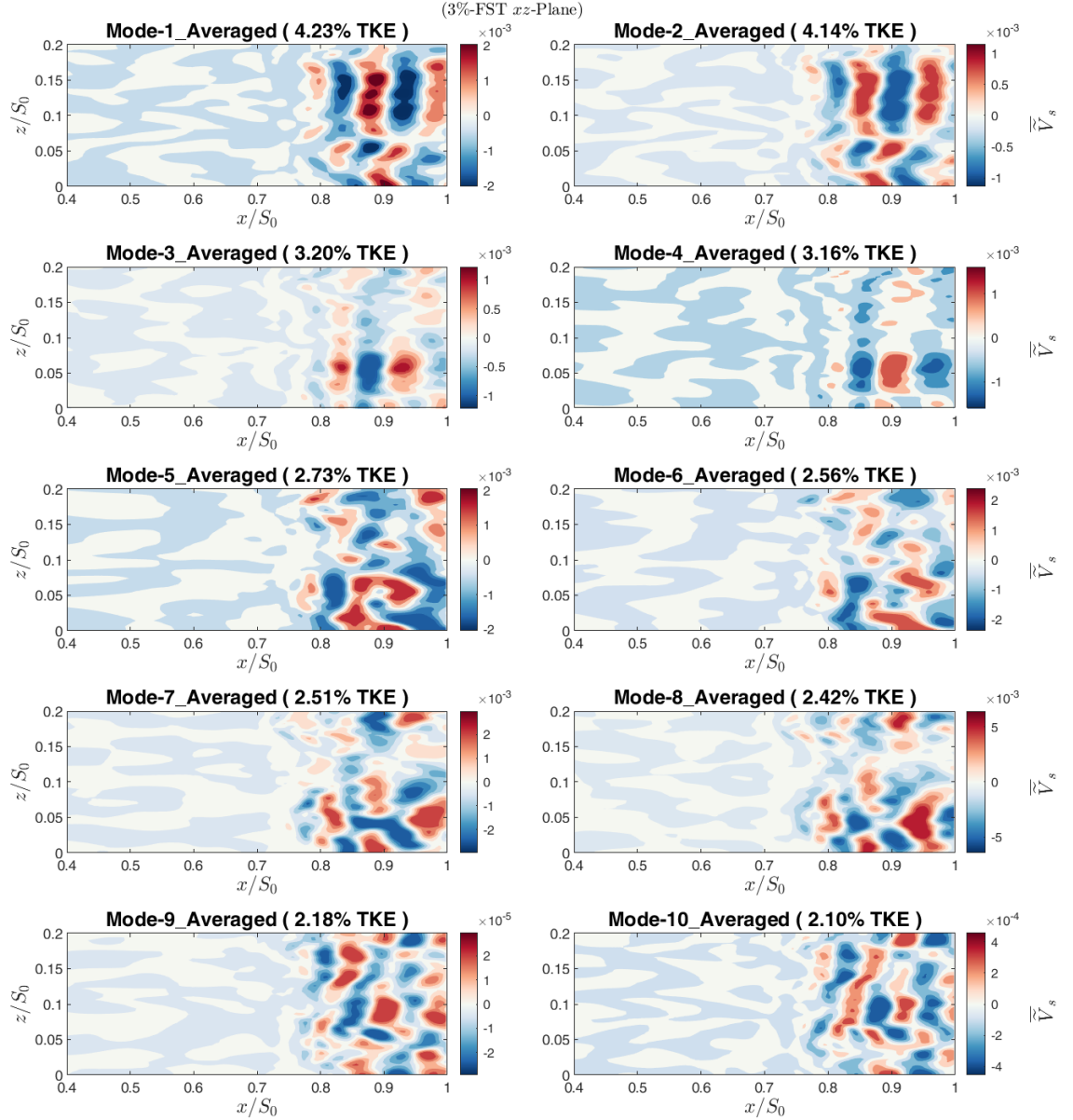


Figure 6.11: POD contour of the v' -velocity from the xz -plane flow field (3%-FST case).

of the part-span K-H rollers. Also, the existence of part-span K-H instability can be confirmed in the current 3.0%-FST case. When comparing the scale in both u' -velocity and v' -velocity POD contour, the former scale is an order of magnitude greater than the latter one. This is because that the former POD contour represents the streak instability and it is considered more dominant in the current transition process under 3.0% FST.

As the boundary layer streaks are a result of stream-wise velocity variation, they are primarily detected by the u' -velocity POD analysis. The part-span K-H roller contains stream-wise and wall-normal velocity variations, as well as pressure fluctuation. But its

stream-wise variation is too weak compared with those from the streak instability. As a result, it does not appear in the u' -velocity POD contour. Nevertheless, the K-H roller has a distinct footprint in the v' -velocity and P' POD contour. This implies that the u' -velocity POD analysis can be used to detect streak instability and the v' -velocity and P' POD analysis can be used to detect K-H instability. This provides a plausible explanation for the fact that no K-H related energy structure were detected in the u' -velocity POD analysis by [Hosseinverdi and Fasel \(2018\)](#). The current finding suggests that both the v' -velocity component and the P' pressure component should be examined along with the u' -velocity component when conducting a POD analysis in separated-flow transition.

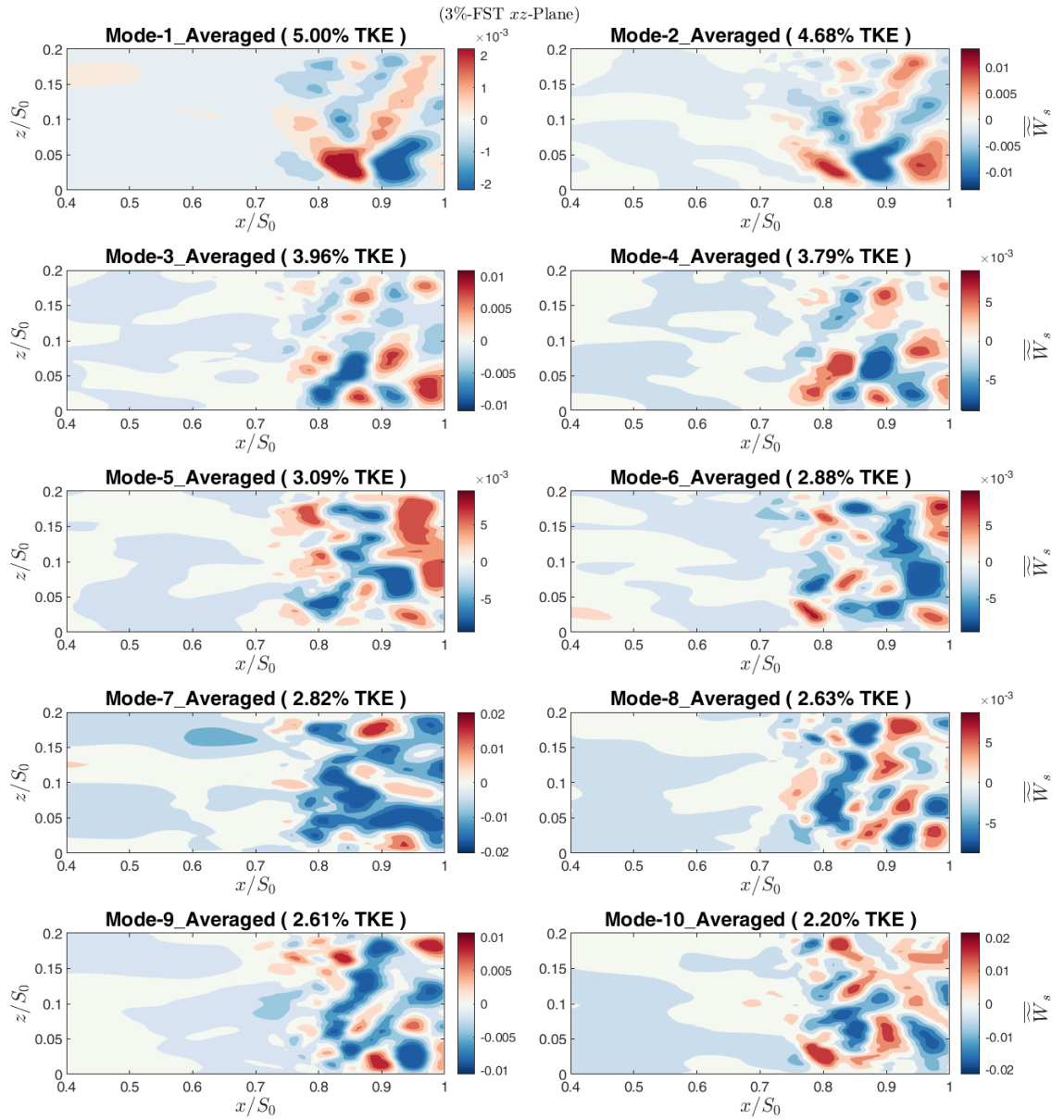


Figure 6.12: POD contour of the w' -velocity from the xz -plane flow field (3%-FST case).

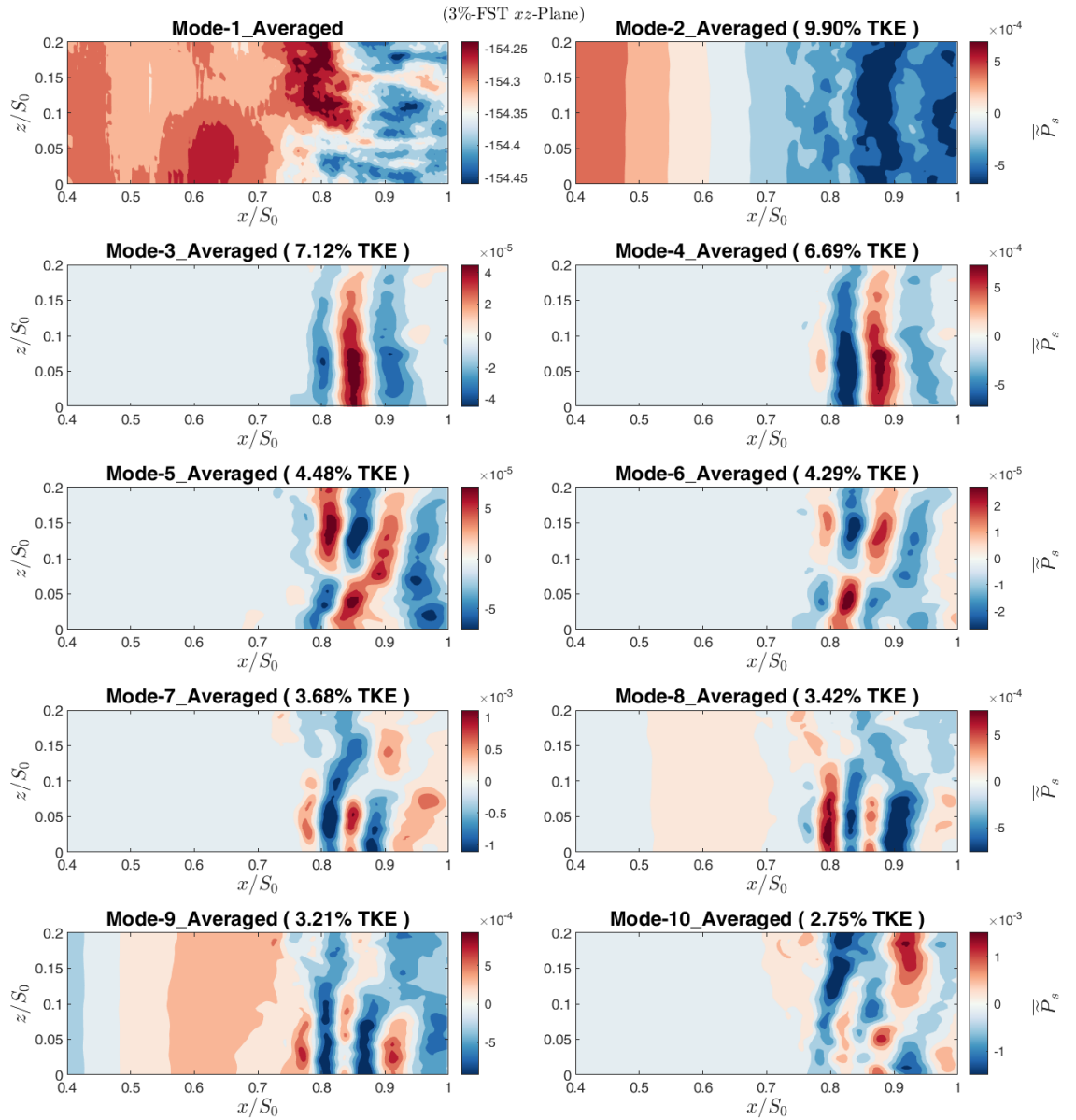


Figure 6.13: POD contour of the pressure fluctuation from the xz -plane flow field. Mode-1 of the pressure fluctuation POD contour has predominantly captured the global pressure fluctuation due to the mass flow imbalances between the upper and the lower passage of the computational domain. As a result, its energy contribution has not been accounted for in the energy distribution calculation (3%-FST case).

Results on xy -Plane ($z/S_0 = 0.10$)

POD results from the xy -planes flow field are investigated here. In total, POD in three xy -planes have been computed and investigated, located at $z/S_0 = 0.5$, $z/S_0 = 1.0$, and $z/S_0 = 1.5$. In the xy -plane at $z/S_0 = 1.0$ (mid-span), the POD energy distribution has a similar pattern to the energy distribution in the previous xz -plane. As shown in Figure 6.14, the first POD mode has contributed a relatively large portion of the kinetic energy in the current xy -plane, which is about 35% of the total kinetic energy. However, this is still less than half the amount (71%) in the 0%-FST case. The current energy contribution from Mode-2 to Mode-9 is between 11.6% and 2.0%, and the rest of the POD modes individually contribute less than 2% of the total kinetic energy. Clearly, more energy contributions come from the high-order modes (Mode-2 onwards). In total, these high-order modes have contributed about two thirds of the total kinetic energy rather than one third as in the 0%-FST case. Such energy distribution indicates that unsteadiness has been scattered into high-order modes. This also suggests that more lower order modes are required to represent the current flow field with 3.0%-FST.

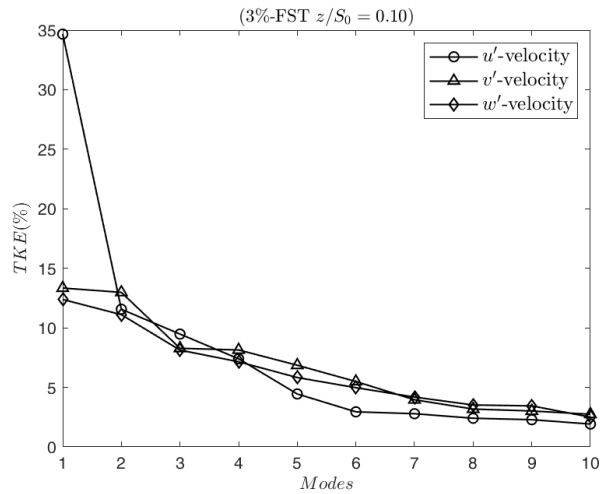


Figure 6.14: Energy distribution of the mid-span xy -plane flow field ($z/S_0 = 0.10$).

Figure 6.15 shows the xy -Plane flow field ($z/S_0 = 0.10$) POD contour that consists of the first 10 POD modes. In the most energised mode, Mode-1, a correlated region can be identified with a sharp leading edge and a blunt trailing edge that is tilting slightly downwards. This region exists between $x/S_0 \approx 0.51$ to $x/S_0 \approx 0.97$, and its appearance is similar to the time-mean separation bubble. Its shape and location is reminiscent of the highly unsteady structure found in the RMS stream-wise velocity, $\sqrt{u'u'}$, contour (not

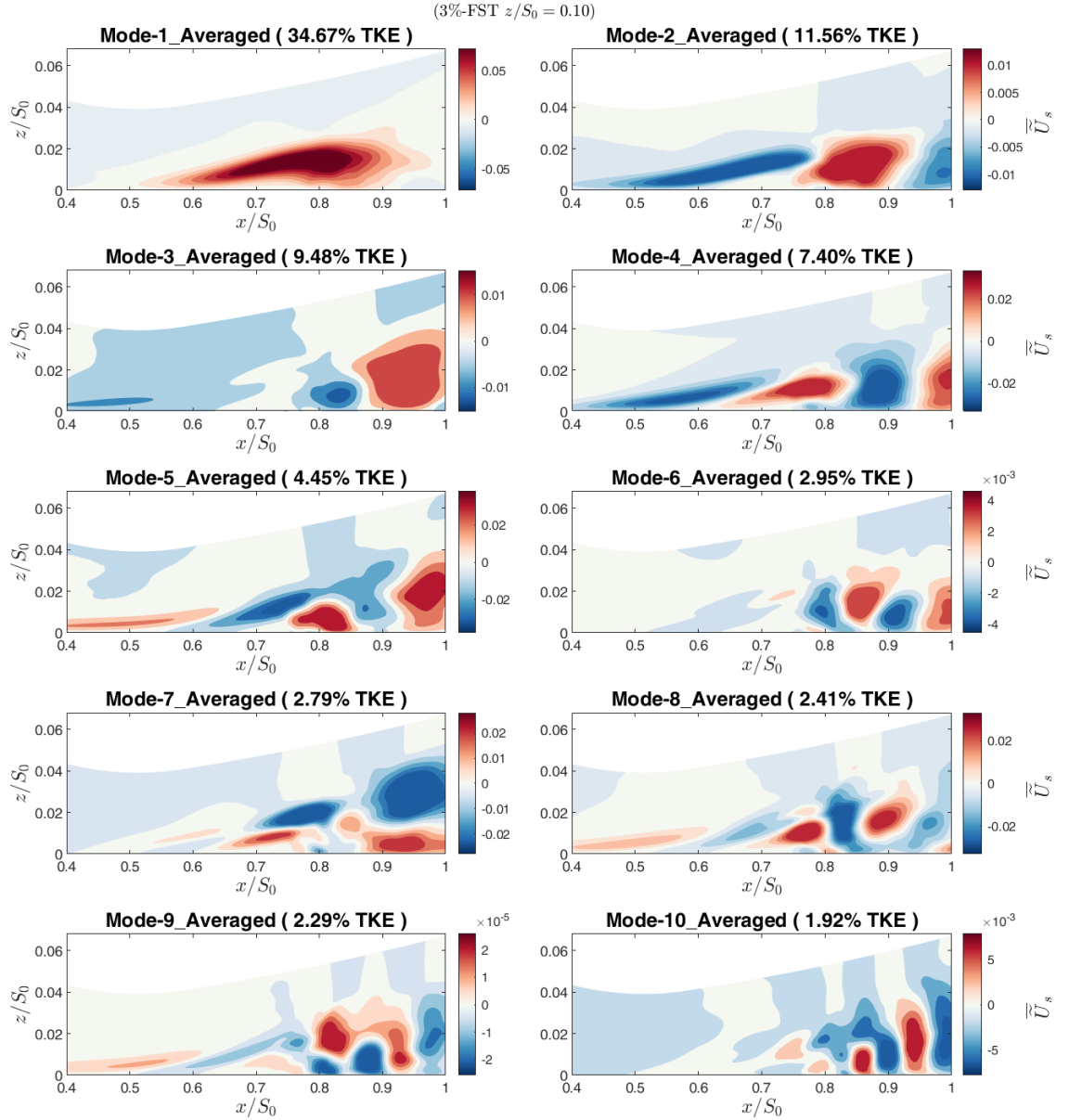


Figure 6.15: POD contour of the u' -velocity from the mid-span xy -plane flow field ($z/S_0 = 0.10$).

shown). A region with a similar shape exists at the similar location, and the velocity fluctuation is highest in the entire contour plot. In the actual flow field, this region is where the separated shear layer, transition, and breakdown activities occur.

In addition, the downward tilting trailing edge of the correlated region indicates that most streak interactions crossing the current xy -plane, as well as the transition processes, are happening close to the flat plate surface. As a result, a high level of kinetic energy is concentrated closer to the plate surface to form a downward tilting tail. Instability caused

by such streak interaction is known as the inner mode streak instability. This is similar to the inner mode streak instability in bypass transition, which is caused by near wall inflection points in the velocity profile (Zaki (2011) and Vaughan and Zaki (2011)). In Mode-2 to Mode-6 of the POD contour, a train of vortical structures with alternating zones of correlation and anti-correlation appear onward of the transition-onset location at $x/S_0 = 0.75$. These vortical energy structures are in contact with the plate surface, and their circular appearance is flattening at the lower edge. This also indicates that the current transition process and vortex shedding are happening close to the surface. Consequently, the corresponding streak instability can again be confirmed to happen through the inner mode. This mode of streak instability is caused by an interaction between a high-speed streak and a low-speed streak or stationary fluid at the inner part of the separation bubble. Also, the positive correlation level of the entire unsteady event is mainly caused by a high-speed streak entering the separation bubble and triggering the transition event.

The increased streak instability is caused by streak collisions in the separated shear layer. When a streak enters the free shear layer, it tends to collide with another streak. The collision is mainly caused by the deceleration and lift-up of the former streak where the separation bubble is thickened as a result of the local adverse pressure gradient. The latter streak enters the free shear layer at a constant velocity and collides with the former one. After the collision, the latter streak is decelerated and lifted again to cause further collision with an upcoming streak. Therefore, the related streaky energy structures in Mode-2 to Mode-5 is alternating between correlation or anti-correlation and stack up together in the separated shear layer. Similar streaky energy structures are also found in high-order modes which represent the accumulation of kinetic energy from streak interactions of less energised streaks. As a result, such unsteadiness has not been further amplified and has not developed into streak instability or even transition.

When investigating the current time-coefficients PSD shown in Figure 6.16, the PSD result in Mode-1 of the u' -velocity has no distinct frequency peak with kinetic energy dissipating exponentially. In other displayed modes (Mode-2 to Mode-4), a frequency peak of 10Hz exist in all these modes. Also, several low-energy frequency peaks exist, however their energy level is too low to be significant. In contrast, a distinct frequency peak with a frequency of 31Hz exists in Mode-1 and Mode-2 of the v' -velocity PSD, followed by a less energised low frequency peak (13Hz). In Mode-3 and Mode-4, the existence of two

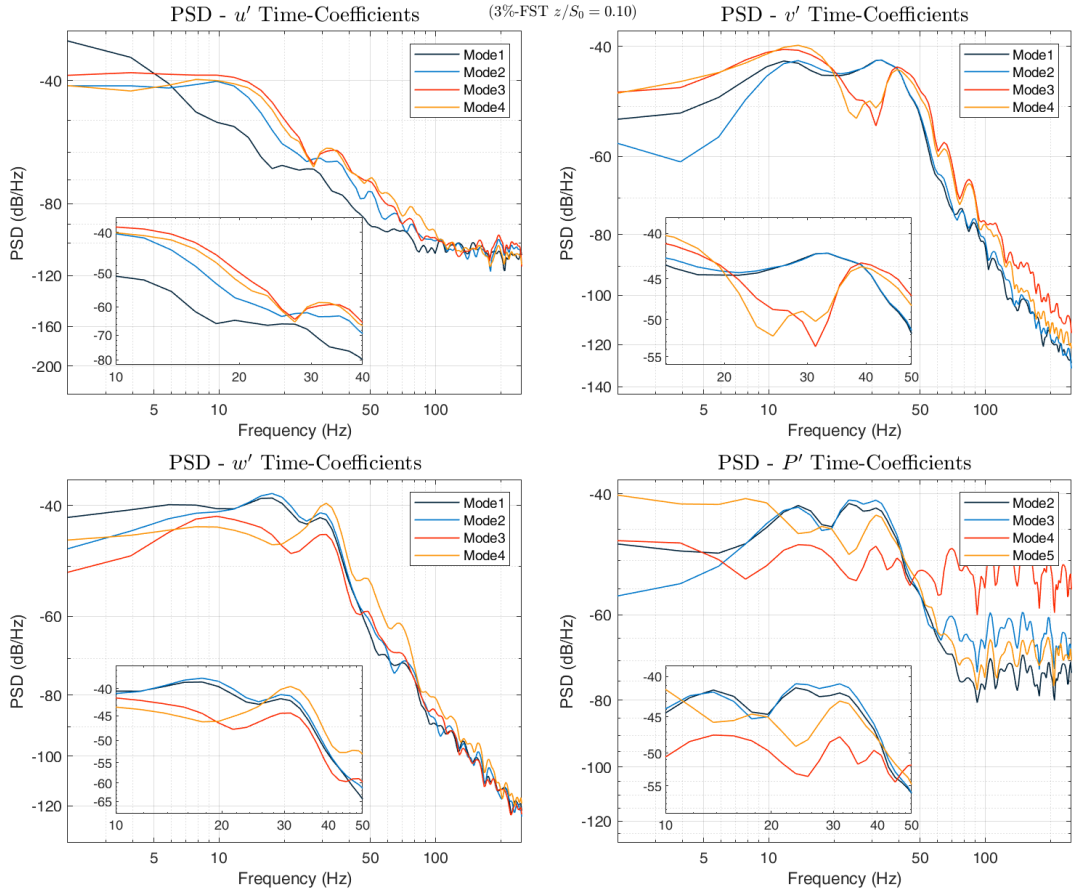


Figure 6.16: Time-coefficient PSDs from the mid-span xy -plane flow field ($z/S_0 = 0.10$).

frequency peaks can also be identified. One frequency peak is 31Hz followed by another less energised frequency peak of 11.72Hz. Likewise, in the w' -velocity PSD, two frequency peaks are found in Mode-1 and Mode-2, and two different frequency peaks are found in Mode-3 and Mode-4. The current frequency peak pattern again reveals that the current transition process is triggered by multiple instability mechanisms. These are most likely to be the two modes of the streak instabilities.

Results on xy -Plane ($z/S_0 = 0.05$)

Due to the localised nature of boundary layer streaks, xy -plane POD analysis in different span-wise locations have different energy contents. The xy -plane at $z/S_0 = 0.5$ is located at the left-quarter-span of the computation domain. Figure 6.17 displays the energy distribution from the current xy -plane POD analysis, which is similar to the mid-span flow field. The most energised mode, Mode-1, has contributed approximately 32% of the total kinetic energy and Mode-2 and Mode-10 have contributed 10.5% and 2.2%. The rest

of the modes have individually contributed less than 2%, therefore they can be reasonably disregarded in the investigation. In the other two velocity fields, the energy distribution decreases linearly from Mode-1 to Mode-10. This is also similar to the previous xy -plane results.

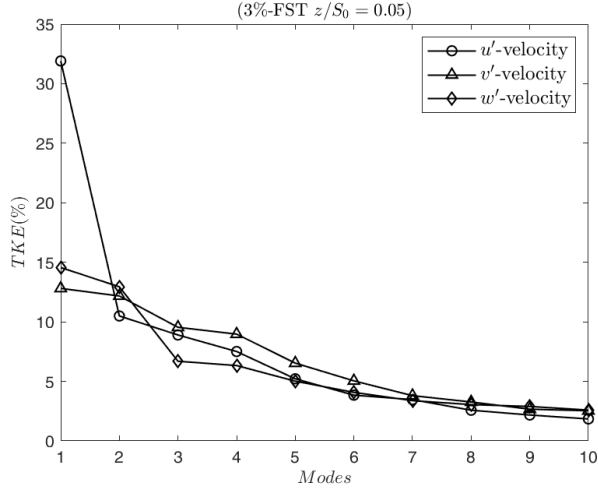


Figure 6.17: Energy distribution of the left-quarter-span xy -plane flow field ($z/S_0 = 0.05$).

Figure 6.18 shows the POD energy contours at the computational domain left-quarter-span ($z/S_0 = 0.05$). In total, 10 POD modes are shown in this figure. In the most energised mode, Mode-1, a region with a high level of anti-correlation can be identified with its appearance and position comparable to the one found in the mid-span. However, some differences appear between the two cases. The trailing edge of the current anti-correlated region is tilting slightly upwards instead of downwards as previously. This is a result of the transition and breakdown process happening further away from the plate surface. More specifically, they are near the boundary layer edge. The corresponding streak instability is via the outer mode streak instability mechanism which is caused by the interaction between a lifted low-speed streak ($-u'$) and the higher speed free-stream fluid. This instability mechanism is found to be comparable to the outer mode streak instability in bypass transition (Zaki (2011), Vaughan and Zaki (2011), Jacobs and Durbin (2001), and Nagarajan et al. (2007)). Empirical observations have shown that the outer mode streak instability is hosted by low-speed streaks in bypass transition. Similarly, a streak instability mechanism through the outer inviscid mode is also reported by Nagarajan et al. (2002).

The existence of outer mode streak instabilities is also supported by streaky energy

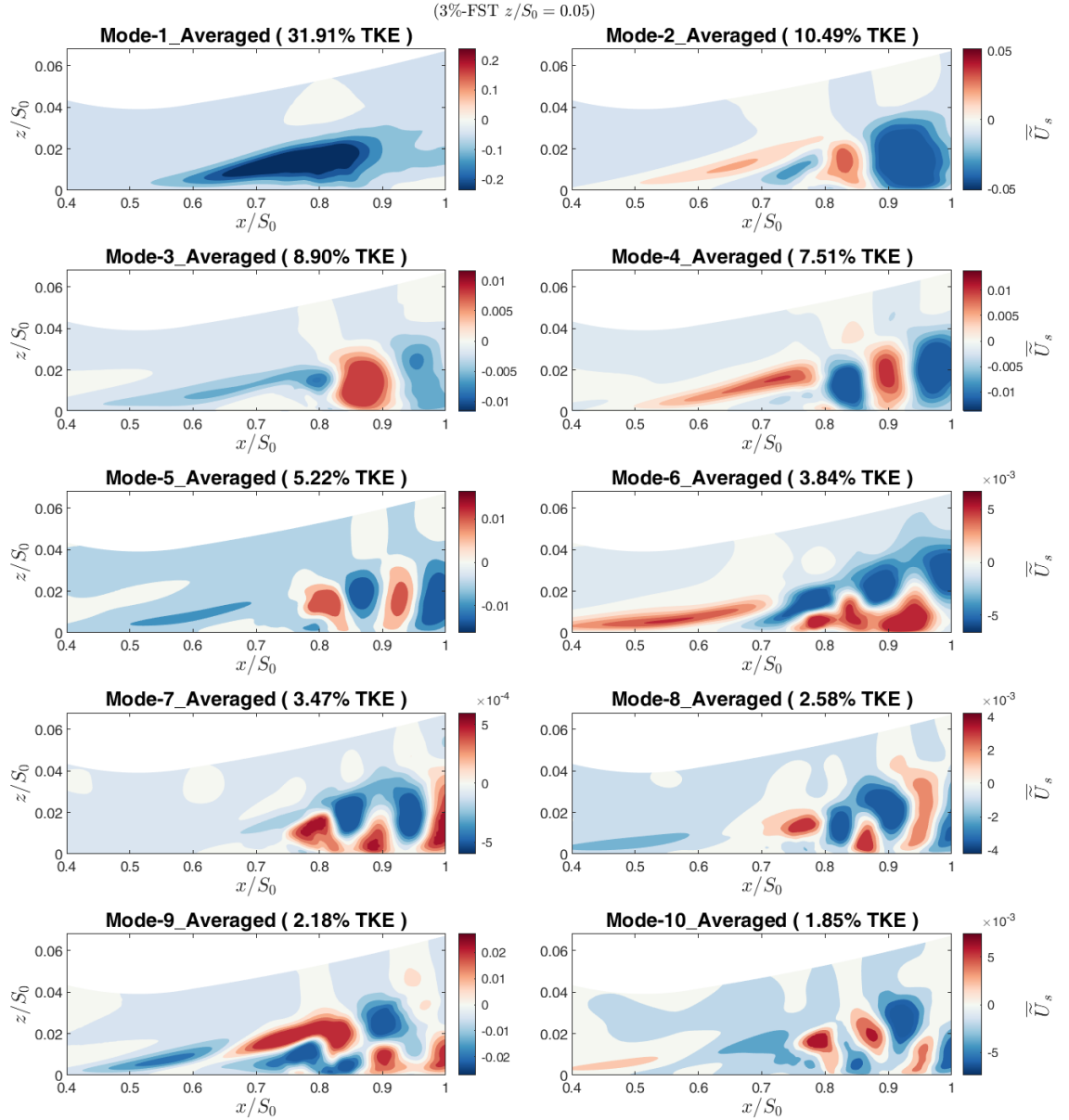


Figure 6.18: POD contour of the u' -velocity from the left-quarter-span xy -plane flow field ($z/S_0 = 0.05$).

structures found in the high-order modes. In Mode-2, a thicker free shear layer contains a streaky correlated structure (red), observable at between $x/S_0 = 0.5$ and $x/S_0 = 0.8$. An anti-correlated structure (blue) is entrained underneath the correlated one. This is in contrast with Mode-2 in the previous xy -plane (Figure 6.15), which has only one streaky structure found in the separated shear layer. This indicates that the current outer mode streak instability has led to the thickening of the separated shear layer, and that the transition process happens near the boundary layer edge.

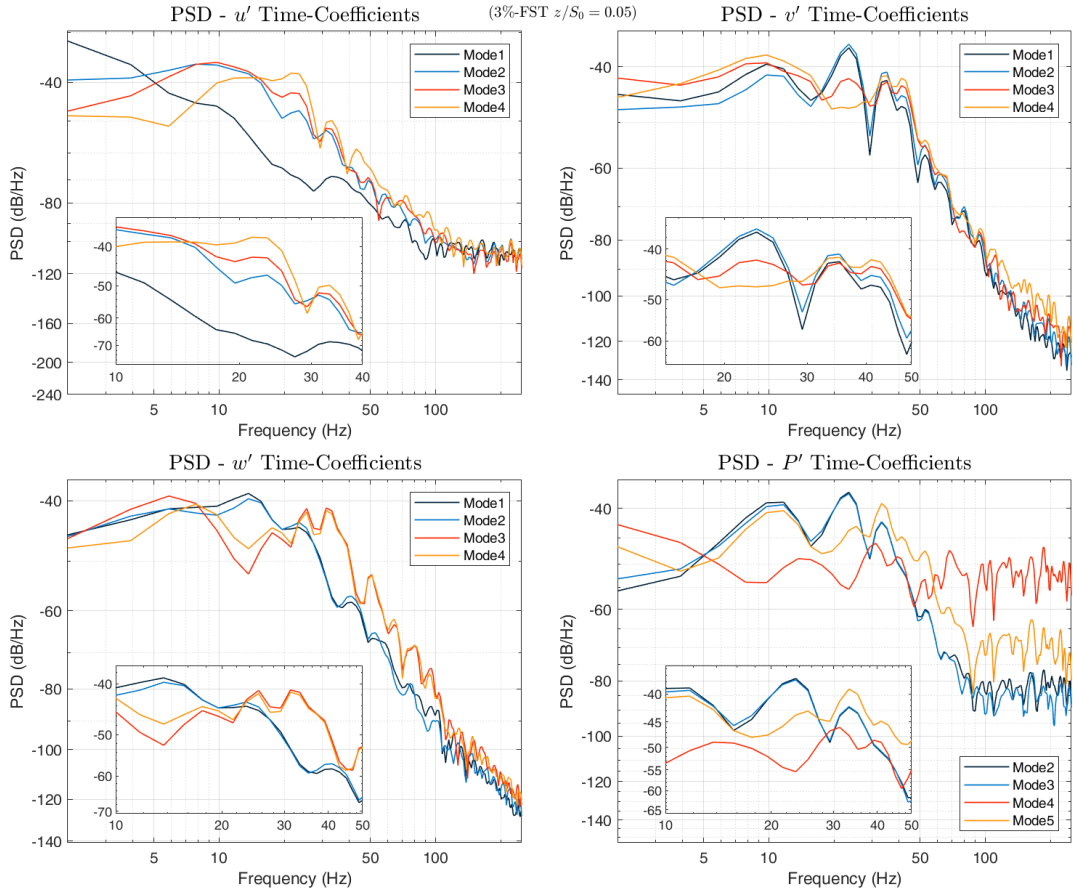


Figure 6.19: Time-coefficient PSDs from the left-quarter-span xy -plane flow field ($z/S_0 = 0.05$).

In Mode-2 to Mode-5, vortical structures with alternating correlation and anti-correlation can be found after the transition-onset location at $x/S_0 = 0.75$. These represent the vortex shedding from the shear layer breakdown process, located near the boundary layer edge. Their shape is of a much finer circular appearance with a lower edge that has not been deformed. Also, in Mode-6 and Mode-7, a train of vortical energy structures in the low-order modes has been reshaped into two layers of vortical structures with identical correlation or anti-correlation in each layer. This is believed to be caused by the current transition process happening away from the plate surface, with sufficient space allowing the outer shear layer to roll into the fluid underneath, resulting in the two-layer energy structures shown. This is also recognised as being a result of the outer mode streak instability, of which this energy structure has not been captured by the previous POD contours at $z/S_0 = 0.10$.

A distinct frequency peak of approximately 23.4Hz exists in Mode-2 to Mode-4 of

the u' -velocity PSD, as shown in Figure 6.19. The energy level of this frequency peak is also quite strong ranging between -37dB and -47dB. An identical frequency peak can also be observed in Mode-1 to Mode-3 of the v' -velocity PSD, as well as in Mode-2 and Mode-3 of the pressure field PSD. This frequency peak is found to be comparable to the frequency peak of 25.34Hz detected in both xz -plane and xy -plane of the 0%-FST case. This peak exists in the PSDs of all variables (u' , v' , w' , and P') and suggests that the transition process here is comparable to the one via the primary K-H instability. The current frequency peak (23.4Hz) is also similar to the u' -velocity frequency peak (24Hz) detected from sampling points immediately after the transition location, as shown in Figure 4.16. Multiple pieces of evidence have suggested that the K-H frequency and the K-H instability indeed exist at the current span-wise location.

Results on xy -Plane ($z/S_0 = 0.15$)

The POD analysis of another xy -plane flow field at the right-quarter-span ($z/S_0 = 0.15$) is also being computed and investigated. In the POD contours shown in Figure 6.20, a region of high energy structure again exists in the primary mode. It is also linked to the transition and breakdown process, as with the other span-wise locations. However, correlation ($+\widetilde{U}_s$) can be observed in this region. This indicates that the transition process is likely to be triggered by high-speed streaks, similar to the xy -plane in the mid-span. Normally, a high-speed streak induces the inner mode streak instability in the separated shear layer, and the transitions process is triggered by the near wall inflection point. In Mode-2 to Mode-4, distinct vortical structures with alternating correlation and anti-correlation can be identified next to the plate surface. This also indicates that the transition process and the free shear layer breakdown in the actual flow field is happening very close to the plate surface. This matches the description of the inner mode streak instability.

The inner mode streak instability is considered to dominate in the current xy -plane flow field, as in the mid-plane flow field ($z/S_0 = 0.10$). This observation is based on results from the POD contour. In Mode-2, mode shapes are comparable to those in Mode-2 of the mid-plane POD contour (Figure 6.15), where the inner mode streak instability has been recognised. However, in Mode-3 and Mode-4, the current mode shapes are very similar to Mode-2 in the left-quarter-span POD contour (Figure 6.18), where the outer mode streak instability has been recognised. Consequently, both mode shapes from the inner and the

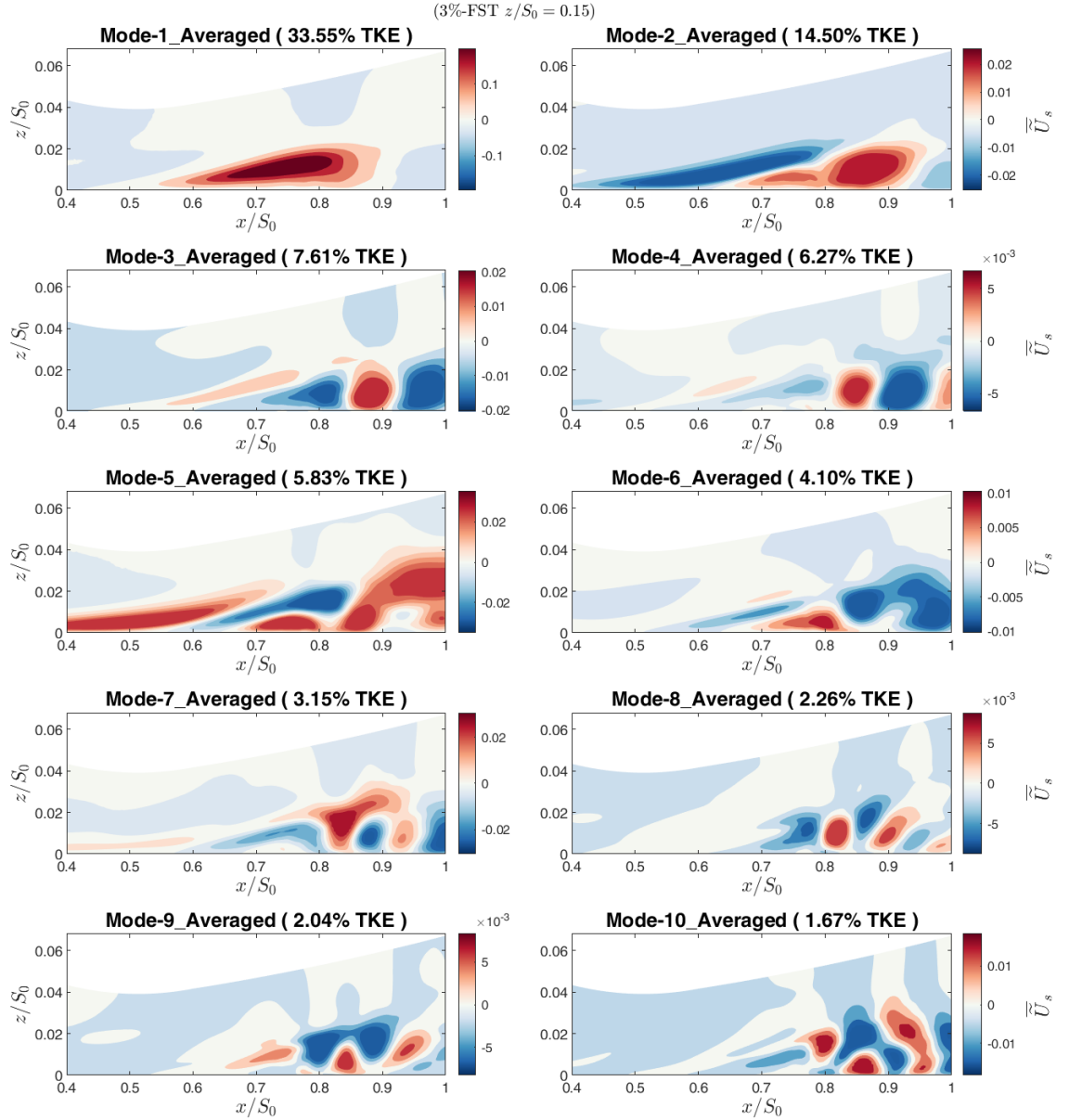


Figure 6.20: POD contour of the u' -velocity from the right-quarter-span xy -plane flow field ($z/S_0 = 0.15$).

outer mode streak instability can be observed in the current POD contour. However, energy structures from the inner mode streak instability in Mode-2 are considered more energised than those from the outer mode in Mode-3 and Mode-4. This supports the observation that the inner mode streak instability dominates in the current xy -plane.

Streak Instability

As discussed previously, the current separated-flow transition has two streak instability modes: outer and inner mode. In the previous POD analyses of the u' -velocity field, evidence has shown that these two streak instabilities have led to different thicknesses of the separated shear layer, and the corresponding transition process also happens in different wall-normal locations. This has also caused vortices that are shaded at different wall-normal locations. More evidence to support this observation can be found in the POD contours of the w' -velocity field. Mode-5 and Mode-6 from the xy -plane POD contours of two span-wise locations are shown in Figure 6.21 and Figure 6.22, respectively, at $z/S_0 = 0.10$ and $z/S_0 = 0.05$.

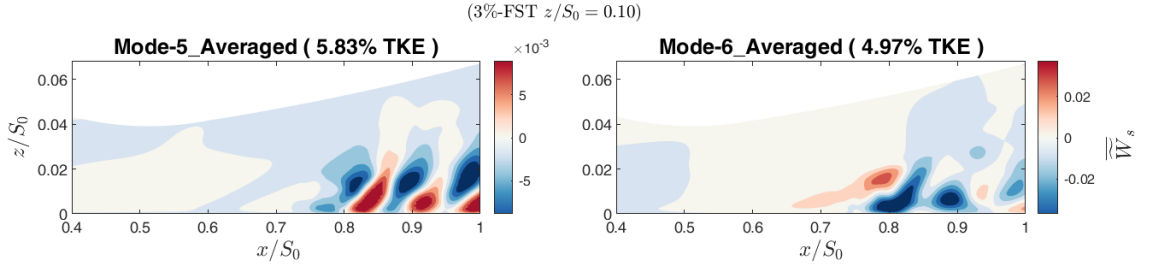


Figure 6.21: POD contour of the w' -velocity field from the left-quarter-span flow field ($z/S_0 = 0.10$).

In these figures, some energy structures with a curved appearance can be identified in both modes. These energised structures are normally observed from $x/S_0 \approx 0.8$ and down-stream locations. When related to the two-dimensional and three-dimensional flow structures in Figure 4.19 and Figure 4.20 in the previous chapter, these locations are where there is the formation of a vortex cascade or a cascade of Hairpin-vortices. As a result, a rapid change in span-wise velocity can be found in the body of these vortices, which leads to the increased w' fluctuation. The rapid changing w' values has been reflected by the POD energy contour, expressed as energised structures with a curved appearance. The height of these structures reflects the height of the Hairpin-vortex and can be used to estimate the boundary layer height at shear layer breakdown. Consequently, these energy structures are found to be taller in the xy -plane with predominant outer mode streak instabilities (Figure 6.22) than are those in the xy -plane with predominant inner mode streak instabilities (Figure 6.21).

The investigation of a single temporal-mode POD contour, $\tilde{U}_s(N_t)$, is shown in Figure

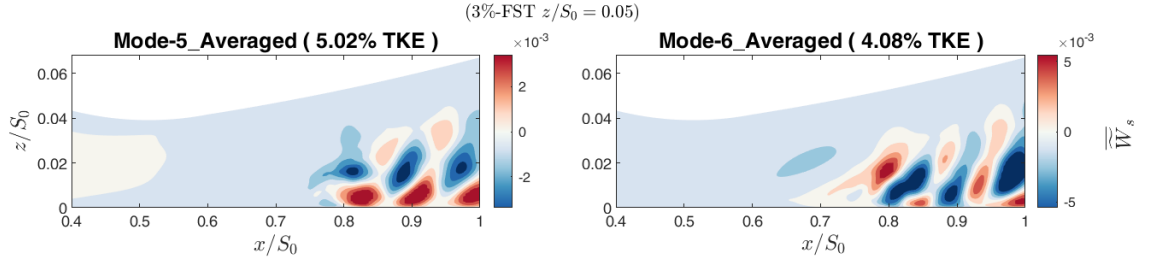


Figure 6.22: POD contour of the w' -velocity field from the left-quarter-span flow field ($z/S_0 = 0.05$).

6.23 and Figure 6.24 with u' -velocity contour lines being overlaid on top of the contour to show the exact locations of the boundary layer streaks. In the temporal-mode POD contour in Figure 6.23, an energised structure can be identified, similar to that in the mid-span POD contour (temporal averaged POD contour in Figure 6.15). The structure here also has correlated contour levels and a tail that points downwards. The actual streak instabilities in the separated shear layer are dominated by the inner mode streak instability, which is hosted by a high-speed streak. In this instability mode, a high-speed streak becomes unstable after interacting with the slow-moving fluid underneath or a low-speed streak below. Once the instability level is saturated, the high-speed streak either rolls into the slow-moving fluid or sheds into the freestream, leading to shear layer breakdown. In this inner mode streak instability case, high-speed streaks in the shear layer are much closer to the plate surface with a small amount of low-speed fluid contained underneath. Therefore, the transition process is also found at the inner part of the boundary layer between $x/S_0 = 0.75$ to $x/S_0 \approx 0.90$. In this region, small vortical structures can be identified with a couple being next to the plate surface. Subsequently, the shear layer begins to break up, and this is also close to the plate surface.

In Figure 6.24, a single temporal-mode POD contour is shown. This POD contour is from the xy -plane located at the left-quarter-span ($z/S_0 = 0.05$) of the computation domain. The transition processes in the current xy -plane are known to happen much further away from the plate surface. They are initiated by the outer mode streak instability which is caused by the interaction between the high-speed free-stream fluid and a low-speed streak in the separated shear layer. From the line contour that highlights the boundary layer streaks, an outer mode streak instability can be observed even after the time-mean transition-onset location ($x/S_0 = 0.75$). Strong shear has been generated by

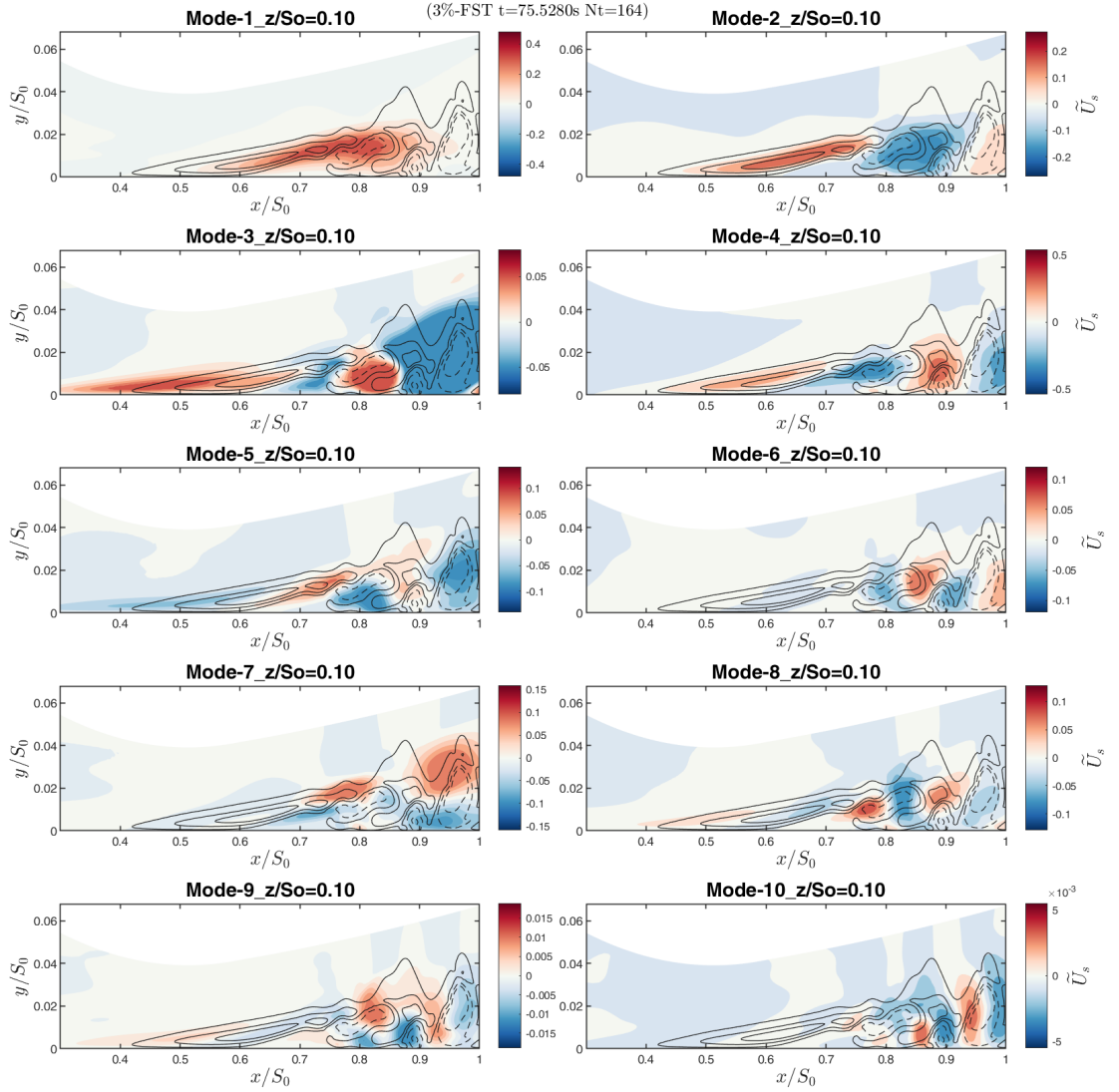


Figure 6.23: POD contour of the u' -velocity field from the mid-span flow field ($z/S_0 = 0.10$). Solid lines: High-speed streaks ($+u'$); Dash lines: Low-speed streaks ($-u'$).

the interaction between the free-stream fluid and the low-speed streak (dash-line). At this location, the low-speed streak begins to roll up once the shear force become saturated. Three small-scale vortical structures represented by $+u'$ (solid lines), can be found between $x/S_0 = 0.75$ and $x/S_0 = 0.85$, located at the edge of the boundary layer. Energy generated by these instability structures has also been captured by the POD analyses. However, the energy contributions from these structures are relatively small compared with the large-scale vortices. Therefore their energy traces only can be found in the high-order modes, Mode-2 to Mode-4, of the POD contour.

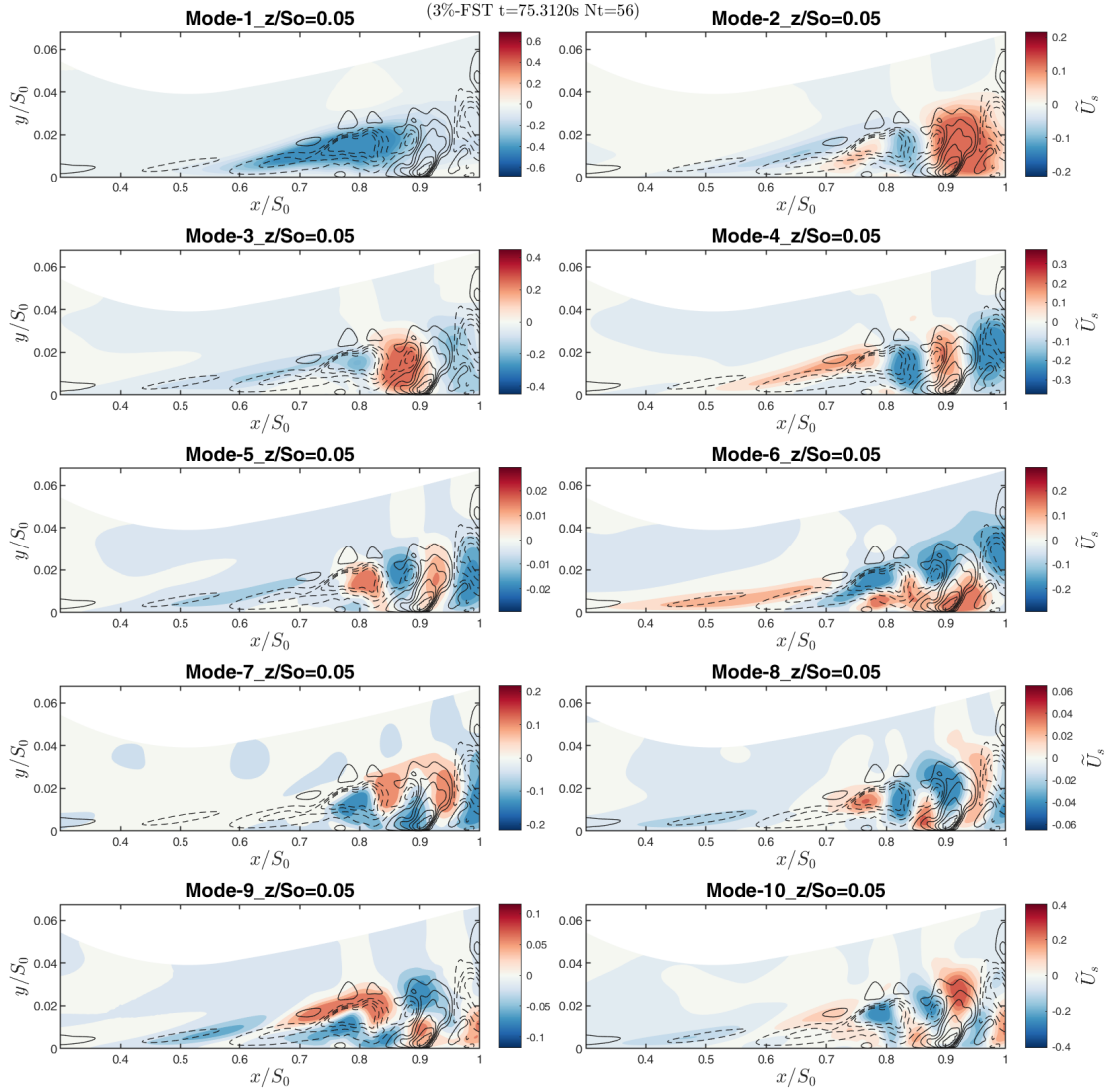


Figure 6.24: POD contours of the u' -velocity field from the left-quarter-span flow field ($z/S_0 = 0.05$). Solid lines: High-speed streaks ($+u'$); Dash lines: Low-speed streaks ($-u'$).

6.4 Summary

The proper orthogonal decomposition (POD) of the fluctuation velocity fields (u' , v' , w') and fluctuation pressure field (P') has been computed and studied here. In the POD calculation, these variables have been decomposed into an arrangement such that it can be represented by different POD modes according to its energy contribution. In such an approach, flow structures with different energy contributions can be separated and studied independently. This can be greatly beneficial when analysing highly complex flow phenomena. Such as, the current separated-flow transition under elevated FST, where it is not possible to be studied the coexistence of multiple instability mechanisms with readily

available analytical tools.

In order to provide a comprehensive understanding of the current flow field, the POD calculation has been carried out on different planes in the three-dimensional space. These include one xz -plane, located at the centre line of the shear layer, and three xy -planes respectively located at the left-quarter-span, the mid-span, and the right-quarter span of the computational domain. These sampling locations have covered the most important flow structures of the current transition process.

Results from the POD analyses have revealed that the dominant K-H instability in the 0%-FST case no longer dominate in the 3%-FST case. This has been supported by the disappearance of the cross-span energy structures normally found in the transition process under 0%-FST. Instead, longitudinal energised streaks are found in both the attached and the separated shear layer even before the transition onset in the 3%-FST case. Furthermore, in the 0%-FST case, the K-H instability has been predominantly captured by Mode-2 of the POD analysis. Whereas, in the 3%-FST case, streaky energy structures linked to the streak instabilities have been captured by Mode-2 and by higher order modes. This is due to the streaks formed in different sizes, and energy contribution by instability of the smaller streaks are less energised. As a result, such energy has been scattered into high-order modes, and energy distribution in the 3%-FST case is less bias to the primary mode contrasting to the 0%-FST case.

Evidence has suggested that the streak instability is the dominant transition mechanism in the 3%-FST case. For example, only longitudinal streaky structures exist in the most energised mode (Mode-1) of the u' -velocity POD contour (xz -plane). Nevertheless, high energy vortical structures from the shear layer breakdown are still captured by most of the POD modes, which indicates the existence of vortex shedding. Upon carefully investigating the sectional time-coefficient PSD, a shear layer base frequency can be identified in different span-wise locations. These frequency peak of 24Hz are within the range of frequencies that are unstable to the K-H instability ($0 < f < 29.61(\text{Hz})$). This evidence reveals that the K-H instability indeed exists. However, these frequency peaks in different span-wise locations have different energy levels. Therefore, it is reasonable to agree that K-H instability is a localised event. The current POD analyses have provided strong evidence for the coexistence of both the streak and K-H instability with the former being the dominated transition mechanism.

The POD mode visualisation has also provided evidence for the existence of both the outer and the inner mode streak instability, which are well-known in bypass transition. These two streak instability mechanisms have been found in different span-wise locations, which indicates that they are localised transition activities. Also, the differences between these two streak instabilities have been provided by the POD analyses. The outer mode streak instability is found to happen close to the edge of the boundary due to the interaction between the high-speed free-stream fluid and a low-speed streak within the shear layer. The breakdown of the shear layer is also happening near the boundary layer edge. POD analyses have captured the related high energy vortical structures from the vortex shedding. These are also away from the plate surface. Whereas the inner mode streak instability is caused by interaction between a high-speed streak and the low-speed fluid within the separation bubble. Therefore, vortical energy structures from the boundary layer breakdown are found next to the plate surface. While these energy structures are in contact with the plate surface, their spectral characteristics have also been altered.

Chapter 7

Boundary-Layer Streak Instability

7.1 Introduction

Boundary layer streaks are longitudinal propagating vorticities formed due to boundary layer receptivity to free-stream turbulence. These streaks can cause span-wise modulations that accompany the thickening and thinning of the boundary layer. These boundary layer streaks are termed Klebanoff streaks. The presence of streaks has been found locally to prevent the usual transition route via K-H instability. Nevertheless, transition is still promoted by other kinds of localised instability mechanisms, caused by the interaction of streaks and the surrounding fluid. The current study indicates that these streak interactions are the dominant mechanism responsible for triggering the instability promoting transition. Meanwhile, the K-H instability is still at work locally, and it has led to weak vortex shedding activities. In this chapter, visualisation of three-dimensional transitional flow structures is provided and analysed. Additionally, particle tracking analysis has been carried out to provide additional information about the streak instability mechanisms.

7.2 Streak Identification

As boundary layer streaks are dominated by the stream-wise velocity component, the stream-wise velocity fluctuation, u' , has been widely used for the measure of streaks inside the boundary layer. A high-speed streak can be identified by a positive velocity fluctuation ($+u'$), whereas a low-speed streak can cause negative velocity fluctuation ($-u'$). Streaks propagate inside the boundary , normally accompanied by a concave or convex region on the boundary layer surface. Figure 7.1 shows the normalised velocity fluctuation line

contour of cut-planes at four different wall-normal locations between $y/S_0 = 0.0008$ to $y/S_0 = 0.0124$.

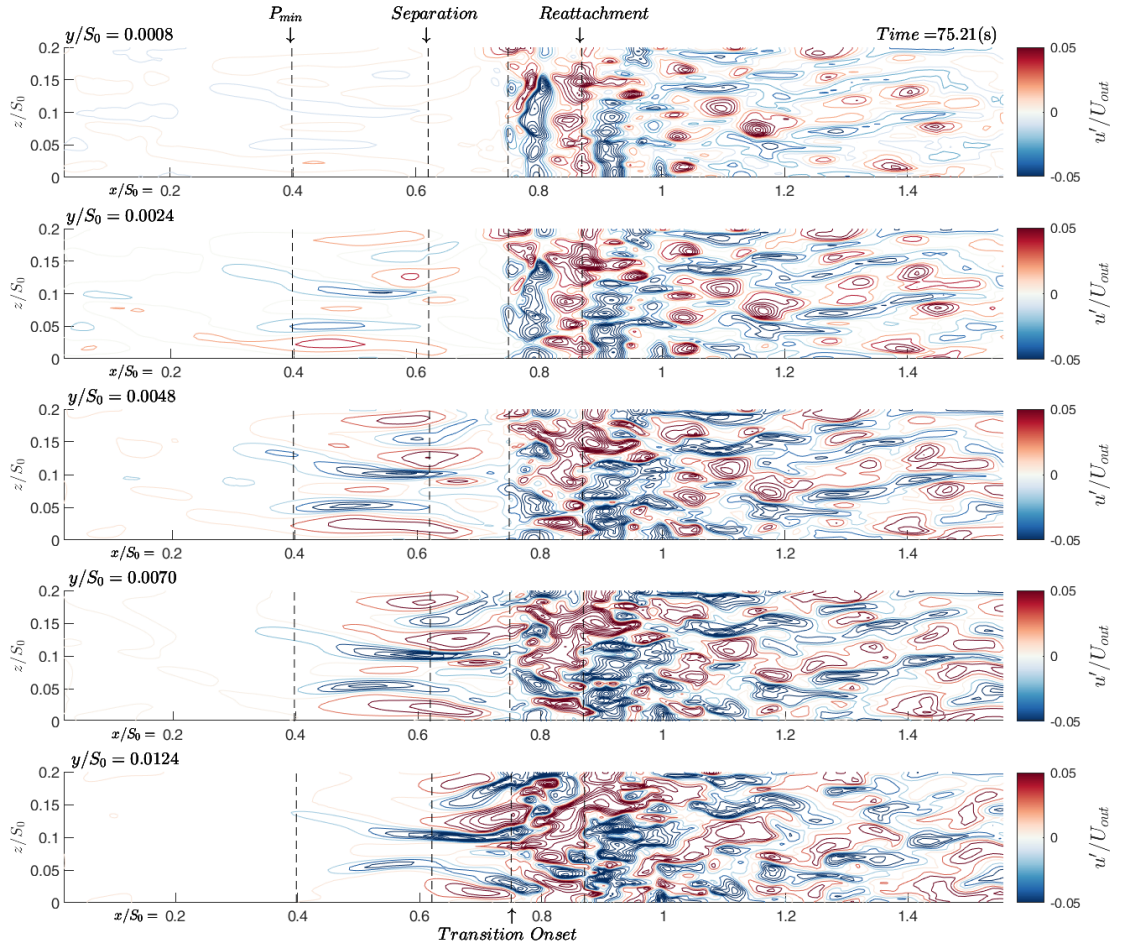


Figure 7.1: Normalised velocity fluctuation, u' , line contour of xz -plane at $y/S_0 = 0.0008$, 0.0024, 0.0048, 0.0070, and 0.0124 of an arbitrary time step.

In this figure, high-speed streaks ($+u'$) are illustrated in red and low-speed ones ($-u'$) in blue. Both low- and high-speed streaks can be identified inside the boundary layer before the transition-onset location ($x/S_0 = 0.75$). This aligns with the streaky energy structures that appear in the xz -plane POD contours in Chapter 6 Figure 6.8. These streaks originate from small patches of free-stream disturbances that impinge on the flat plate leading edge, in which low-frequency disturbance is transferred into the thin boundary layer through the shear sheltering mechanism (Jacobs and Durbin (2001) and Zaki (2011)). Consequently, small patches of velocity fluctuation can be observed before $x/S_0 = 0.2$ in three nearest cut-planes to the wall ($y/S_0 = 0.0048$ or below). Before the P_{min} location, the favourable pressure gradient has suppressed the development of these immature streaks. Once prop-

agating past this location, streaks start to strain, and their amplitude grows dramatically. Streak elongations can clearly be observed after the P_{min} location, which continue into the separated shear layer. In this location, the streak amplitude grows dramatically and can be of an order of magnitude higher than before.

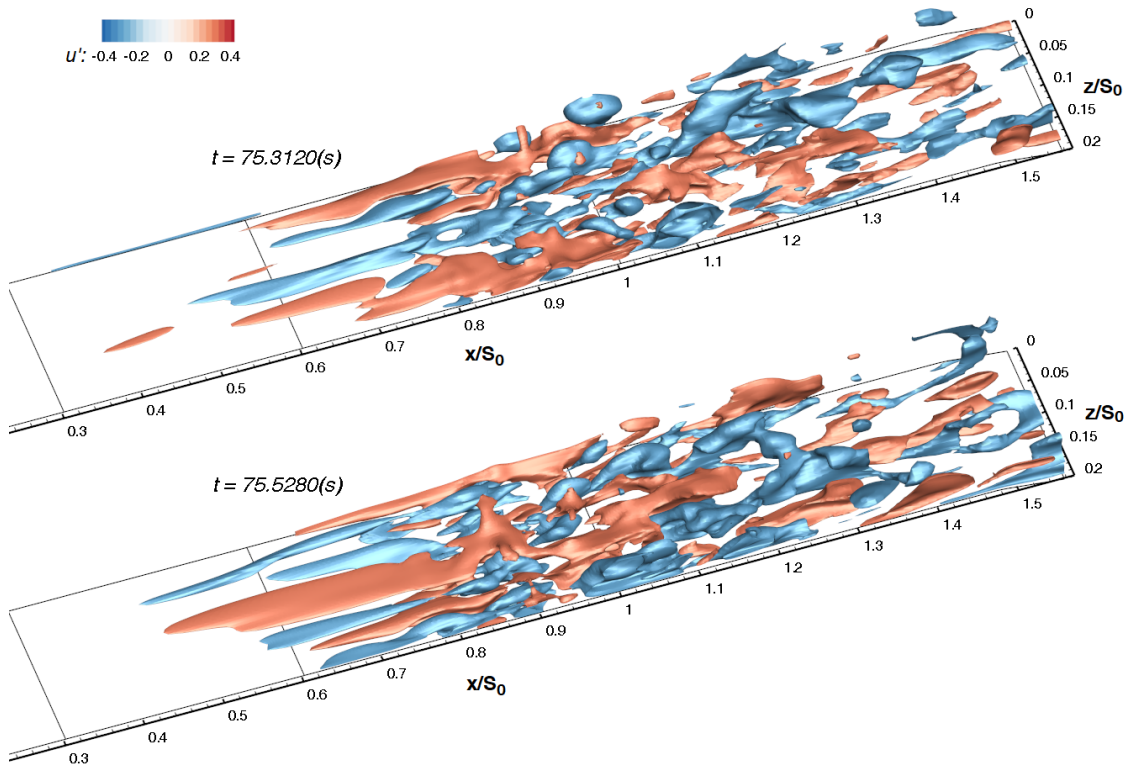


Figure 7.2: u' -velocity iso-surfaces to demonstrate boundary layer streaks in the three-dimensional space.

In the three-dimensional space, streaks can also be visualised by u' -velocity iso-surfaces, as shown in Figure 7.2. This figure has demonstrated streaks and related downstream flow structures in two different time steps. Noticeably, streaks with different span-wise wavelengths can be observed. The increase in span-wise wavelength is mostly observed to happen in a high-speed streak when it enters the shear layer. However, the cause remains unclear. Streak magnitude only begins to grow after the minimum pressure location, P_{min} , in both Figure 7.1 and Figure 7.2. Therefore, the length of streaks is significantly shorter than those found in bypass transition (Vaughan and Zaki (2011), Zaki (2011), Zaki and Durbin (2006), and Jacobs and Durbin (2001)). This may also imply that the streak instabilities and the related breakdown process may be different from those in bypass

transition.

7.3 Vortex Identification Methods

Multiple vortex identification methods have been previously employed to identify vortices caused by streak instabilities. Two of the most popular methods in transition studies are λ_2 -criterion and Q-criterion. Results from both criteria have been computed and compared in Figure 7.3. Only a small discrepancy can be found between the two approaches. In some situations, slightly better large-scale structure is provided by the Q-criterion. Therefore, it is employed here to identify vortex structures.

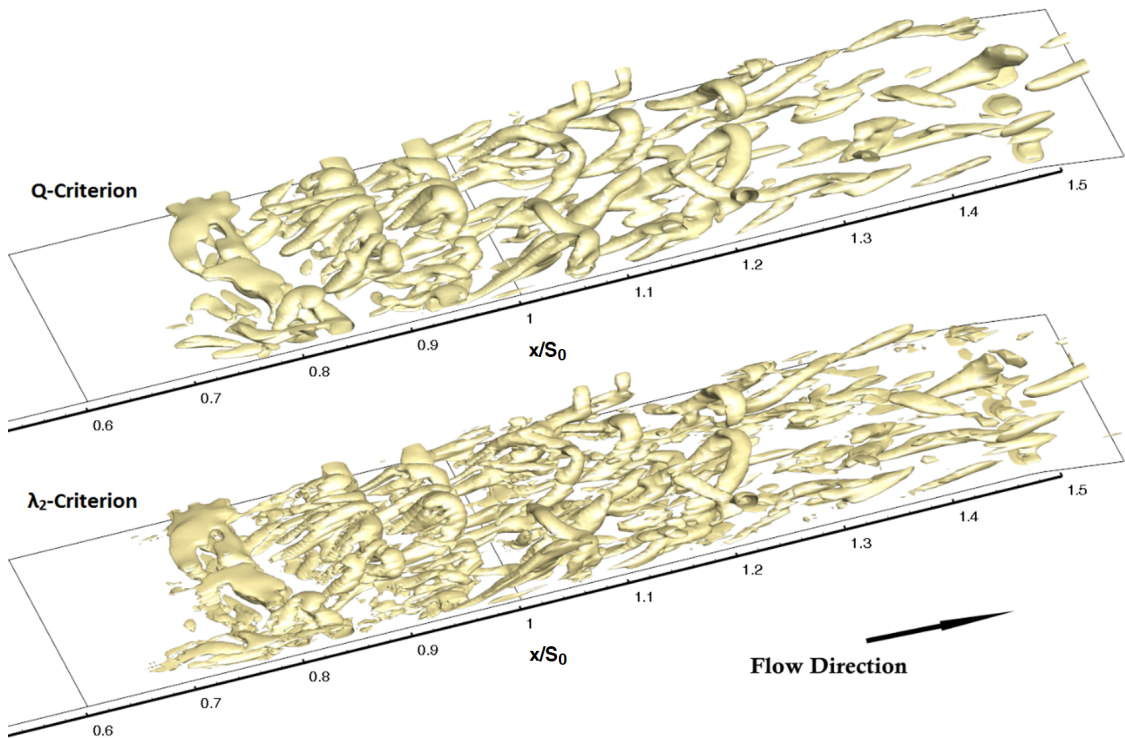


Figure 7.3: Comparison between the λ_2 -criterion and Q-criterion on identifying coherent flow structures from the current separated-flow transition and breakdown.

7.4 Streak Instability - Overview

In bypass transition, such as the one in Vaughan and Zaki (2011), streaks can develop into primary and secondary instabilities, with some leading to further turbulent spot inception. However, in the current separated-flow transition, no evidence is found to

support turbulent spot inception. Instead, shear layer breakdown follows directly from the streak (secondary) instability in the separated shear layer. “Secondary instability” is termed in such a way that it can be differentiated from primary instability. Streak interactions leading to streak instabilities are considered to be the primary instability stage.

In a carefully controlled forcing environment, two streak instability modes are predicted by linear stability analysis (Vaughan and Zaki (2011)). These are the inner and outer mode streak instabilities. Hack (2014) reported that the inner mode streak instability could arise due to interaction between a high-speed streak and a low-speed streak when under an adverse pressure gradient. A typical velocity profile of the inner mode streak instability should have an inflection point that is close to the surface. Respectively, for the outer mode streak instability, this is caused by the interaction between lifted low-speed streaks and high-speed free-stream fluid. A typical velocity profile of this instability mechanism should have an inflection point that is away from the plate surface, more specifically, it is near the shear layer edge.

Additionally, the two modes of streak instability from bypass transition are found to be similar to the two instability modes from Götler flow (Swearingen and Blackwelder (1987)). They can have both the varicose (symmetric) and the sinuous (asymmetric) breakdown pattern (Brandt and de Lange (2008)). The varicose mode is caused by a symmetry breakdown of two momentum streaks. An instability wave is therefore amplified when the surface shear is promoted by a high-momentum streak going over a lower-momentum one. The sinuous mode can be found from the anti-symmetry interaction of two momentum streaks with partial overlap. An instability arises through a side-impact of a high- and a low-momentum streak, in which the former is bent sideways. The instability wave is amplified mostly due to the span-wise shear.

In the current research, the two modes of streak instability have been confirmed by the POD analyses. However, discrepancies remain when comparing with bypass transition. This can be concluded from flow visualisations and particle tracking analyses as follows. First, the streak (secondary) instability has not caused turbulent spot inception. Second, the inner and outer mode streak instability are found to be different to those from the bypass transition. Finally, the breakdown patterns of the outer mode are different to those from the bypass transition.

7.5 Streak Instability - Inner Mode

Two-dimensional Flow Visualisation

Figure 7.4 below shows the two-dimensional (2D) temporal evolution of a boundary layer streak with inner mode streak instability over 10 time steps (with a time-interval of 0.01(s)). At the beginning of the process, a high-speed streak ($+u'$) can be observed near the boundary layer mean separation point ($x/S_0 = 0.62$). A high-speed streak is known to host an inner mode streak instability. From the particle-tracking history shown in Figure 7.7, a seeded particle inside the high-speed streak is found to be accelerated more strongly when the streak magnitude becomes intense. As a result, fluid inside a high-speed streak has a higher velocity than the fluid below and is marginally slower than the free-stream fluid. Streak instability can arise when the high-speed streak moves over any low-speed fluid below. This can be the stationary fluid inside the separation bubble, or a low-speed streak entrained underneath the separated shear layer. This process can be observed between $t = 75.68(s)$ and $t = 75.69(s)$ in Figure 7.4. In the next stage, streak instability rises, and streak undulation can be observed from the high-speed streak between $x/S_0 = 0.70$ to $x/S_0 = 0.80$ at $t = 75.70(s)$. Subsequently, the streak starts to shed off and rolls up into turbulent flow.

7.5.1 Three-dimensional Flow Visualisation

In the three-dimensional (3D) space, the above-mentioned inner mode streak instability is demonstrated in Figure 7.5. When the high-speed streak (inside the black box) moves over the low-speed fluid below, surface shear arises at the interface. This leads to the formation of two-dimensional part-span rollers. These rollers are represented by the increased Q-criterion value (coloured gold). The development of this high-speed streak and the 2D part-span rollers is shown in Figure 7.5 A-C. A xy -plane ($z/S_0 = 0.15$) located at the centreline of the high-speed streak is also investigated here (Figure 7.5 D-F). The 2D rollers (coloured gold), represented by the increased Q-criterion value, can be clearly observed below the high-speed streak. This indicates that the inner mode streak instability herein is an inviscid instability mechanism.

After the investigation of the two velocity profiles (u and u') in Figure 7.6, the velocity profile herein is found comparable to the velocity profile from the K-H instability mecha-

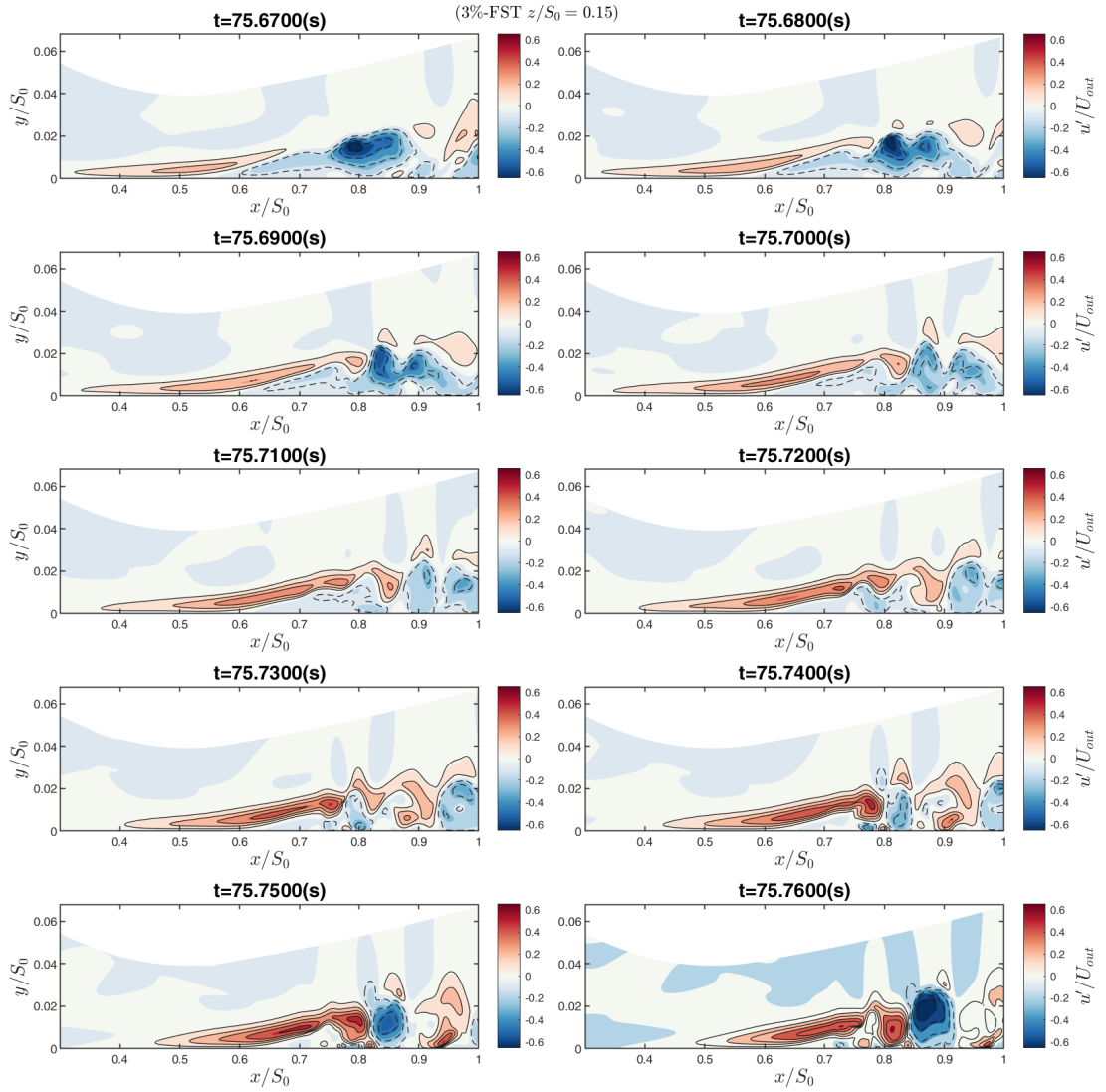


Figure 7.4: A transient contour plot illustrates the evolution of a typical inner mode streak instability in the 2D space.

nism (shown in Figure 4.15b). The current instability mechanism is also considered similar to the K-H instability. However, it is a span-wise localised transitional activity. From the u' -velocity profile in Figure 7.6, the upper surface of the high-speed streak is found to be situated in the freestream. It propagates z with a velocity comparable to the free-stream velocity. Therefore, no surface shear arises at the top surface of the high-speed streak. The centreline of the high-speed streak is found propagating at approximately 90% of free-stream velocity. The maximum velocity difference can be identified between the lower edge of the high-speed streak and the reversed flow below. The instability originating from this location agrees strongly with the previous observation from both the 2D and 3D flow

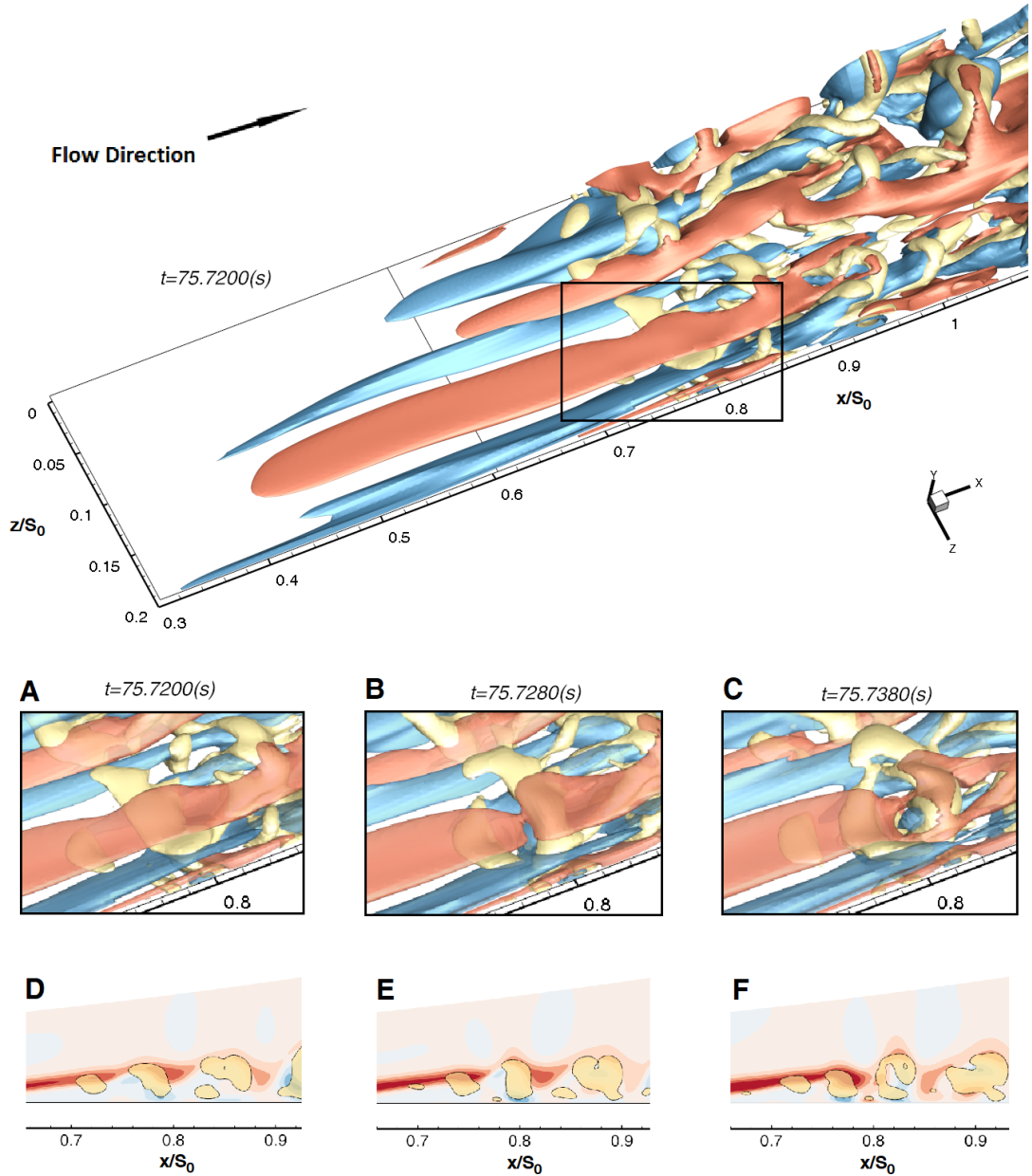


Figure 7.5: A transient iso-surfaces plot illustrates the evolution of a typical inner mode streak instability in the 3D space. Red: High-speed streak ($+u'$). Blue: Low-speed streak ($-u'$). Gold: Q-criterion iso-surface.

visualisations.

After the streak span-wise wavelength has increased, the inner mode streak instability mechanism is comparable to the K-H mechanism, but exists only locally. The resultant 2D span-wise rollers from the streak interaction are partly spanned and are previously termed as the part-span K-H rollers (Coull and Hodson (2011) and Nagabhushanan et al. (2013)).

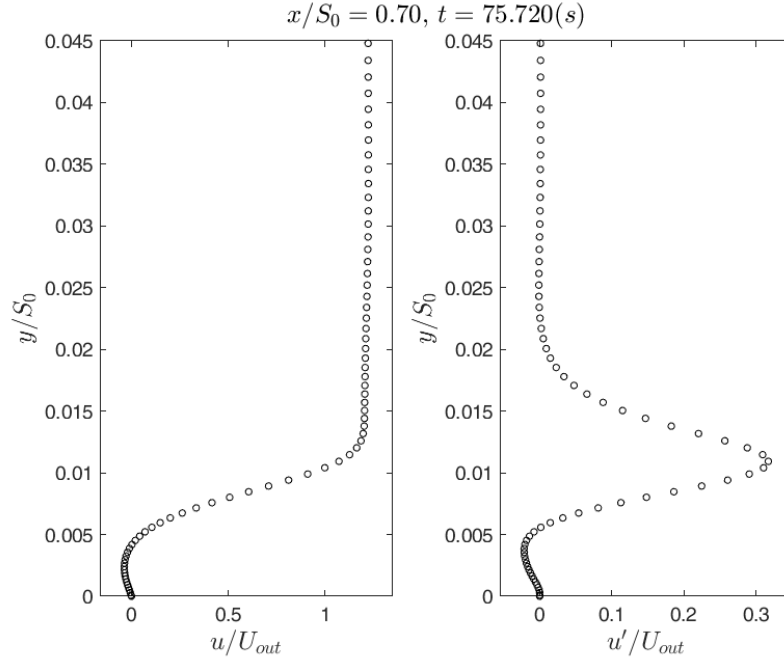


Figure 7.6: Velocity profiles (u and u') at $x/S_0 = 0.70$ and $t = 75.7200(s)$.

7.5.2 2D Particle Tracking - Inner Mode

A particle-tracking analysis of a seeded point inside a high-speed streak has been carried out. The objective is to provide more information on the streak instability mechanism and information on the corresponding breakdown pattern. Figure 7.7 shows the path of the particle that has been seeded inside the high-speed streak at $t = 75.67(s)$. At the initial stage, this particle has travelled alongside the high-speed streak. It is elevated after the boundary layer separates and the streak is travelling inside the separated shear layer. After the particle has passed the separated shear layer and arrives at the aft portion of the time-mean separation bubble, the particle path becomes unsteady due to the local flow breaking down. As can be seen from the velocity information gathered along the particle trajectory shown in the first subplot of Figure 7.8, the particle is found to descend suddenly, rising again after $x/S_0 > 0.80$.

Figure 7.8 shows the velocity information gathered during the streak path. From velocity information along the particle trajectory, the instability of the current high-speed streak can be seen to be caused by both the stream-wise and wall-normal velocity fluctuation components between $x/S_0 = 0.70$ to $x/S_0 = 0.80$. From the u' - and v' -velocity fluctuations history, both velocity components are found to dominate in the instability process. Although there are some strong span-wise deviations of the w' -velocity between

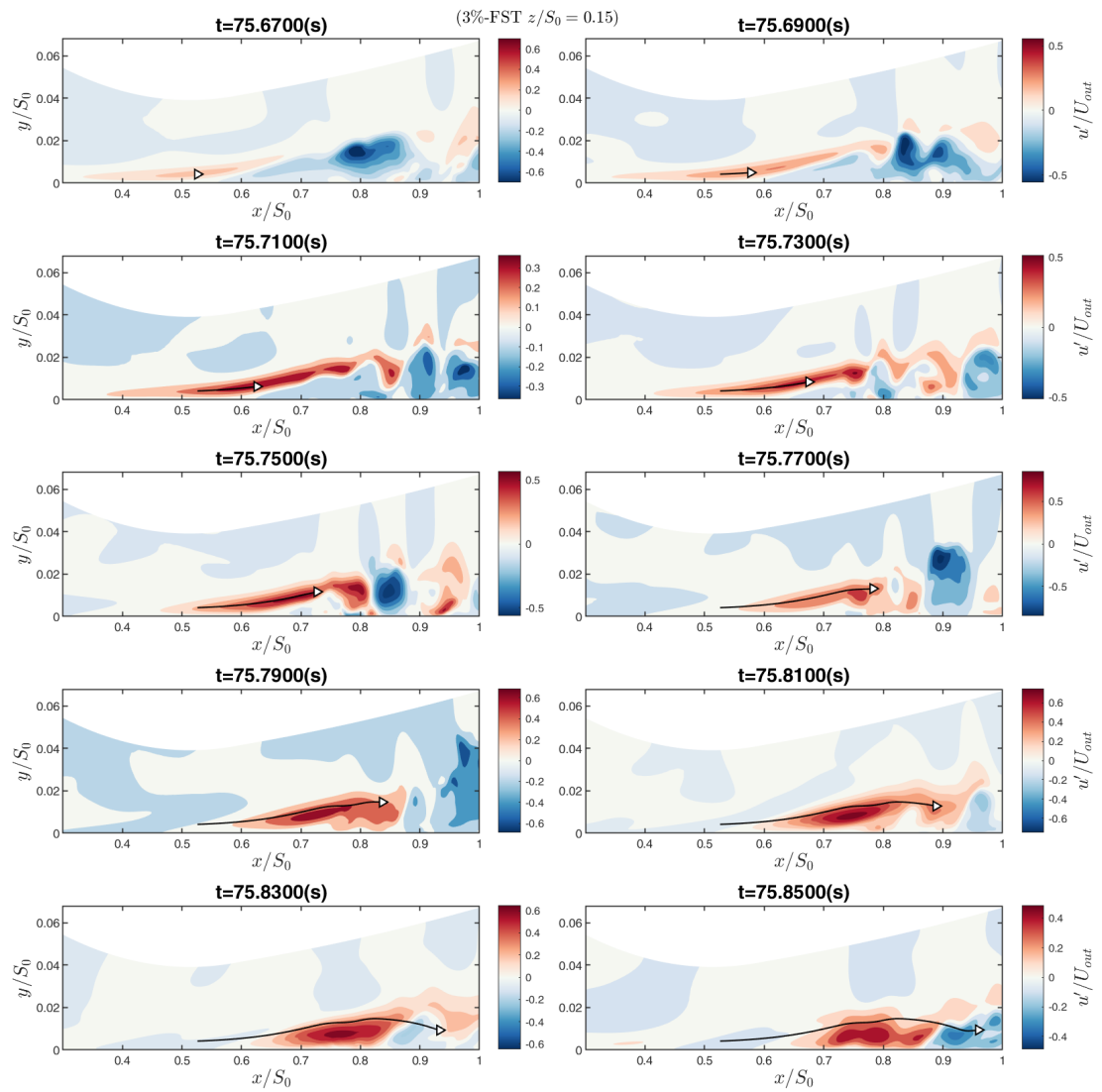


Figure 7.7: Particle trajectory inside the high-speed streak that leads to the inner mode streak instability.

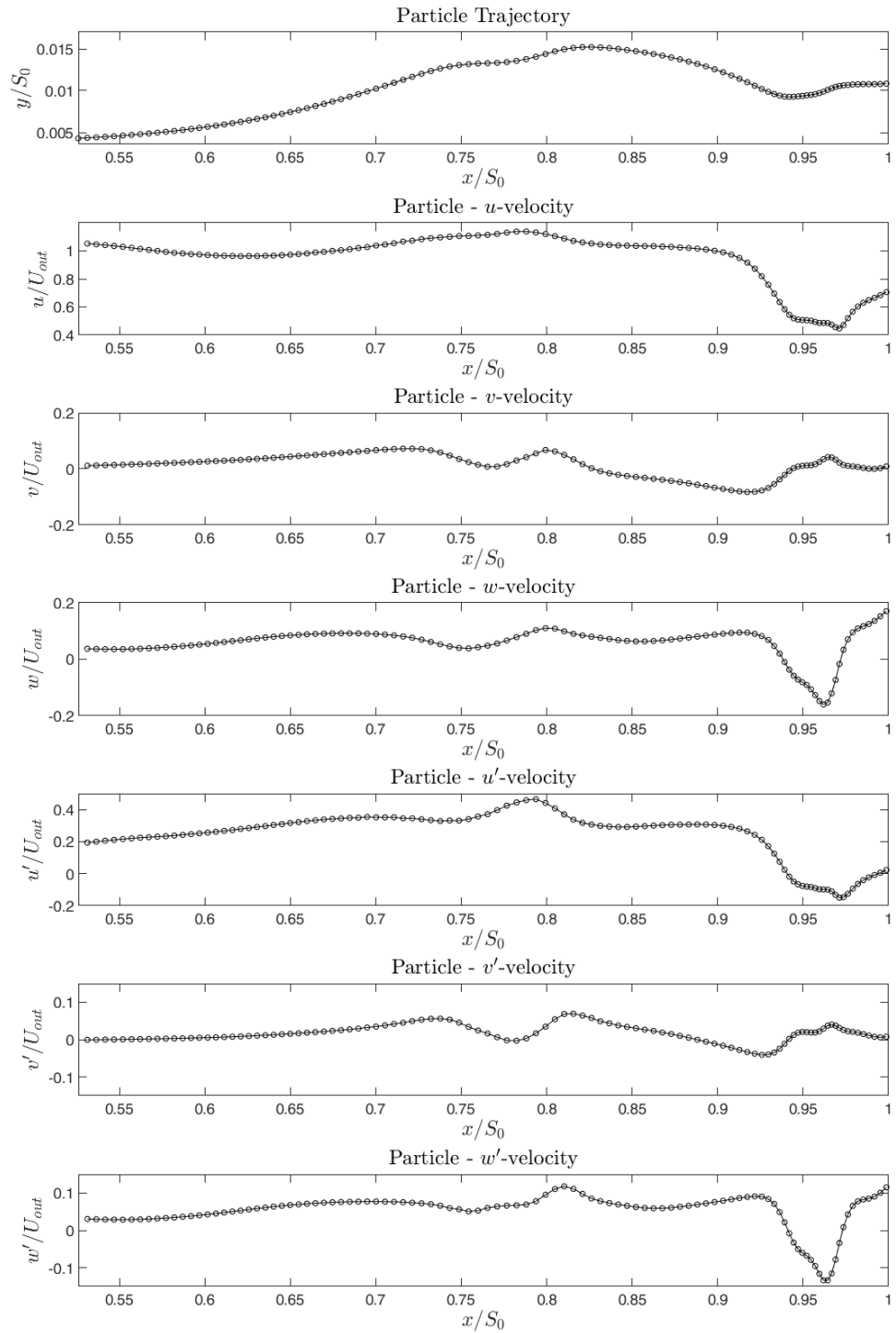


Figure 7.8: Particle-velocity information along the particle trajectory inside the high-speed streak that leads to the inner mode streak instability.

$x/S_0 = 0.7$ to $x/S_0 = 0.80$, the w' -velocity fluctuation remains relatively linear in this region. As a result, the particle has only displaced in the span-wise direction without significant span-wise fluctuations. The varicose breakdown pattern is considered here without any sinuous breakdown activity aligning with the bypass transition.

7.6 Streak Instability - Outer Mode

Two-dimensional Flow Visualisation

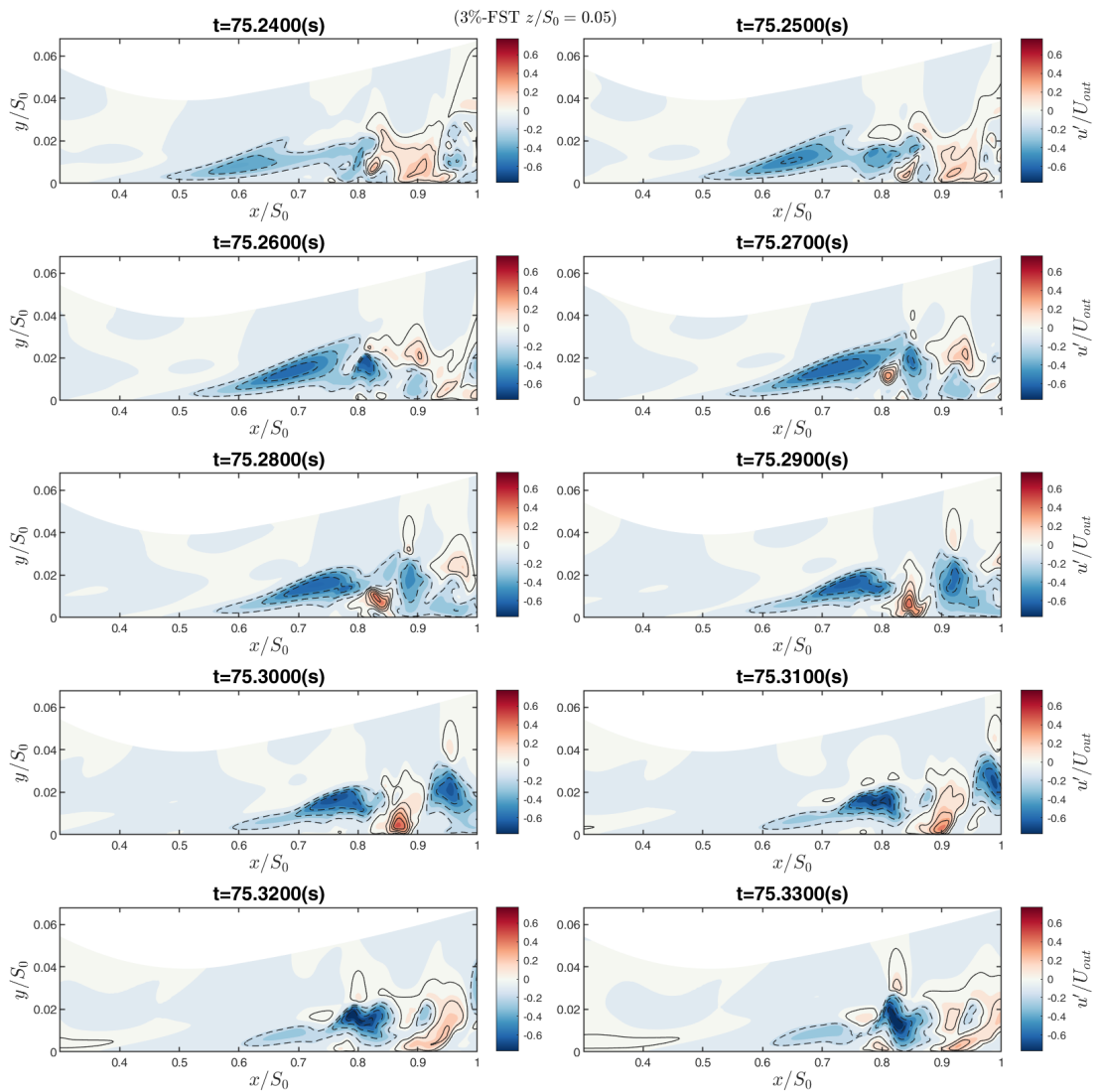


Figure 7.9: A transient contour plot illustrates the evolution of a typical inner mode streak instability in the 2D space.

Figure 7.9 demonstrates the development of a low-speed streak from streak interaction

to breakdown. At the beginning of the process ($t = 75.24(s)$), a low-speed streak (between $x/S_0 = 0.48$ to $x/S_0 = 0.68$) is found to propagate on top of another low-speed streak. This has resulted in the lift-up motion of the upstream low-speed streak. This phenomenon has also been reported in the outer mode streak instability in bypass transition. As demonstrated by contours between $t = 75.26(s)$ and $t = 75.30(s)$, the down-stream portion of this low-speed streak is in the freestream and interacts with the high-speed free-stream fluid. This has resulted in an inflection velocity profile at the edge of the boundary layer. An instability process develops when quasi-2D-rollers are formed on top of the low-speed streak. These flow structures are shown at $t = 75.31(s)$ (between $x/S_0 = 0.70$ and $x/S_0 = 0.84$). They are followed by the roll-up of the low-speed streak, which also indicates the roll-up of the shear layer.

7.6.1 Three-dimensional Flow Visualisation

In the 3D space, the current example of the outer mode streak instability is demonstrated in Figure 7.10 A-C. The development of the instability activity is first observed at the downstream edge of the low-speed streak. A ring-like vortex structure (coloured gold) with increased Q-criterion value can be found wrapping around the top half of the low-speed streak (coloured blue). The instability process becomes more intense in the next time step ($t = 75.31(s)$), in which three ring-like vortex structures (coloured gold) with increased Q-criterion values, are formed. These again wrap around the low-speed streak, as shown in Figure 7.10 B. In a later time step, the low-speed streak rolls up, and the ring-like vortex structure is continuously situated on top. This results in a 3D breakdown structure located at the north-east corner of Figure 7.10 C. The ring-like vortex structures (coloured gold), with increased Q-criterion value, are believed to be a precursor of the well-known Hairpin vortices. They mostly develop into Hairpin vortices in the turbulent breakdown stage.

Figure 7.10 D-F shows the contour plots on a xy -plane ($z/S_0 = 0.05$) located at the centreline of the low-speed streak. These plots agree well with the observation from the 3D iso-surface plots, in which circular structures (coloured gold) with increased Q-criterion values, can be found on top of the low-speed streak (coloured blue). These indicate that increased surface shear and a highly inflectional velocity profile can be found near the boundary layer edge. As demonstrated in 7.11, an inflectional velocity profile indeed

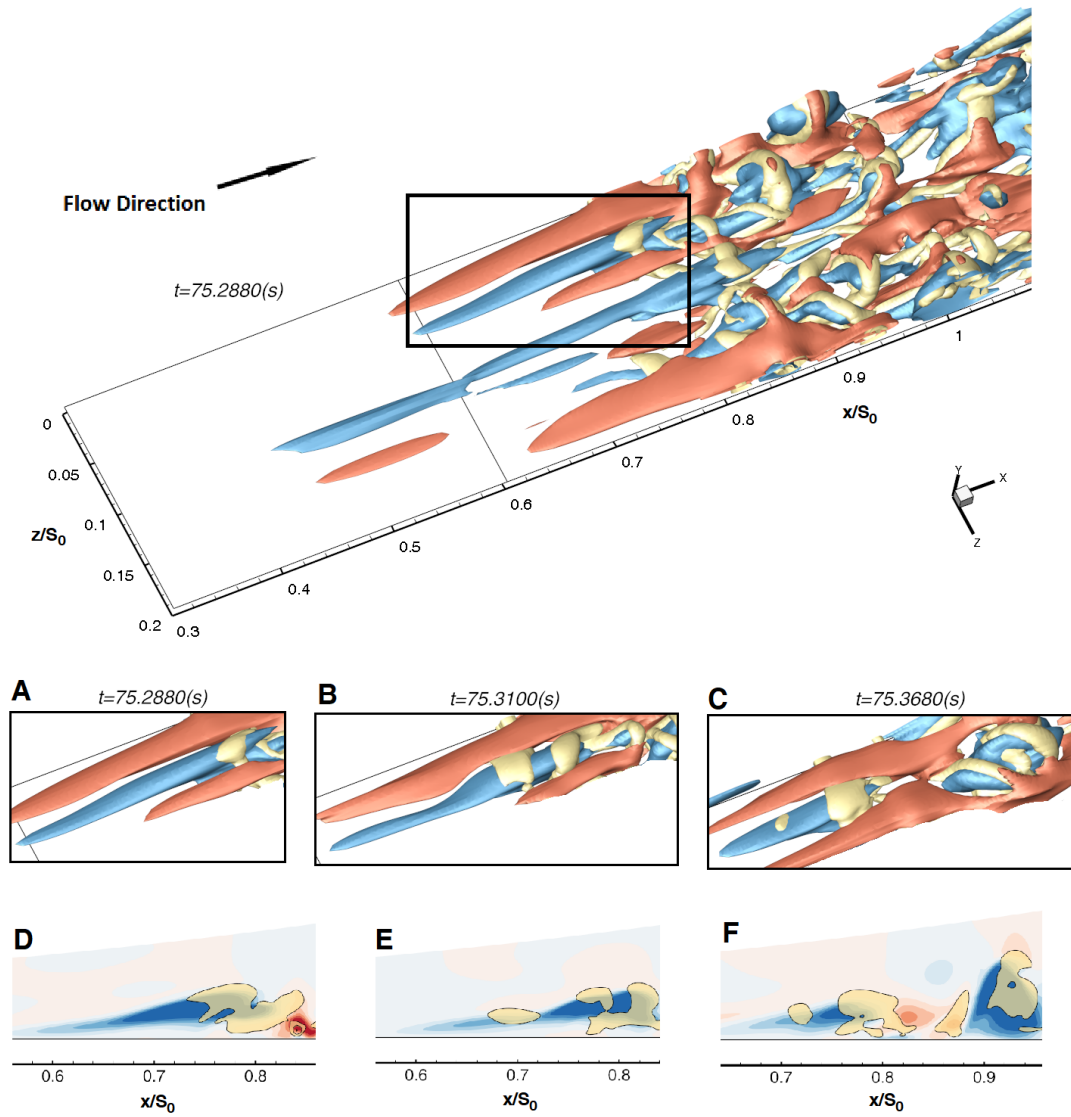


Figure 7.10: A transient iso-surfaces plot illustrates the evolution of a typical outer mode streak instability in the 3D space. Red: High-speed streak ($+u'$). Blue: Low-speed streak ($-u'$). Gold: Q-criterion iso-surface.

exists near the boundary layer edge and the upper surface of the low-speed streak. The centreline of the low-speed streak (minimum u' -value) can be identified from the right-hand-side u' -velocity plot. It is found to travel at approximately 37.5% of the free-stream velocity. The shear layer has been formed between the low-speed streak centreline and the free-stream fluid.

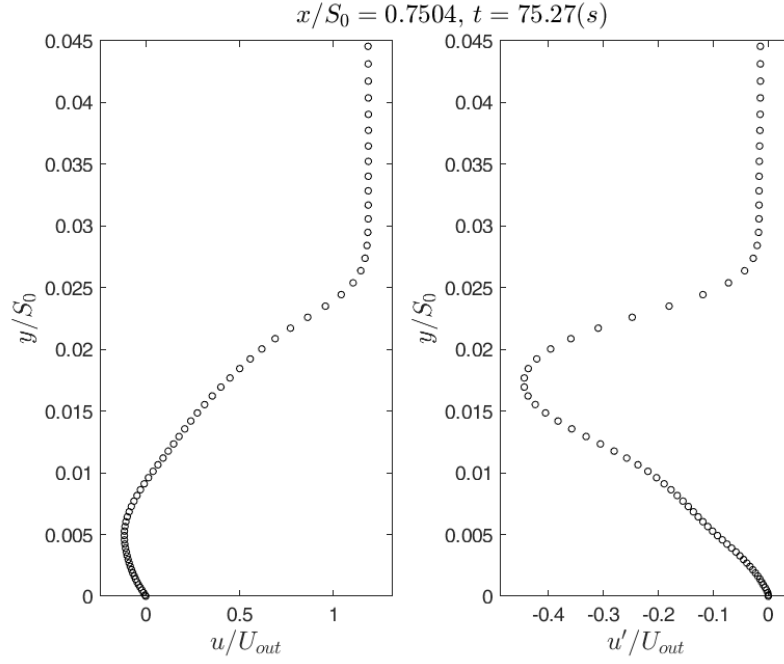


Figure 7.11: Velocity profiles (u and u') at $x/S_0 = 0.75$ and $t = 75.27(s)$.

7.6.2 2D Particle Tracking - Outer Mode

As shown in Figure 7.12, the seeded particle trajectory from the outer mode streak instability contrasts with the one from the inner mode (Figure 7.7). In the outer mode, the particle location rises while moving downstream after $x/S_0 = 0.80$, whereas the particle path is found to decline in the inner mode. This is considered to be a result of having a different inflection point location in the velocity profile. The outer mode has an inflection point away from the flat plate surface near $y/S_0 = 0.02$, and the inner mode has an inflection point close to the flat plate surface near $y/S_0 = 0.008$. In the outer mode, the seeded particle decelerates when travelling inside the low-speed streak. In contrast to the outer mode, the seeded particle is found accelerating when travelling in the high-speed streak of the inner mode.

Figure 7.13 shows the velocity information gathered by the particle while propagating downstream. In this figure, the low-speed streak is discovered to be relatively steady before the stream-wise location at $x/S_0 = 0.75$. Here, only the u' -velocity fluctuation increases gradually and the other two velocity components remain constant. At $x/S_0 = 0.80$, the v' -velocity fluctuation suddenly has a 14% increase in magnitude. Also, the u' -velocity fluctuation increases to the maximum value (approximately 15%) at $x/S_0 = 0.83$. For the w' -velocity fluctuation component, only a small amount of fluctuation can be observed,

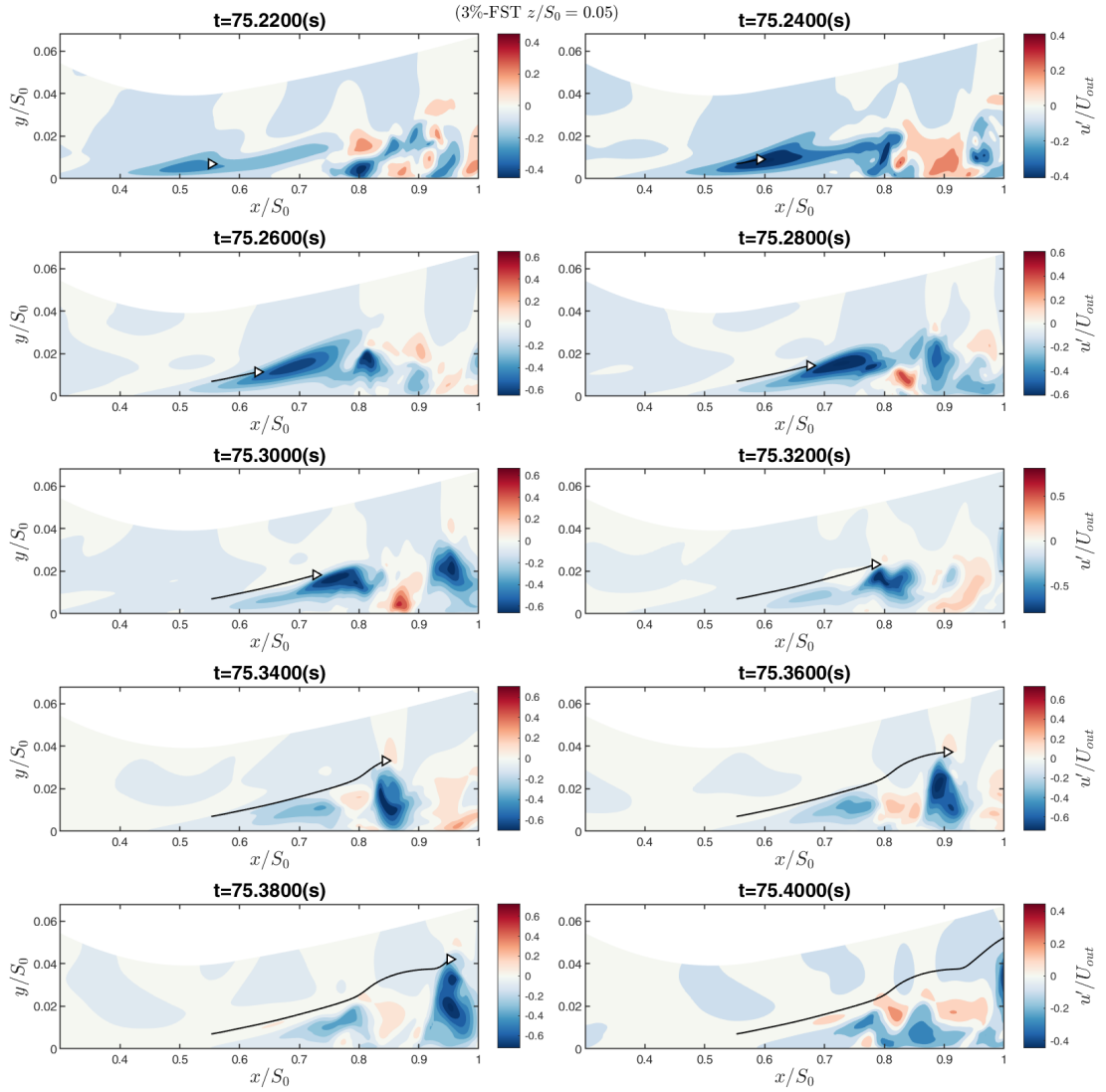


Figure 7.12: Particle trajectory inside the low-speed streak that leads to the outer mode streak instability.

which is smaller than those found in the other two velocity components. Consequently, the instability stage here is considered to be dominated by both the stream-wise and wall-normal velocity components and is considered via the varicose (symmetric) breakdown pattern. This is due to there being almost on span-wise fluctuation velocity component involved in the instability stage.

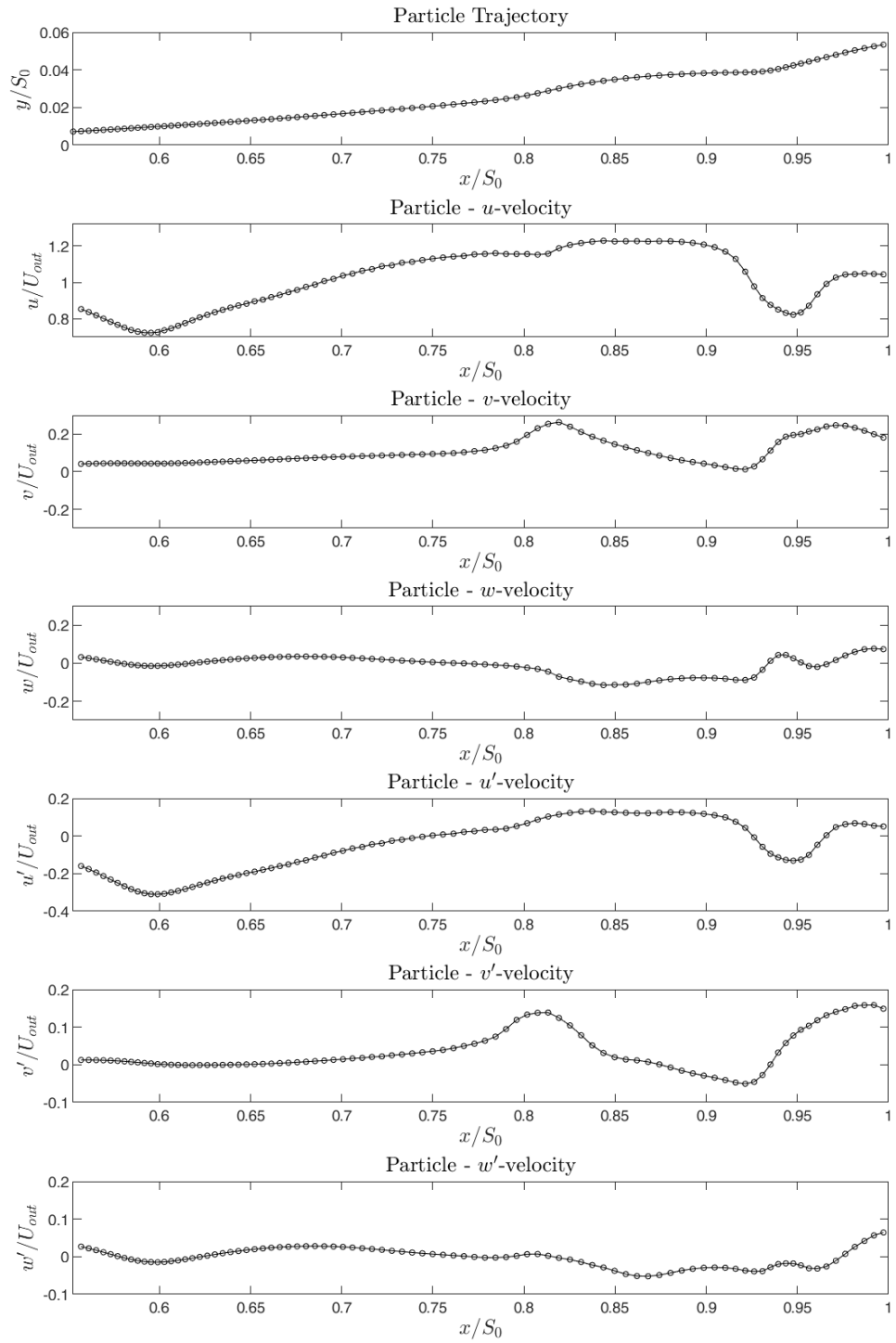


Figure 7.13: Particle velocity information along the particle trajectory inside the low-speed streak that leads to the outer mode streak instability.

7.7 Summary

In the current study, two modes of streak (secondary) instabilities from the separated-flow transition have been analysed using different visualisation techniques, which include 2D and 3D flow visualisation, as well as 2D particle tracking. Currently, the two modes of streak instability are found to have some similarities to the two modes of streak instabilities from the bypass transition. Nevertheless, differences remain. Analogous to the bypass transition, the inner and outer mode streak instability are respectively caused by a near wall inflection point in the velocity profile and a near boundary layer edge inflection point in the velocity profile. Apart from this, other aspects of the two streak instability modes are found to be different to those in the bypass transition. First, both streak instability modes are inviscid shear layer instabilities found in the boundary layer. This is not the case in the bypass transition, where the separation bubble is eliminated. The two modes of streak instability are considered viscous instabilities. Second, similarity can be found between the inner mode streak instability and the K-H instability. The part-span K-H rollers are believed to be caused by the inner mode streak instability. This is a result of the span-wise wavelength of the host streak increasing. Third, the outer mode streak instability arises due to the formation of ring-like structures (increased Q -criterion value) wrapping around the low-speed streak. These ring-like vortex structures are precursors to the Hairpin vortex. Lastly, the breakdown patterns from these two streak instability modes are via the varicose (symmetric) pattern, with both the stream-wise and wall-normal velocity components dominating in the process.

Chapter 8

Conclusion

8.1 Conclusion

Boundary layer separated-flow transition under 3% FST and adverse pressure gradient has been numerically investigated. An LPT blade represented model is employed with the separated-flow transition triggered on an elliptical leading edge flat plate. The computational model can therefore be greatly simplified by neglecting the surface curve effect from a turbine blade, which is less significant in the transition process than is FST. Boundary layer separation was induced by an imposed pressure distribution taken from a “high-lift” LPT blade suction surface. This pressure profile is applied to the two flat-plate surfaces by opposing contour walls. An LES approach with the dynamic SGS turbulence model was employed to carry out the numerical simulation. FST applied to the inlet of the computational domain was generated by a numerical tripping method belonging to a branch of the synthetic fluctuation approach. The current computational mesh has also been carefully designed, minimising the input from the SGS turbulence model in regions that contain important flow structures. Consequently, the time-mean flow field of the current LES prediction has a good agreement with the experimental observation and the previous LES prediction.

In the first analysis, K-H instability has been confirmed by a stability analysis in the 0%-FST case. A frequency peak exists in the PSD analysis, satisfying the K-H instability criterion. From flow visualisation, K-H related cross-span rollers are also observed, indicating the existence of shear layer shedding activities and, most importantly, the existence of K-H instability. This frequency peak has not been detected in the 3%-FST case. In-

stead, Klebanoff streaks exist and propagate inside both the attached and the separated shear layer before the transition-onset location. Turbulence spot inception in the attached boundary layer has been ruled out by investigation of the maximum RMS velocity plots of all three velocity components. Consequently, bypass transition is considered not to be the current transition mechanism. In the PSD analysis, there are a few less distinctive frequency peaks existing near the transition-onset location. Although the lowest frequency peak has a Strouhal number that is slightly above the K-H vortex shedding Strouhal number, vortex shedding and part-span K-H rollers can still be identified from the flow visualisation. As a result, the K-H instability is considered to exist in the current transition process. Nevertheless, it is a localised transition activity. Also, K-H instability and the streak-related instabilities are confirmed to coexist in the current transition process under 3% FST. The 2D K-H rollers are found to be severely disrupted by passing through streaks which have rapidly developed into 3D motions. The current study has confirmed the bypassing of the usual K-H related secondary instability stage, which is not reported previously. Additionally, a much shorter transition length and separation bubble length can be identified under 3% FST.

In the second analysis, the effect of FSTI on separated-flow transition is investigated and the transition process was compared in four levels of FSTI. Near the flat plate LE, FSTI in these four cases is measured as 0.0%, 3.0%, 4.7%, and 8.0%. Due to a converging diverging section present in the computational domain, FST is suppressed and stretched resulting in a reduced FSTI measured before the boundary layer separation location. FSTI at this location is measured again as, 0.0%, 2.1%, 2.5%, and 4.0%, respectively. With increased FSTI, the separation and reattachment locations are found to be closing up with reduced separation bubble length. The bubble height is also reduced with the increase in FSTI. However, the relationship between FSTI and bubble height is non-linear. The separation bubble height varies significantly when switching FST on and off, for example, between 0.0% and 3.0%. However, there is only a small change when FSTI varies from 3.0% and 8.0%. The transition onset location is found to move forward when FSTI increases while the length of the initial separated shear layer reduces. Most importantly, with 8.0% and 4.0% FSTI, respectively, measured near the flat plate LE and before the boundary layer separation, a small separation bubble exists with wall shear stress reduced to negative. Additionally, in this highest FSTI case, no turbulence spot

formation is found from the maximum RMS velocity plot with both wall-normal and span-wise RMS velocities remaining constant before the transition onset location. Results from the 2D flow visualisation also support this conclusion, with vortex shedding clearly observed in the highest FSTI case. This indicates the existence of localised K-H instability coexisting with the streak instability, but with a much weaker magnitude.

The POD of all three fluctuation velocity fields and pressure field have been computed and investigated in the third analysis of this research only for the 0%-FST and 3%-FST. The POD calculation has decomposed these variables into different proper orthogonal modes and ranked them according to their energy contribution to the total kinetic energy. As a result, they can be investigated separately. The POD analyses have been carried out in different cut-planes of the computational domain, providing further explanation of the current separated-flow transition. In the 0%-FST case, the POD analysis also confirms the existence of the K-H instability, in which cross-span energy structures related to the K-H instability can be observed in the most energised POD modes. The corresponding time-coefficient PSD also possesses a distinct frequency peak that is within the K-H unstable-frequency range. In the 0%-FST case, the primary POD mode alone has contributed about 70% of the total kinetic energy. In the 3%-FST case, the primary mode only contributes about 20% of the total kinetic energy, and the remaining energy is spread across the high-order modes. Streaky energy structures are found to dominate in the first few low-order modes, which have contributed about 45% of the total kinetic energy. This implies that the boundary layer streaks dominate in the current transition process. The K-H related frequency peak can be detected from the current time-coefficient PSD, supporting the coexistence of K-H and streak-related instabilities in the current transition process. Nevertheless, this K-H related frequency peak is found to have a different magnitude in different span-wise locations, indicating that the current K-H instability is a localised transition activity. From the POD mode visualisation, both the inner and outer mode streak instabilities normally found in bypass transition can be observed in the current transition process. These are also span-wise localised instability activities found to exist in different span-wise locations. In this chapter, the wall-normal and span-wise fluctuation velocity POD were employed to analyse the separated-flow transition, which covered the deficit from the previous approach in the literature. In [Hosseini-verdi and Fasel \(2018\)](#), only the stream-wise fluctuation velocity POD was investigated, resulting in the K-H instability

not being detected. This is due to the stream-wise velocity field being dominated by boundary layer streak unsteadiness, with a much weaker K-H footprint completely covered up.

Both 2D and 3D flow visualisations and 2D particle tracking have been carried out in the final part of this research. The two modes of streak (secondary) instability in the current separated-flow transition have been found to share some similarities with the two streak instability modes in bypass transition. Identical to bypass transition, the inner and outer mode streak instability are respectively caused by a near wall inflection point and by a near boundary layer edge inflection point in the velocity profile. Nevertheless, other aspects of the current streak instabilities remain different to those in bypass transition. First, both modes of streak instability are inviscid shear layer instabilities that happen in the separated shear layer. This is different to bypass transition in where the separation bubble is eliminated. Second, similarity can be found between the inner mode streak instability and the K-H instability. The part-span K-H rollers are believed to be caused by the inner mode streak instability when the span-wise wavelength of the host streak has increased. This also provides an explanation for the K-H frequency being detected by the time-coefficient PSD analysis. Third, the instability of the outer mode streak instability arises due to the formation of ring-like structures (increased Q -criterion value) wrapping around the low-speed streak. These ring-like vortex structures are a precursor to the Hairpin vortex. Lastly, the breakdown pattern from these two streak instability modes is via the varicose (symmetric) pattern. In this study, dynamics of separated-flow transition with the coexistence of both streak and K-H instability are reported, which were not reported previously in the literature. Additionally, the current study reports outer and inner streak instability modes existing in the separated-flow transition, which has not been previously reported. The particle tracking method employed in the current study has not been previously applied to any separated-flow transition, which is considered to be a plausible approach for studying this complex transition mechanisms.

8.2 Scope for Future Research

The established understanding of the elevated-FST level on separated-flow transition is that it can lead to a shorter separation bubble, which is a result of the early shear layer breakdown. The coexistence of both the K-H instability and the streak-related instability mechanisms are believed to be the cause. However, the underlying breakdown mechanisms with both these instability mechanisms remain a mystery. Further research is advised to understand these breakdown mechanisms.

A three-dimensional POD analysis can be greatly beneficial to the understanding of this topic. However, due to the limited computational resources, this analysis has not been carried out in the current research. Therefore, a three-dimensional POD analysis is advised to be conducted in future research.

The current research on the separated-flow transition was conducted on an elliptical leading-edge flat plate. Two sites of receptivity, where low frequency energy from FST penetrates into the boundary to form streaks, can be found. These are the flat plate leading edge and where the elliptical leading edge joins the flat plate surface. This is not the case in an actual turbine blade profile with only one site of receptivity, which is the leading edge. Also, the surface curvature and the centrifugal force of the turbine blade suction-side surface have not been accounted for by the flat plate model. Therefore, a similar research on the transition process can be conducted on a turbine blade profile.

Lastly, the input from the SGS turbulence model in LES is a shortcoming, and DNS calculation can be conducted in a future research.

Bibliography

- Abadalla, I. E. and Yang, Z. (2004). Numerical study of the instability mechanism in transitional separating-reattaching flow. . *International Journal of Heat and Fluid Flow*, 25:593–605.
- Abadalla, I. E. and Yang, Z. (2005). Numerical study of a separated-reattached flow on a blunt plate. . *AIAA J.*, 43:2465–2474.
- Abdalla, I., Yang, Z., and Cook, M. (2009). Computational analysis and flow structure of a transitional separated–reattached flow over a surface mounted obstacle and a forward-facing step. *Int. J. Comput. Fluid Dyn.*, 23:25–57.
- Alfredsson, P. and Matsubara, M. (2000). Free-stream Turbulence, Streaky Structure and Transition in Boundary Layer Flows. *AIAA, Fluids June-2000 Conference and Exhibit, Fluid Dynamics and Co-located Conferences*.
- Andersson, P., Brandt, L., Bottaro, A., and Henningson, D. (2001). On the breakdown of boundary layer streaks. . *J. Fluid Mech.*, 428:29–60.
- Balzer, W. (2011). Numerical investigation of the role of freestream turbulence in boundary-layer separation and separation control. . *PhD Thesis, The University of Arizona*.
- Balzer, W. and Fasel, H. (2016). Numerical investigation of the role of freestream turbulence in boundary-layer separation. *J. Fluid Mech.*, 801:289–321.
- Bhushan, S., Walters, D. K., Muthu, S., and Pasiliao, C. L. (2018). Identification of Bypass Transition Onset Markers Using Direct Numerical Simulation. . *Journal of Fluids Engineering, ASME*, 140:111107–1–111107–9.

- Brandt, L. and de Lange, H. (2008). Streak Interactions and Breakdown in Boundary Layer Flows. *Physics of Fluids*, 20:024107–1 16.
- Burgmann, S., Dannemann, J., and Schroder, W. (2008). Time-resolved and volumetric PIV measurements of a transitional separation bubble on an SD7003 airfoil. *Exp. Fluids*, 44:609–622.
- Castro, I. and Haque, A. (1988). The structure of a shear layer bounding a separation region. Part 2. Effects of free-stream turbulence. . *J. Fluid Mech.*, 192:577–595.
- Chandrasekhar, S. (1968). *Hydrodynamics and hydromagnetic stability*. Oxford University Press.
- Choi, H. and Moin, P. (2011). Grid-pint requirements for large eddy simulation: Chapman’s estimates revisited. . *Center for Turbulence Research - Annual Research Briefs*.
- Clark, R. A., Ferziger, J. H., and Reynolds, W. C. (1979). Evaluation of subgrid models using an accurately simulated turbulent flow. . *J. Fluid Mech.*, 91:273–337.
- Cobley, K., Coleman, N., Siden, G., and Arndt, N. (1997). Design of new three stage low pressure turbine for BMW Rolls-Royce BR715 engine. *ASME*, 97.
- Coull, J. and Hodson, H. (2011). Unsteady Boundary Layer Transition in Low-pressure Turbines. *J. Fluid Mech.*, 681:370–410.
- Dähnert, J. (2013). Transition Mechanisms in Laminar Separated Flow Under Simulated Low Pressure Turbine Aerofoil Condition. *Journal of Turbomachinery*, 135:1–10.
- Dähnert, J., Lyko, C., and Peitsch, D. (2012). Transition mechanisms in laminar separated flow under simulated low pressure turbine aerofoil conditions. *J. Turbomach.*, 135:011007.
- Danaila, I., Dusek, J., and Anselmet, F. (1997). Direct numerical simulation of the free, unsteady, round, unforced jet at low Reynolds numbers. *Direct and Large-Eddy Simulation II*.
- Dryden, H. L. (1936). Air flow in the boundary layer near a plate. *National Advisory Committee for Aeronautics (NACA)*, 34.

- Emmons, H. W. (1951). The Laminar-Turbulent Transition in Boundary Layer - Part I. . *J. Aero. Sci.*, 18:490–498.
- Germano, M., Piomelli, M., Moin, P., and Cabo, W. (1991). A Dynamic Subgrid-scale Eddy Viscosity Model. *Phys. Fluids*, page 1760.
- Hack, M. (2014). *Localized Instabilities of Klebanoff Streaks and the Influence of Time-harmonic Wall Forcing on Bypass Transition*. PhD thesis, Imperial College London.
- Herbert, T. (1983). Secondary instability of plane channel flow to subharmonic three-dimensional disturbances. *Physics of Fluids*, 26.
- Hillier, R. and Cherry, N. (1981). The effect of stream turbulence on separation bubble. . *J. Wind Engineering and Industrial Aerodynamics*, 8.
- Ho, C. and Huerre, P. (1984). Perturbed free shear layers. *Ann. Rev. Fluid Mech.*, 16.
- Hosseinvardi, S. and Fasel, H. (2018). Numerical Investigation of Laminar-turbulent Transition in Laminar Separation Bubble: the Effect of Free-stream Turbulence. . *J. Fluid Mech.*, 858:714–759.
- Istvan, M. and Yarusevych, S. (2018). Effects of free-stream turbulence intensity on transition in a laminar separation bubble formed over an airfoil. *Exp. Fluids*, 59:52.
- Jacobs, R. and Durbin, P. (2001). Simulations of Bypass Transition. *J. Fluid Mech.*, 428:185–212.
- Jeong, J. and Hussain, F. (1995). On the identification of a vortex. . *J. Fluid Mech.*, 285:69–94.
- Kendall, J. (1985). Experimental study of disturbances produced in a pre-transitional laminar boundary layer by weak freestream turbulence. *AIAA Paper*, 85.
- Kerschen, E. (1993). Boundary Layer Receptivity Theory. 90-0065, Aerospace and Mechanical Engineering, The University of Arizona. AFOSR Grand Report.
- Klebanoff, P., Tidstrom, K., and Sargent, L. (1961a). The three-dimensional nature of boundary-layer instability. *J. Fluid Mech*, 12.
- Klebanoff, P. S. (1971). Effect of freestream turbulence on the laminar boundary layer. *Bull. Am. Phys. Soc*, 16.

- Klebanoff, P. S., Tidstrom, K. D., and Sargent, L. M. (1961b). The three-dimensional nature of boundary-layer instability. *J.Fluid Mech*, 12.
- Langari, M. (2013). *Large Eddy Simulation of Separated Boundary Layer Transition under Free-stream Turbulence*. PhD thesis, University of Sussex.
- Langari, M. and Yang, Z. (2013). Numerical Study of the Primary Instability in a Separated Boundary Layer Transition under Elevated Free-stream Turbulence. *Physics of Fluids*, 25:1–12.
- Li, H. and Yang, Z. (2016). Numerical study of separated boundary layer transition under pressure gradient. *Conference: The 12th International Conference on Heat Transfer, Fluid Mechanics and Thermodynamics, Malaga, Spain*.
- Lilly, D. (1991). A proposed modification of the Germano subgrid-scale closure method. . *Physics of Fluids*, 4:633–635.
- Mayle, R. E. (1991). The Role of Laminar-Turbulent Transition in Gas Turbine Engines. . *Journal of Turbomachinery*, 113:509–536.
- McAuliffe, B. and Yaras, M. (2008). Numerical Study of Instability Mechanisms Leading to Transition in Separation Bubble. *Journal of Turbomachinery*, 130:1–8.
- McAuliffe, B. and Yaras, M. (2010). Transition Mechanisms in Separation Bubbles Under Low- and Elevated-Freestream Turbulence. *Journal of Turbomachinery*, 132:1–8.
- Nagabhushanan, V., Tucker, P., Jefferson, R., and Coull, J. (2013). Large Eddy Simulation in Low-pressure Turbines: Effect of Wake at Elevated Free-stream Turbulence. *International Journal of Heat and Fluid Flow*, 43:85–89.
- Nagarajan, S., Lele, S., and Ferziger, J. H. (2002). Investigations of time-growing instabilities in laminar separation bubbles. . *Eur. J. Mech. B/Fluids*, 21:495–509.
- Nagarajan, S., Lele, S., and Ferziger, J. H. (2007). Leading-edge effects in bypass transition. *J. Fluid. Mech.*, 572:471–504.
- Page, G. J. (2005). Influence of Nozzle Modelling in LES of Turbulent Free Jets. . *In Proceedings of 11th AIAAICEAS Aeroacoustics Conference*.

- Page, G. J., McGuirk, J. J., Hughes, N. J., and Hossain, M. Trumper, M. T. (2002). A Computational and Experimental Investigation of Serrated Coaxial Nozzles. . *In Proceedings of 8th AIAA/CEAS Aeroacoustics Conference.*
- Pokora, C., McMullan, W., Page, G., and McGuirk, J. (2011). Influence of a Numerical Boundary Layer Trip on Spatio-temporal Correlation within LES of a Subsonic Jet. *Presented at the 17th AIAA/CEAS Aeroacoustics Conference, Portland, Oregon.*
- Rhie, C. and Chow, W. (1983). Numerical Study of the Turbulent Flow Past an Airfoil with Trailing Edge Separation. . *AIAA Journal*, 21:1525–1532.
- Rogers, M. and Moser, R. (1993). Direct numerical simulation of a self similar turbulent mixing layer. . *Physics of fluids*, 6:903–923.
- Saric, W., Helen, L., and Kerschen, E. (2002). Boundary-layer Receptivity to Freestream Disturbances. *Annu. Rev. Fluid Mech.*, 34:291–219.
- Satta, F., Simoni, D., Ubaldi, M., Zunino, P., and F., B. (2010). Experimental investigation of separation and transition processes on a high-lift low-pressure turbine profile under steady and unsteady inflow at low Reynolds number. *J. Therm. Sci.*, 19:26–33.
- Schlichting, H. (1979). *Boundary-Layer Theory*. McGRAW-HILL.
- Serna, J. and Lazaro, B. J. (2015). Numerical study of instabilities in separated-reattached flows. *Eur. J. Mech.: B/Fluids*, 49:171–183.
- Simoni, D., Lengani, D., Ubaldi, M., Zunino, P., and Dellacasagrande, M. (2017). Inspection of the dynamic properties of laminar separation bubbles: Free-stream turbulence intensity effects for different Reynolds numbers. *Exp. Fluids*, 58:66.
- Sirovich, L. (1987). Turbulence and the dynamics of coherent structure. I. coherent structures. . *Quarterly of Applied Mathematics*, 45.
- Spalart, P. and Strelets, M. (2000). Mechanisms of transition and heat transfer in a separation bubble. *J. Fluid Mech*, 403:329–349.
- Swearingen, J. D. and Blackwelder, R. F. (1987). the growth and breakdown of streamwise vortices in the presence of a wall. *J.Fluid Mech*, 182:255–290.

- Sylvain, L., Michael, L., and Tamer, Z. (2012). Large Eddy Simulation of Transitional Separated Flow over a Flat Plate and a Compressor Blade. . *Flow Turbulence Combust*, 88:19–44.
- Taylor, G. I. (1939). Experimental study of disturbances produced in a pre-transitional laminar boundary layer by weak freestream turbulence. In *Den Hartog, J. and Peters, H., editors, Proceedings Fifth International Congress for Applied Mechanics*.
- Urbain, G. and Metais, O. (1997). Large-Eddy Simulation of Three-dimensional Spatially-developing Round Jets. *Direct and Large-Eddy Simulation II*, 16:35–46.
- Vaughan, N. and Zaki, T. (2011). Stability of zero-pressure-gradient boundary layer distorted by unsteady Klebanoff streaks. *J. Fluid Mech*, 681:116 – 153.
- Volino, R. J. (2002a). Separated Flow Transition Under Simulated Low-Pressure Turbine Air-Foil Conditions: Part 1 - Mean Flow and Turbulence Statistics. . *ASME J. Turbomach.*, 124:645.
- Volino, R. J. (2002b). Separated Flow Transition Under Simulated Low-Pressure Turbine Air-Foil Conditions: Part 1 - Turbulence Spectra. . *ASME J. Turbomach.*, 124:656–664.
- Walker, G. (1989). Transitional Flow on Axial Turbomachine Blading. *AIAA J.*, 27.
- Weiss, J. (2019). A Tutorial on the Proper Orthogonal Decomposition. *AIAA aviation forum, 17-21 June 2019, Dallas, Texas, United States*.
- Wundrow, D. and Goldstein, M. (2001). Effect on a Laminar Boundary Layer of Small-amplitude Streamwise Vorticity in the Upstream Flow. *J. Fluid Mech.*, 426:229–262.
- Yang, Z. (2013). Numerical Study of Instabilities in Separated-Reattached Flows. *Int. J. Comp. Meth. and Exp. Meas.*, 1-2:116–131.
- Yang, Z. and Abdalla, I. (2005). Effects of free-stream turbulence on large-scale coherent structures of separated boundary layer transition. . *Int. J. Numer. Meth. Fluid.*, 49:331–348.
- Yang, Z. and Voke, P. (2000). On early stage instability of separated boundary layer transition. *Advances in Turbulence VIII*.

- Yang, Z. and Voke, P. R. (2001). Large-eddy Simulaiton of Boundary-layer Separation and Transition at a Change of Surface Curvature. *J. Fluid Mech*, 439:305–333.
- Yi, W., Corbett, D., and Yuan, X. F. (2016). An Improved Rhie-Chow Interpolation Scheme for the Smoothed-interface Immersed Boundary Method. . *Nnternational Journal for Numerical Methods in Fluids*, 82:770–795.
- Zaki, T. (2011). From Streaks to Spots and on to Turbulence: Exploring the Dynamics of Boundary Layer Transition. *J. Fluid Mech*, 681:116 – 153.
- Zaki, T. and Durbin, P. (2005). Mode interaction and the bypass route to transition. . *J. Fluid Mech.*, 531:85–111.
- Zaki, T. and Durbin, P. (2006). Continuous mode transition and the effects of pressure gradient. *J. Fluid Mech.*, 563:357–388.